PhD in Chemical Science and Technology

Cycle XXV

Development of innovative processes and materials for the CO_2 conversion and separation from mixtures of combustion products

PhD Student: Luca Cappai

Coordinator of the PhD Program: Prof. Carla Cannas

Supervisor: Prof. Gabriele Mulas

Final Exam: Academic Year 2021-2022

Thesis defence: September 2023 session

1 Summary

1. INTRODUCTION

The continuous increase of the CO_2 atmospheric concentration has just approached, during 2023, the value of 420 ppm (Figure 1.1). According to the reports of different experimental campaigns on drilled ice cores, and the results of modelling investigation, the cited concentration is the highest one reached in the last 800 000 years [1] and represents a critical benchmark negatively affecting human health and climate and tropospheric ecosystems [2,3]. The increasing in the CO_2 atmospheric concentration, at a rate of about 2 ppm per year in the last decade, has brought to largely overcome the preindustrial level, which was about 275 ppm. This dramatic change can be related to anthropic emissions, in particular to the large use of fossil fuels. In 2018 37.5 $GtCO_2$ on 55.3 $GtCO_2$ of the total greenhouse gasses emissions aroused from the combustion of fossil fuels, mainly addressed to the production of energy, heating and mobility systems [4]. The extraordinary increase of CO_2 in the atmosphere raise several concerns related to the environmental problems and climate changes which are due to its activity as greenhouse gas [5]. Indeed, the amount of CO_2 emitted into the atmosphere by electrical power plants, transportation, concrete and building industries, etc… is so much that natural CO_2 cycle and natural CO_2 capturing capacity have been overwhelmed.

What briefly described, represents a worldwide challenge of our times, which should trigger the deployment of proper responses and adequate policies by countries and supranational organisations. It, in turns, is committing the scientific community to provide innovative scientific and technological breakdowns to effectively face such new scenario. To this regard, the reduction of the CO_2 emission has been already started by shifting the energy production from fossil fuels towards the harvesting of renewable energy sources which has been strongly supported and financed in many countries at different scale, i.e. both at domestic and industrial levels. Although the increase of renewable sources net capacity in the last years, they are still not able to cope with the worldwide electricity demand [6,7]. Indeed, their implementation on a

wider scale is, at present, still hampered by the lack of reliability due their intermittent nature, as well as by the high storage cost. In order to push forward effective policies, the 2015 Paris agreement set to 2.0 °C, the maximum global temperature increase, with respect to pre-industrial level, that can be sustained by the earth environment and life systems, even though strongly recommending keeping this value below 1.5 °C by 2100. Those goals can be achieved only controlling anthropic CO_2 emission in the atmosphere. The need of new methods and technologies for CO_2 capture and transformation has given rise to the Carbon Capture Utilization and Storage strategies (CCUS) [8–10], which gather new methodologies technologies, policies, regulating frameworks etc, aiming for CO_2 removal from flue gas or directly from the atmosphere, followed by recycling the captured CO_2 for utilization or for determining a safe permanent storage.

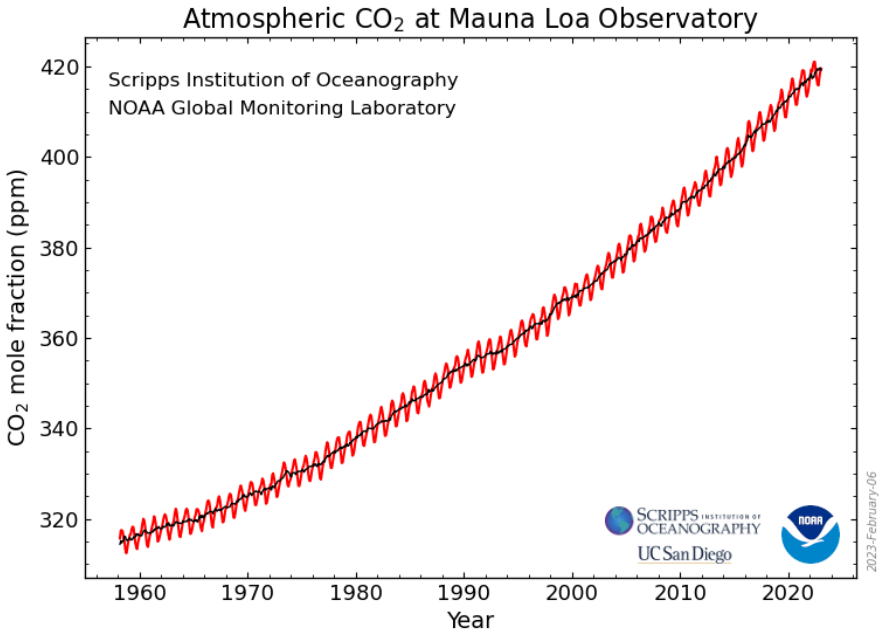

Figure 1.1: Historic CO_2 atmospheric concentration at Mauna Loa Observatory, Hawaii, USA. The red line represents the monthly mean values while the black line represents the average value corrected for the seasonal cycle [11]

1.1 Photochemistry

Photochemistry is defined as a branch of chemistry that deals with the effects of radiant energy in producing chemical changes. The main goal is to use the absorption of a photon energy in a suitable material to make a reaction happens. From the Grotthuss-Draper law we know that only absorbed light by a system can produce a photochemical change [12]. The choice for a suitable material for photochemistry must consider the Stark-Einstein law that states that for each photon of light absorbed by a chemical system, only one molecule is activated for subsequent reaction [13]. This is true assuming that non biphotonic processes occur. We can therefore summarize that every photochemical or photophysical process is triggered by the absorption of a photon by a molecule.

The absorption of a photon by a material is the first step of a photochemical process. If the photon absorbed possesses enough energy (higher than the energy band gap) an electron can be promoted into an unoccupied orbital (LUMO) from the highest occupied one (HOMO). Usually, photochemical processes are so triggered on semiconductor materials where you promote an electron from the valence band (VB) to the conduction band (CB). The Energy band gap is a primary parameter we have to consider when determining the choice of a semiconductor, but this is not the only parameter we have to focus to.

When a photon is absorbed an electron of the material is promoted generating an electron-hole pair system that is bound together by Coulomb forces [5]. The electron-hole pair can dissociate into free charges that must migrate separately on the absorbent material surface sites. The migration of this charges permits the occurrence of a chemical reaction on the surface. It has to be taken into account that molecules with excited electrons can undergo charge recombination processes. Fast recombination times cause an electron reconfiguration that prevents the electron-hole pair system to reach the surface of the material affecting his potential for

photochemistry. On the surface electrons and holes may reduce an adsorbed acceptor (*i.e.* CO_2) or oxidize an electron donor (*i.e.* OH^-).

The electronic excitation in a semiconductor may be accompanied by a partial electron transfer between the atoms if the material is characterized by a p-d transition, as it often happens in titanium dioxide, TiO_2. In semiconductors such as NiO, characterized by a d-d transition, the electron excitation between the valence and conduction bands occurs between two orbitals d of the Ni atom. This transition leads to a generally lower energy band gap but also to faster recombination rates.

In order to trigger a redox reaction, the band edges of a semiconductor must be properly aligned with the redox potential of the reaction. For example, the complete reduction of CO_2 to methane is characterized by a standard potential of E^0 = - 0.24 eV (Equation 1.1).

$$CO_2 + 8e^- + 8H^+ \rightarrow CH_4 + 2H_2O \quad (1.1)$$

To promote such reaction, the conduction band must be more negative than the reduction potential and the valence band must be more positive than the complementary oxidation reaction potential. The semiconductor must provide overpotential for both electrons and holes transfer to electron acceptors and donors. If one of the two criteria of potential is not fulfilled, a sacrificial agent may be needed to permit for the oxidation or the reduction semi reaction to occur.

The energy band gap thus must ideally be wide enough to permit the storage of enough energy to break a chemical bond (for example, C=O 750 kJ mol^{-1}), or trigger a molecule rearrangement while simultaneously be able to act as electron and hole transfer.

The quantum efficiency (QE) of a photochemical reaction represents the ratio between incident photons and converted electrons [14]. Several processes may affect the QE of a photochemical reaction. Highly energy demanding reaction and reaction that involves highly energetic adsorption steps usually require UV light irradiation, more energetic and thus more subject to energy losses processes, affecting negatively the

QE of the process. The irradiation of samples with photon having energy larger than the band gap cause the formation of hot charge carriers. The excess energy is then lost through thermalization. Other energy losses may depend on indirect, or dipole forbidden transitions, Auger recombination and nonradiative recombination.

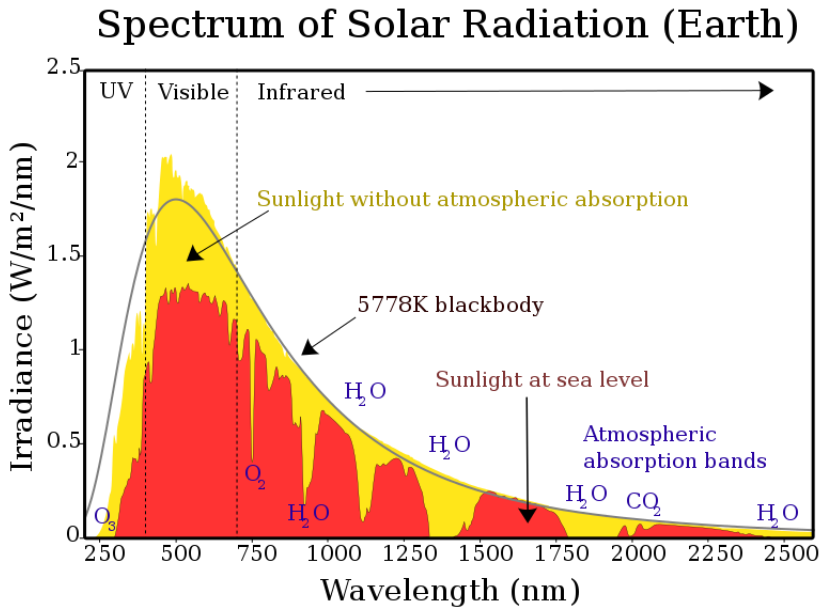

Figure 1.1.1: Solar spectrum theoretical blackbody (black line); without atmospheric absorption (yellow + red area); on Earth's surface (red area) [15].

Activation of photochemical processes is nowadays carried out by resorting to different wavelengths, ranging from the far UV to the near-IR. Solar driven photochemistry has attracted more attention in the last few years because it has the possibility of exploiting a natural free and abundant energy source. Solar radiation has a huge wavelength range spanning from 100 nm to 1 mm. The distribution of the total power in function of the energy can be interpretated as the curve of emission of a blackbody. The total energy irradiated varies depending on Earth's orbit and obliquity. Not all the wavelengths can be exploited on Earth's surface due to the shield effects of the atmosphere. Ultraviolets photons ranging from 100 nm to 280 nm (UVC) are almost totally absorbed in Earth's upper atmosphere. UV light ranging from 280 nm to 315 nm

catalyse the production of ozone in the atmosphere, and thus a large part of these radiations is absorbed by oxygen molecule before arriving to the surface (UVB). Those radiations are nevertheless responsible for sunburns and development of skin cancer. The solar radiation is further subject to absorption by molecules like CO_2 and H_2O among others thus the solar radiation on Earth's surface assumes a figure like the one reported in Figure 1.1.1.

1.2 Aim of the Thesis

The shortly introduced topics represent the field within which the doctoral research activity has been carried out. The present thesis work has then been addressed to the study and implementation of the CO_2 conversion process activated via photochemical irradiation. Particular focus has been given to the investigation of the reactivity, as photoactivators, of different silicate-based materials characterized by low cost and abundance: olivine, a natural silicate-based mineral class, and industrial waste products such as the steel slags produced by electric arc furnaces. Indeed, olivine, structurally characterised by a solid solution of Fe_2SiO_4 (fayalite) and Mg_2SiO_4 (forsterite), are among the most widespread classes of minerals on Earth's crust. On the other hand, steel slags are a by-product obtained in large amount every year as the result of the industrial processes for the steel production. The common point that relies on these two classes of materials that have been investigated in this thesis, is the ability to provide a basic reaction in water solution, which, in turn, may facilitate CO_2 dissolution in H_2O. Redox and acid base natural reactions activated on such silicates in presence of water may fix the CO_2 in form of metal carbonates and may produce a reducing environment [16–18]. The possibility to resort to raw materials or to industrial slags to promote CO_2 conversion processes is, of course, a subject of great interest, either for basic science investigation, or in view of potential application purposes. However, the available literature data, relevant to the investigation of such reactivity behaviour, highlight that the above processes are, nowadays, characterized by slow kinetics that prevent the application on large scale [19]. The solar-driven CO_2

conversion processes are considered nowadays, instead, a more promising route to achieve a large-scale application.

While pristine olivine minerals and steel slags are good candidates as substrates and activators for CO_2 conversion strategies for their abundancy, low cost and reactivity, their poor photochemical efficiency represent a drawback that limited the research aimed at their actual implementation. The present work deals with such issue, addressing the problems posed by solar-driven CO_2 conversion processes on silicate-based materials.

The project purposes were to achieve the photochemical activated CO_2 conversion processes on the silicate-based materials through their eventual modification, to increase the efficiency of the CO_2 conversion processes, to identify and quantify the products of conversion, and to possibly evaluate the kinetics of the conversion processes.

Considering the needs for a closed-circle CO_2 re-utilization, the possibilities of utilization of metal carbonates produced by CO_2 fixation have been investigated. In particular, as a possible industrial application, the possibility to increase the permeation efficiency at low temperatures of carbonate-based dual phase membranes have been investigated.

The second Chapter of this thesis will address the state of the art for CO_2 conversion and capture strategies. First, it will be provided an introduction to the general approach to these strategies and then the focus will shift to the processes activated via photochemical route on olivine and steel slags. A brief description of the materials tested and their reactivity towards CO_2 will be also provided in pair with the description of carbonate based dual-phase membranes. Afterwards, in Chapter 3, the experimental methods and techniques used for samples characterization and products analysis will be briefly described. The Chapters 4, 5 and 6 will be dedicated to the description of the experiments and the experimental results on olivine, steel slags and dual-phase membranes respectively.

2 STATE OF THE ART

As reported in the previous section, finding efficient and sustainable solutions to rising CO_2 levels is a critical scientific and technological challenge of our times. It is evident that the vast literature on the subject covers a range of fields, which includes, among others, chemical systems and their reactivity in specific processes, industrial issues, environmental issues, political, economic and regulatory affairs. The analysis of all these aspects is beyond the scope of the present thesis, and, in the following pages, the attention will be addressed to present the main recent findings and the still open questions concerning innovative chemical processes as well as molecular and material systems that can be used in a sustainable approach to CO_2 transformation.

2.1 CO_2 Conversion and capture strategies

Climate change mitigation and environmental preserving are strongly dependent on the successful achievement in the actions addressed to CO_2 emission reduction. Anthropic CO_2 emissions are produced by different routes and are mainly due to fossil fuels combustion processes used for energy production, transportation, and other industrial sectors [20]. Different approaches and strategies to capture and convert CO_2 are the object of intense research activities and have been studied and developed within the criteria of CCUS strategies [21–23]. Accordingly, investigation has been focused to explore and develop both innovative capture and conversion procedures. As for the former, different storage strategies have been widely studied, namely *in situ* and ex situ sequestration processes, referring to the mineral sequestration of carbon dioxide through processes occurring, respectively, below or above ground level [24]. In situ strategies require that the reaction between CO_2 and geological formation of reactive class of minerals is triggered after underground injection of the gas. Mg and Ca rich mineral classes, such as orthopyroxene, clinopyroxene, serpentine and olivine have been identified as candidates for in situ capture strategies, thanks to the

spontaneous and exothermic reactions occurring between CaO or MgO and CO_2 to form carbonates (Equation 2.1-2.2).

$$CaO + CO_2 \rightarrow CaCO_3 + 179\ kJ\ mol^{-1} \quad (2.1)$$

$$MgO + CO_2 \rightarrow MgCO_3 + 118\ kJ\ mol^{-1} \quad (2.2)$$

Natural carbonation rates have been enhanced by increasing the injecting gas temperature and pressure, and test injections were performed on basalt sites, by mixing pure CO_2 with water and H_2S either at low (20-50 °C) either at high (>250 °C) temperature [24]. Ex situ strategies, on the other hand, require the mineral mining prior to proceed to the carbonatation reaction. Direct routes usually require high CO_2 pressure and temperatures, and research has been focused on improving carbonation rates by optimizing the surface area, using heat or mechanical activation methods, physical or chemical pre-treatments [25,26]. Reaction rates and conversion are usually still not able to compensate CO_2 emissions produced during the whole process. Indirect carbonation routes are instead technologically feasible but the widespread of these methodologies has been slowed by the high cost associated on large scale plants [27].

One possibility to overcome the problems associated with the pure sequestration process is represented by different conversion routes, aimed at obtaining additional chemical products with high added value and characterised by the possibility of reuse. The conversion of CO_2 has been focused on the production of different chemicals, spanning from hydrocarbons to alcohols, carbon monoxide or carboxylic acids [28–31]. To this regard, electrochemical and thermal activated CO_2 conversion processes have represented a large part of their research effort. Electrochemical CO_2 conversion requires durable and efficient electrocatalysts for both cathode and anode, where the reduction reaction of CO_2 and evolution reaction of O_2 occur, in order to increase the efficiency of the process. Electrodes and electrolytes that possess high conductivity are also required to achieve a suitable mass transport of products and reactants [32]. The electrochemical processes proved to be very effective in selectivity to products like acetate or formic acid with various electrodes like CuS, Pb, sulfure modified copper

catalyst, $[SiW_9V_3O_{40}]^{7-}$(SiW_9V_3) reaching high values of CO_2 conversion [33,34]. While the results are encouraging the studies are focused more on improving the efficiency of the methods than on improving their sustainability. Thermally activated conversion processes have been proposed for both production of syngas via reverse water-gas shift (RWGS) reaction or bi-reforming process, and production of methanol or light hydrocarbons [35,36]. Among the numerous researches, it is here to be remembered that many authors have investigated the catalytic properties of different noble metals as Rh, Ru, Pd, Pt or Ir, and relevant compounds, focusing on the improvement of products selectivity more than total CO_2 conversion efficiency [37–39].

While the results obtained are quite encouraging those studies do not face neither the problems related to the utilization of non-renewable energy sources nor the utilization of critical raw materials [40]. Noble metal-based catalysts tested for CO_2 methanation (especially Rh-based catalysts), although efficiently converting CO_2 under different experimental condition, are usually associated with sintering problems, elevated reaction temperatures and economical drawbacks. Ni-based catalysts have been proposed to partially solve those problems but the difficulties concerning the low temperature activation have not yet been fully resolved [41]. The implementation of methods capable of converting CO_2 by activating the process using renewable energy sources is a step forward to achieve a full-circle recycling of CO_2. Feasible sunlight activated photocatalytic CO_2 conversion processes, mimicking natural photosynthesis, will be the ideal route to reach this goal.

As a matter of the fact, beside the above cited routes, it is recent the interest towards further CO_2 conversion methods, and among these, photoelectrochemical, photochemical and biochemical processes , have attracted growing attention in the literature [42]. Photochemical processes are purely based on the exploitation of radiant energy to trigger a chemical reaction. Photoelectrochemical processes, on the other hand, combine the photochemical approach with the electrochemical one. The electricity and the light irradiation are the driving forces for the CO_2 conversion

reaction, simulating an artificial photosynthesis process where the critical step is the adsorption and activation of CO_2 and intermediates, to an electrode surface. Biochemically activated CO_2 conversion, instead, tries to exploit the anaerobic digestion processes, usually carried out by enzymes, bacteria or other microorganisms, in order to transform the gas into valuable products [41].

In particular, biochemical method, using bacteria, have shown very good results in terms of observed conversion (CO_2 conversions reaching values over 5000 µmol g^{-1} h^{-1}) but research conducted so far are still affected by problems related to the high cost of bioreactor and the difficulties of scaling up the process because of the amount of nutrients required for the microbial culture to stay alive [33,43].

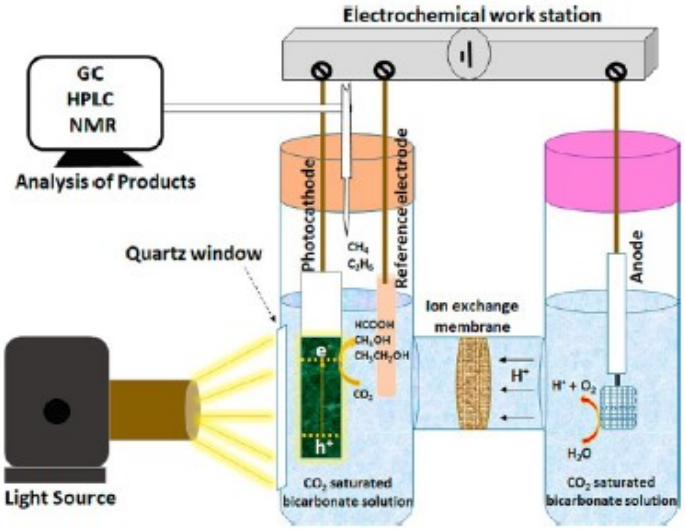

Figure 2.1.1: Schematic H-type photoelectrochemical reactor for CO_2 conversion [44]

Photoelectrochemical CO_2 conversion proceeds through e^-/H^+ transfer and associated C-O bond breaking and C-H bond formation but no detailed reports on the kinetics of CO_2 conversion can be found in the literature. The conversion processes are negatively affected by the poor electron affinity of the gaseous CO_2. Reaction routes and intermediates may be very different depending both on the reactor geometry and on the electrode investigated. Most of the studies focused on H-type

photoelectrochemical reactors with suitable ion-exchange membranes (Figure 2.1.1). With the use of multilayer electrolysers, it has been possible to reach conversion up to 40%. The lack of comprehensive studies on the mechanism of the processes and the need of an electrolyte solution still limit the industrial application of photoelectrochemical conversion strategies [44].

2.2 Photochemical CO_2 conversion

Photochemical CO_2 conversion is considered, nowadays, to be more promising for large-scale applications with respect to the previous activation methods. Indeed it has been on the spot since the first work, published in 1979 by Inoue et al., that presented the photoreduction of CO_2 to formic acid, formaldehyde and methanol [45]. Different heterogeneous photocatalysts have been developed, to be activated by visible or UV light irradiation. As mentioned in Chapter 1.2 photochemical conversion on CO_2 requires the adsorption of the gas to lower the energy of the C=O bond (750 kJ mol^{-1}) allowing for this bond to be broken thanks to the energy provided by visible/UV irradiation. The ideal photocatalyst must permit the transfer of electron-hole pairs to the adsorbed CO_2. H_2O is an ideal sacrificial reagent to consume the photogenerated holes. Various work used H_2O as electron donor and hydrogen source using photocatalysts like Cu_xO nanoclusters or Ag clusters loaded on Ga_2O_3 [46]. Different studies have tackled the issue of H_2O possible reduction. Hybrid materials composed of semiconductor/semiconductor, semiconductor/metal complex, cocatalyst/semiconductor, with appropriate spatial architecture, energy band gap and photoreduction conditions, were developed to achieve CO_2 reduction coupled with H_2O oxidation. Systems for artificial photosynthesis (Z-scheme) were also developed to avoid the reduction of H_2O. TiO_2 is the most used photocatalyst material [14]. Among the non-TiO_2 based photocatalysts we must report Ge, Ga, W, Ni-based, graphitic carbon nitride, Ag plasmonic systems, photoactive MOFs. Different works on TiO_2

photochemical activated conversion were focused on engineering the crystal phase and facets [47,48]. The increase of surface area and utilization of porous substates to increase the number of active sites has been also studied. The energy band gap of pure titania of 3.0 eV is suitable for UV light activation but not for solar activated photocatalysis. TiO_2 doping with nonmetal (F, N, C, S, P) or metal (Ni, Co, Cu, Ce, Mo, In, V, Cr) ions was investigated to narrow the energy band gap. Cu doped TiO_2 has proved to be effective in reducing the energy band gap and enhancing the selectivity to HCOOH, while N doping can lower the energy associated with the valence band by increasing the light absorption efficiency. This leads to better results in terms of conversion and selectivity [49,50]. TiO_2 was also modified trying to exploit plasmonic effects associated with noble metals, like Au or Ag nanoparticles, or promote charge separation and reaction rates by loading noble metals as cocatalysts [51,52]. The presence of noble metals boosts the Hydrogen production and was proved to be effective in increasing the selectivity of conversion to methane and/or CO. Among the non-TiO_2 photocatalysts, Cu_2O drew the attention of the scientific community for his ability to carry on photochemical CO_2 conversion reactions with visible light irradiation. While the results reported in the literature evidence high selectivity and good conversion, deeper understanding of reaction mechanism and optimization of surface, facets, phases and material properties are still needed in order to increase the CO_2 conversion [14].

2.3 Materials

In the previous paragraphs we have provided a general overview of the developments concerning the CO_2 conversion strategies and the activation methodologies currently endeavoured by the scientific community. In the following section the focus will shift to a more detailed description of the class of materials investigated within the present research activity.

2.3.1 Olivine

Mafic and ultramafic rocks like olivine and pyroxenes, and their component silicate materials, in nature gave rise to weathering processes (Equation 2.3) able to capture CO_2 from the atmosphere [53]. The 99.94% of all CO_2 sustainably captured into carbonate rocks has been produced with these processes during Earth history and they play a fundamental role into Earth Carbon cycle [54,55].

$$Mg_2SiO_4 + 4H_2O + 4CO_2 \rightarrow Mg^{2+} + 4HCO_3^- + H_4SiO_4 \quad (2.3)$$

Olivine has then been identified as promising candidate for CO_2 capture and permanent storage option for its abundance and inexpensiveness, and due to its ability of imparting a basic reaction in water solution thanks to the presence of metal silicates [24]. Permanent CO_2 storage strategies have been investigated, but the scaling up of such strategies has been slowed down by technology optimization problems, environmental issues and economic feasibility [56–58]. Serpentinization process often accompanies CO_2 fixation in form of carbonates in natural conditions in presence of water and high pressures [17]. The reaction mechanism under such conditions (equation 2.4 to 2.6) has been investigated to exploit the reducing environment promoting H_2 evolution.

$$(Mg,Fe)_2SiO_4 + 2CO_2 \rightarrow 2(Mg,Fe)CO_3 + SiO_2 \quad (2.4)$$

$$6(Mg,Fe)_2SiO_4 + 12H_2O + 6CO_2 \rightarrow 2(Mg,Fe)_3Si_2O_5(OH)_4 + 2Fe_3O_4 + 8H_2 + 6MgCO_3 + 2SiO_2 \quad (2.5)$$

$$(Mg,Fe)_3Si_2O_5(OH)_4 + 3CO_2 \rightarrow 3(Mg,Fe)CO_3 + 2SiO_2 + 2H_2O \quad (2.6)$$

Hydrothermal and mechanochemical attempts to exploit Mg-rich olivine reactivity, and CO_2 fixation in form of metal carbonates, have been reported in literature [53,59]. Carbonation process thermally activated has been studied after olivine dissolution in acid solutions, and, using the pristine mineral on mild temperature conditions, reached carbonation rates of about 92% [60,61]. The impact of Fe(II) on carbonation rates of olivine was investigated by Wood et al. [62] who found an increase in the carbonation rate while decreasing the Fe(II) content.

Recently, olivine and modified olivine were also investigated as potential substrates for CO_2 transformation processes into light hydrocarbons or simple alcohols [63–65]. The role of Fe(II) was further investigated, Farina et al. were able to identify the oxidation of Fe(II) to Fe(III) as the driving force of CO_2 reduction process under mechanochemical activation [18].

Nature-inspired hydrothermal activation of olivine-based materials present some drawbacks relating to energy consumption due to the high temperatures often involved in the CO_2 reduction processes [26,65].

As far as we know, no publications have been addressing the experimental photochemical CO_2 conversion on olivine activated via solar radiation. Photochemical CO_2 conversion on Fe- and Mg-rich minerals was addressed to find explanation of methane formation on Mars soil [66]. Surface photoreaction via UV irradiation was investigated on hematite by Shkrob et al. [67]. Finally, photochemical activation of CO_2 conversion process on reactive layers of TiO_2 physisorbed and chemisorbed on olivine was investigated by DFT methods by Escamilla-Roa et al. who highlighted the possibility of methane production on Martian or Moon Mg-rich minerals [66].

2.3.2 Steel slags

Electric-arc furnace steel slag is a waste material produced during steel working processes. Iron and Steel industry produce about 0.5 billion Tonnes per year of alkaline waste materials (slags). Iron and steel slags are usually identified by the industrial procedure with which they are produced, indicated by the type of furnace used. We can identify blast furnace slag, from iron producing processes and basic oxygen furnace steel slag (BOFS), ladle furnace slag (LFS) and electric arc furnace oxidizing slag (EAFOS) for steel producing methods [68]. These industrial processes both produce alkaline waste materials currently used only as secondary aggregate, pozzolan or agricultural lime after months of weathering processes to reduce hydroxide content [69,70]. Only a fraction of the total waste material produced worldwide is currently reused as described earlier, the large majority of the steel slag is currently stockpiled. Different

publications focused on the re-utilization of blast furnace slags and basic oxygen furnace steel slags for carbon capture purposes [70–72]. Electric-arc steel slags only recently attracted the attention of the researcher. Currently, 70% of global steel production comes from integrated blast furnace-basic oxygen furnace processes while the remaining 30% from electric arc furnace routes [73]. In the Eu-27 42.4 % of steel is produced within electric arc furnace plants (the percentage rise to 84 % in Italy) [74]. Even if the total annual production deriving from processes concerning the utilization of electric-arc furnaces is lower compared to blast furnace process, the waste slag produced result more appetible for their properties of high affinity with CO_2. Waste products are characterized by the presence of Calcium-rich silicates mixed with iron oxide [75]. They are, indeed, produced by the combination of steel with $Ca(OH)_2$, when this last one compound is added as flux on the molten metal scraps in the furnace. The molten phase usually also contains silicates and oxide materials that combines to obtain the final slag by-product. The steel slag is then separated from the molten steel thanks to its lower density [76]. Steel slag materials are able to give basic pH in water solution thanks to the presence of metal silicates and the pH measured varies in a range from 9 to 13 depending on the composition [77,78]. The reaction between calcium silicates and water, like the example reported for Larnite (Ca_2SiO_4) (equation 2.7), is characterized by the increase of hydroxide ions in the solution.

$$Ca_2SiO_4 + 4H_2O \rightarrow 2Ca^{2+} + H_4SiO_4 + 4OH^- \quad (2.7)$$

This high pH leachates are potentially surface water polluting materials that cannot safely and simply stockpiled [79]. Increasing the reutilization routes his surely needed.

Electric arc furnace slags are considered as oxidizing or reductive systems depending on CaO content (respectively low content and high content). They differ from other steel slags like BOFS or EAFOS for a higher Iron oxide content varying from 24% to 38% [68].

CO_2 fixation by steel slags in form of metal carbonates has been investigated using both direct and indirect routes. The direct route is characterized by a gas-solid interaction

between Ca silicates and gaseous CO_2, and it allows the production of carbonate materials in appreciable quantity only at high temperatures, because of the slow kinetics that characterize the process. The study performed by Santos et al. [80] evidenced an optimal temperature for CO_2 carbonation at atmospheric pressure between 830 °C and 850 °C, this is the highest temperature the process can be held before carbonate decomposition reaction start (after temperature of 850 °C). In the same paper the strong dependence of CO_2 partial pressure on steel slag carbonation rate at relatively low temperature was evidenced. CO_2 uptake was enhanced through water vapour presence and grinding procedures, but generally low carbonation rates observed experimentally and uncertainty on economic feasibility strongly detriments the research on direct carbonation routes [73].

Indirect mineral carbonation is a multi-step route exploiting selective dissolution of calcium ions into aqueous solution and calcium carbonate precipitation processes. The studies of indirect carbonation on steel slags involves the utilization of leaking agents like HCl, organic or mineral acids or complexing salts [71,81–84]. The use of a leaching agent results in the need for a neutralization step of the excess acid in solution and for a regeneration step of the leaching agent. The research has been focused on improving the selective dissolution step while inconsistency remains concerning the economic feasibility and efficiency of the processes [73].

Steel slags have been utilized also as support for various photocatalysts like TiO_2, V-doped materials, CeO_2. Only in 2022 the steel slags have been used as photocatalyst as itself, the steel slags decorated with nanostructured palladium were able to convert CO_2 into formic acid in presence of water [85].

2.4 Molten Carbonate Dual-phase membranes

Considering the needs of a CO_2 full-circle re-utilization, it is essential the study and implementation of the method and applications that allow the optimal utilization of

the products obtained by CO_2 conversion methods. Among the applications that re-use the products of carbonation of the CO_2 there are the dual-phase carbonate-based membranes. Since their first introduction they attracted more and more attention by the scientific community [86]. These membranes have been proposed for CO_2 capture, natural gas separation, energy conversion and diesel-engine pollution reduction [87,88]. Post combustion high temperature CO_2 may be selectively isolated and transported to avoid the gas emission into the atmosphere while O_2 reduction in the gas flow find application in lowering engines pollution by improving the efficiency of reduction systems operating on NO_x or SO_x, like selective catalytic reduction devices implemented in vehicles converters. Dual-phase membranes can be divided in two types depending on the different permeation mechanism involved in the separation process: mixed oxygen-vacancy carbonate-ion conducting (MOCC), mixed electron carbonate-ion conducting (MECC). MOCC membranes are characterized by O^{2-} permeation through the support phase as counter-current transport vessel while in MECC membranes the e^- acts directly to guarantee the counter-current transportation. Therefore, MECC membranes need electron conducting substates, usually a metal.

Metal-Carbonate membranes typically consist of a molten carbonate salts mixture phase supported on a porous electronically conducting metal substrate. Molten salts are infiltrated into the pores of the substate. Carbonate-based membranes are permeable to O_2 and CO_2 and the semi-reactions (2.8-2.9) take places on the two sides of the membrane:

$$CO_2 + \frac{1}{2}\,O_2 + 2e^- \rightarrow CO_3^{2-} \tag{2.8}$$

$$CO_3^{2-} \rightarrow CO_2 + \frac{1}{2}\,O_2 + 2e^- \tag{2.9}$$

The driving force for those semi-reactions is the CO_2 pressure gradient between the feed and permeate side of the membrane. On the feed side of the membrane, O_2 combines with CO_2 and electrons onto the molten carbonates surface and transform into CO_3^{2-}. Carbonate ion is then transported through the molten carbonate phase and

releases electrons, CO_2 and O_2 at the permeate side of the membrane. Electrons will travel back to the feed side of the membrane, in the opposite direction of the carbonate ions, through the electron conducting metal substrate guaranteeing the continuation of the permeation process (Figure 2.4.1). This is the Mixed electron carbonate ion conduction (MECC) permeation mechanism.

The flow of gases through the membrane is governed by transport of carbonate ions in the molten phase and electronic charge carriers in the solid substrate under Wagner-type transport theory electrochemical potential gradient [14]. Flux density for CO_2 can be generally described as (equation 2.10):

$$J_{CO_2} = J_{CO_3^{2-}} = \frac{RT}{2F^2L}\int_{sweep}^{feed} \sigma_{CO_3^{2-},M} + \left[(t_{O^{2-}} + t_{OH^-} + t_{e^-})d\ \ln p_{CO_2} + \frac{1}{2}t_{e^-}d\ln p_{O^{2-}} - t_{OH^-}d\ln p_{H_2O}\right] \quad (2.10)$$

where $\sigma_{CO_3^{2-},M}$ is the conductivity of alkali and carbonate ions, L the membrane thickness, p the partial pressure of gases, t the transport number, R the gas constant, F the Faraday constant e T the temperature.

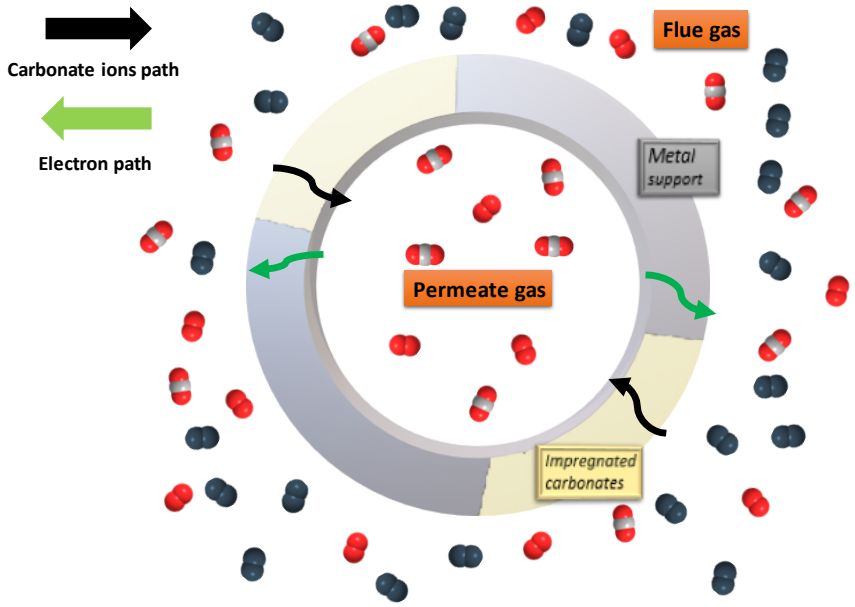

Figure 2.4.1: Schematic representation of dual-phase metal-carbonate membrane

The rate-limiting steps of CO_2 and O_2 permeation have been identified as the peroxycarbonate and the peroxide formation (equation 2.11-2.12) on the surface of the molten carbonate phase[89,90].

$$\frac{1}{2}\,O_2 + CO_3^{2-} = CO_4^{2-} \tag{2.11}$$

$$\frac{1}{2}\,O_2 + CO_3^{2-} = O_2^{2-} + CO_2 \tag{2.12}$$

Porous substrates play a prominent role in the permeation process. Geometry and surface modification can increase the gases permeability and all substrates physical properties like thickness, acidity, wettability, pore volume and size, and tortuosity impact permeability and efficiency of the membrane [91,92]. Porous stainless-steel supports have been proposed and investigated for their good electron conductivity and especially for their mechanical properties [93].

3 MATERIALS AND METHODS

The relationship between physicochemical features, performance of CO_2 sequestration and conversion, and the proposition of reaction pathways which will be shown in the next Chapters of this thesis, have been established by a thorough insight into the structural, microstructural, morphological properties of both natural olivine and steel slag waste. In this Chapter is reported a brief introduction to the experimental techniques and characterization methods adopted along the research activity carried out within this thesis.

3.1 X-Ray Diffraction (XRD) [94]

X-Ray Diffraction is a characterization technique based on the diffraction of X-rays by crystal structures. X-rays were discovered by Roentgen in 1895 but it was not thought as a potential investigation method for solid-state materials until 1912, when Max Von Laue proposed that X-rays passing through a crystal could be diffracted. He was, in fact, the first to fully realize that the wavelengths of X-ray radiation (10^{-10} m) are comparable with the distance separating lattice planes, which is a condition for the diffraction phenomenon to take place. In particular, a relationship stands between diffraction angle, wavelength and interplanar spacing, which is commonly known as the Bragg Law, summarized by the following Equation 3.1:

$$\lambda = 2dsin\theta \tag{3.1}$$

where λ is the wavelength of the X-rays, ϑ is the scattering angle and d is the distance between lattice planes.

This equation allows us to determine the specific direction of diffracted X-rays for which an enforcement of scattering amplitudes is observed that is related to the position of the scatterers among a family of parallel planes. By knowing the wavelength and its angle of incidence upon the sample, it is possible to retrieve the *d*-spacing

characterizing a certain family of planes that respects the condition of constructive interference stated by the Equation 3.1.

The original discovery of X-Ray diffraction was made using a single crystal rather than a powder specimen. The single crystals provide an unambiguous way in which a distance between lattice planes (d_{hkl}) can be chosen (fixed) and rotated (theta scanned) to yield a diffraction event.

X-rays are usually generated by bombarding a metal with high-energy electrons. The interaction between the metal and the electrons gives rise to different phenomena, among which the X-ray generation. The X-rays emitted are composed of a radiation with a continuous range of wavelengths, called Bremsstrahlung, generated by electron deceleration or path deviation due to electric charge interactions, superimposed to a radiation composed of few high-intensity sharp peaks, deriving from the relaxation of the electron structure of the metal atoms after an electron collision (Figure 3.1.1). When a bombarding electron collides with a core shell electron of the metal expelling it, the gap is filled by an electron from a superior shell. The relaxation process causes the emission of X-ray with an energy corresponding to the gap between the electron shells of the metal (Figure 3.1.2).

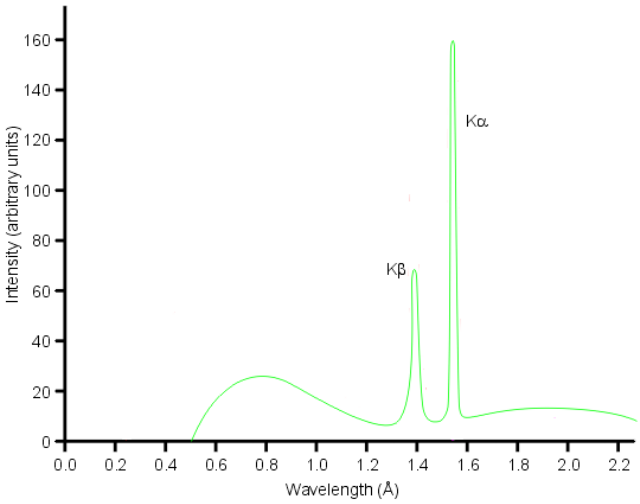

Figure 3.1.1: X-Ray emission spectra for Cu

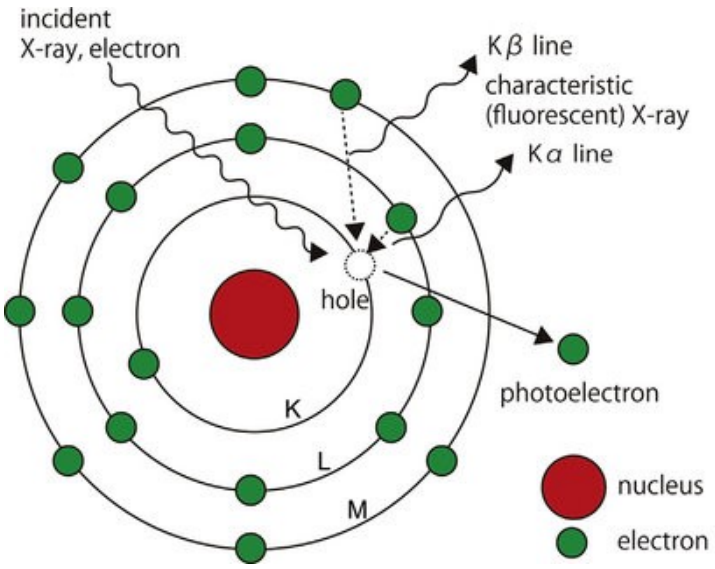

Figure 3.1.2: X-ray generation, Bohr atomic schematic representation [95]

Generated X-rays are diffracted by the lattice planes. The interpretation of diffracted X-ray and their correlation with crystal structures comes along with the theory allowing to relate atomic position in reciprocal 3D space to the real 3D space [96]. In particular, it is possible to link the position of the scatterers from the relative diffracted intensities collected in the Ewald sphere to the *real* 3-dimensional space. Crystallography, so, historically evolved by interpretating the crystal structures with the 14 Bravais lattices (Figure 3.1.3). The crystals were hence considered as a periodical arrangement of atoms or molecules located in correspondence of the lattice points allowing to define an arbitrary origin anywhere in that pattern. The smallest space between adjacent lattice points that can undergo a translation operation along the three crystallographic axes and still fits the reciprocal space without producing any overlapping or voids is defined as unit cell.

The lattices are classified according to their symmetric properties, grouping the crystals according to the combination of symmetry operations (32 point groups) that they possess. The number of total possible operations that account for the translational periodicity of a 3-D crystal is 230; they are referred as *crystallographic space groups*.

Lattice System	Primitive	Base-Centered	Body-Centered	Face-Centered
Triclinic	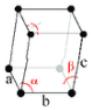 $P\bar{1}$			
Monoclinic	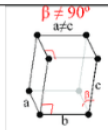 $P2/m$	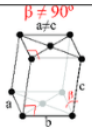 $C2/m$		
Orthorhombic	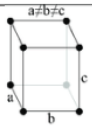 $Pmmm$	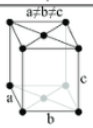 $Cmmm$	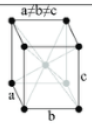 $Immm$	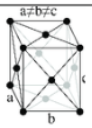 $Fmmm$
Tetragonal	 $P4/mmm$		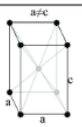 $I4/mmm$	
Rhombohedral	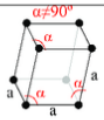 $R\bar{3}m$			
Hexagonal	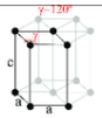 $P6/mmm$			
Cubic	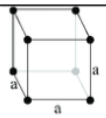 $Pm\bar{3}m$		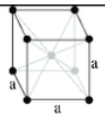 $Im\bar{3}m$	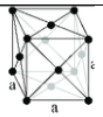 $Fm\bar{3}m$

Figure 3.1.3: the 14 Bravais lattices gathered either by lattice system (rows) or by centring type (columns).

The density of a crystal and the site fractional coordinates determine the number of site able to arrange atomic species inside the unit cell for the 7 classified geometries, always respecting the limitations imposed by the symmetry operation according to the space group. Therefore, the position and the number of electrons for each scatterer affects the intensity of the diffracted signal.

All the information regarding a unit cell of a crystal is collected in crystallography into the Crystallography Information File (CIF files). The CIF files report, for a selected crystal structure, the space group, the lattice parameters of the unit cell, the occupancy of each atomic species expressed as spatial fractional coordinates, multiplicity, etc…

X-Ray Diffraction allows to determine the qualitative phase composition of a sample by comparing a measured pattern, gathering a characteristic sequence of diffraction peaks, to CIF-file databases (search and match analysis) but also to determine quantitative data of phase abundancy and microstructural features.

The quantitative analysis of XRD experimental data can be extracted through modelling with Rietveld method. The Rietveld method is a refinement method for structure solution available for multiphase samples firstly reported in 1969 [97]. The Rietveld method uses the least squares approach to bend a theoretical line profile until it matches the experimental data profile. In this method the weight fraction (w_i) of each crystalline phase in a mixture can be calculated from the following equation:

$$\frac{w_i}{\sum_j w_j} = \frac{S_i(Z_i M_i V_i)}{\sum_j S_j(Z_j M_j V_j)} \tag{3.2}$$

where S_i is the refined scale factor, Z_i is the number of formula units in the unit cell, M_i is the mass of the unit formula and V_i is the elementary cell volume. Quantitative phase analysis using the Rietveld method relies upon the normalization condition $\sum_i w_i = 1$. This normalization condition is valid when the mixture does not contain amorphous phases [98].

XRD analysis were performed with the Rigaku SMARTLAB diffractometer with a Cu rotating anode, working at a voltage of 40 kV and a current of 100 mA (Figure 3.1.4). The diffractometer is equipped with a graphite monochromator in the diffracted beam and a detector based on a scintillation tube. The quantitative phase composition and structure and microstructure parameters were determined by the application of Rietveld refinement on the experimental pattern with the aid of the software MAUD. MAUD (Material Analysis Using Diffraction) is an applicative developed by L. Lutterotti,

available for XRD structure parameters refinement based on the Rietveld method [99]. It provides a friendly access to structural parameter refinement control in order to reach a good accordance between experimental data and fit within the hypothesized electron function density in the unit cell. The parameters taken into account during the refinement were: i) cell parameters, ii) crystallite size, iii) root mean square microstrain, iv) atomic position and v) temperature factor B. The starting crystal structures for Rietveld refinements have been selected among the crystallographic information files (CIF) available in the Crystallography Open Database (COD) and the Inorganic Crystal Structure Database (ICSD). The selected CIFs are reported in the following Table.

Table 3.1.1: CIF

Name	Chemical formula	Database	Database identification number
Forsterite	$Fe_{0.2}Mg_{1.8}SiO4$	COD	9000166
Enstatite ferroan	$Fe_{0.3}Mg_{0.7}SiO_3$	COD	1011238
Clinochlore	$Mg_{4.96}Fe_{0.33}Al_{1.7}Mg_{0.3}Si_{3.02}O_{18}H_8$	COD	0001619
Anatase	TiO_2	COD	1526931
Rutile	TiO_2	COD	1530150
Vermiculite	$Al_{3.36}Ca_{0.86}Fe_{0.41}H_{16.74}Mg_{4.04}O_{30.42}Si_{5.53}Ti_{0.08}$	COD	1001031
Clinoclorite	$Mg_5Al_2Si_3O_{18}H_8$	COD	1011015
NiO	NiO	COD	1010093
Nesquehonite	$MgCO_3{\cdot}3H_2O$	COD	9012401
Larnite	Ca_2SiO_4	COD	9012789
Wurstite	FeO	COD	1011169
Magnetite	Fe_3O_4	COD	1011032
Brownmillerite	$Ca_2(Al,Fe)_2O_5$	COD	1008724
Quartz	SiO_2	COD	1011159
Calcite	$CaCO_3$	COD	1547347
Aragonite	$CaCO_3$	ICSD	32100

The quality of the accordance between the experimental and calculated data was evaluated using as numerical criterion the Rwp parameter (weighted-pattern factor) [100].

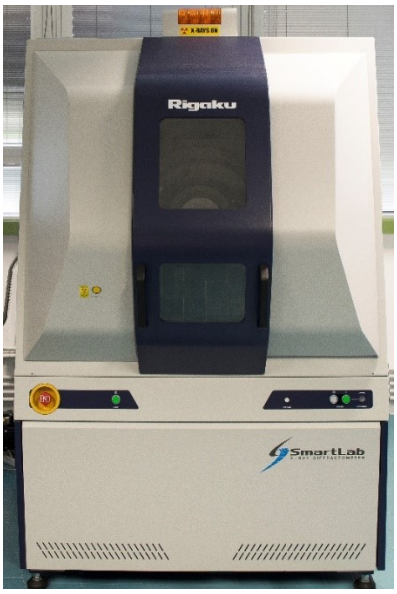

Figure 3.1.4: Rigaku SMARTLAB diffractometer, CeSar laboratories, University of Sassari

3.2 Electron Microscopy [101]

Electron microscopy is an imaging characterization technique based on the interaction between a beam of electron and a specimen, in order to gain information about morphology, structure and composition. At first electron microscopy was developed to overcome the limitation of optical microscopy in terms of magnification, due to the physics of light. We must keep in mind that smallest wavelengths of irradiation sources allow for the resolution of the image to be increased. The resolution (*r*) is defined by the equation $r = \frac{\lambda}{2NA}$ where λ is the imaging wavelength and *NA* is the objective numerical aperture. Thanks to their unparalleled resolution/contrast and versatility, Scanning electron microscopy (SEM) and Transmission Electron Microscopy (TEM) have become ubiquitous techniques for morphological characterization of solid materials.

3.2.1 Scanning Electron Microscopy (SEM)[102]

Scanning electron microscopy (SEM) is a characterization technique that produces images of a sample by scanning the surface with a focused beam of electrons. The

electrons interact with atoms in the sample, producing various signals that contain information about the surface topography and composition of the sample. The backscattered and the secondary electrons generated with a focused electron beam can be thus detected to reconstruct the morphology and topography of the sample.

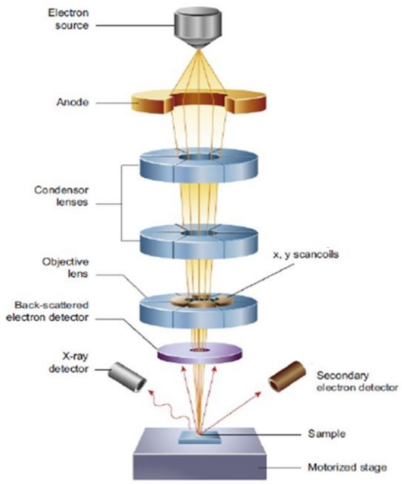

Figure 3.2.1: *Scheme showing the components in a basic SEM*

The electron beam is generated by an electron gun. Tungsten electrode, Lanthanum Hexaboride and field emission gun (FEG) are the most commonly used guns for generating the stable electron beam with adequate current, small pot size, adjustable energy and small energy dispersion. The electron beam then travels in a vacuum column through electromagnetic fields and lenses able to focus it on the sample (Figure 3.2.1)

The interaction of the electrons with a specimen causes an energy loss due to random scattering and adsorption phenomena inside a teardrop shaped volume of the sample (Figure 3.2.2). The size of the interaction volume depends on electron landing energy, atomic number, and density of the sample under analysis. Various phenomena arise from the interaction between the electron beam and a sample: the emission of Auger electrons, elastically backscattered electron, secondary electrons, characteristic X-rays, cathodoluminescence, continuum X-rays (Bremsstrahlung). They arise from different

region of the sample and all of them, when detected, could allow us to obtain different information about the sample morphology and chemical composition.

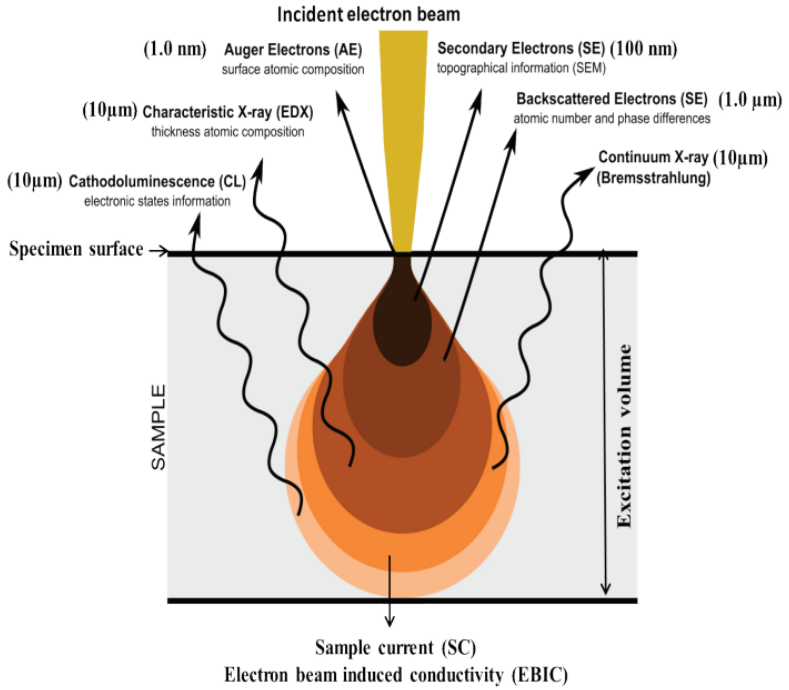

Figure 3.2.2: Electron-sample interaction profile [101]

Secondary electrons are produced by the ionization of the atoms in the specimen after the primary electron beam strikes the surface. The volume of penetration and the corresponding volume of the sample investigated depend on the energy of the primary electron beam, as well as the atomic number of the atoms in the sample. Secondary electrons can provide complementary information about the morphology and topography of a sample with a resolution (r) < 10 nm. These electrons are characterized by a low energy (0 to 50 eV).

On the other hand, backscattered electrons are generated by elastic diffusion. They are characterized by a higher energy with respect to the secondary electrons, providing information related to layers below the surface. Backscattered electrons are very sensitive to the variation of the atomic number: indeed, elements with high atomic

number give off more backscattered electrons, hence appearing brighter than elements featuring lower atomic number.

SEM imaging has been performed with the scanning electron FEI Q250 microscope (Figure 3.2.3).

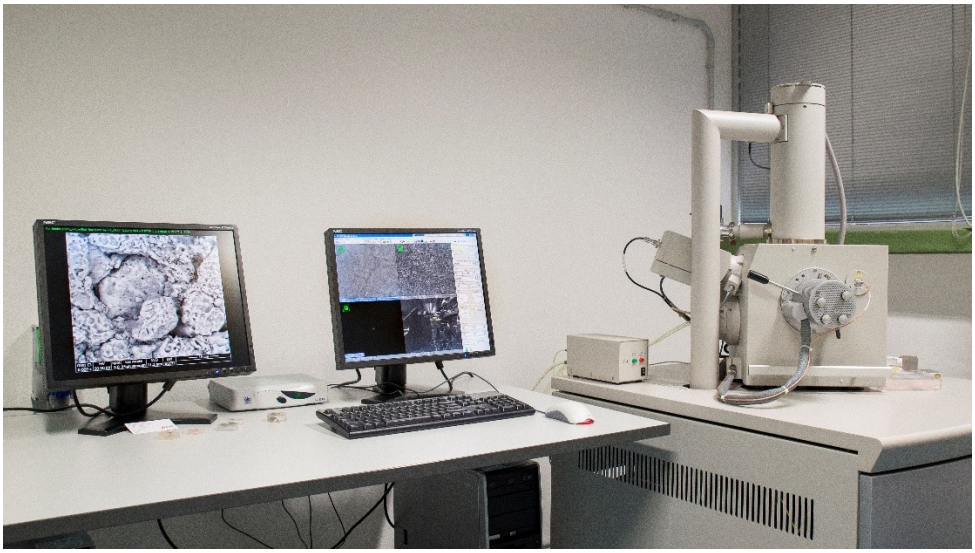

Figure 3.2.3: FEI Q250 microscope, CeSar laboratories, University of Sassari

3.2.2 Transmission electron microscopy (TEM) [103]

The Transmission Electron Microscopy (TEM) is based on the phenomena of electronic diffraction. The first TEM experiment was conducted in 1930s [104] substituting the illumination source and condenser lens of an optical microscope with an electron beam and electromagnetic coils, respectively. The electrons are accelerated by the electromagnetic coils and then interact with the material allowing the detection of the spatial distribution. The images obtained are the bidimensional projections of the 3-D structures.

TEM instruments are equipped with electron sources similar to the ones previously mentioned for SEM, even though electrons are accelerated at much higher energy (80

to 300 keV). The so-accelerated electrons are directed along the microscope column, diverted, and focused by some electromagnetic lenses and, after the interaction with the sample, they are projected on a fluorescent screen or, in modern instruments, revealed by a CCD sensor.

TEM are equipped with quadrupoles able to vary the beam direction (beam tilt) and pairs of quadruples able to divert the beam while maintaining a parallel direction (beam shift). A set-up of the main components of TEM can be observed in Figure 3.2.4.

The apertures in the column allow for the beam to be partially blocked, therefore selecting particular angles (lens apertures), and areas of the sample (area apertures). The apertures allow selecting the most central part of the beam, minimizing the aberrations. In modern TEM, all aberrations can be compensated and therefore corrected, at least in part, to obtain a better quality of the final image.

The intensities revealed after electron beam interaction with the specimen are related to the morphology and thickness of material, but also, for example, to the type of material (because of differences in atomic number and density of charge). There are various imaging techniques which reveal electrons at different angles. The techniques are mainly two: Bright field (BF) and Dark field (DF). The images obtained in BF use the electrons of the direct beam (the central spot of the Laue Zone of Zero order), while those in DF are obtained by the selection of the diffracted electrons by means of a decentralized aperture from the central beam.

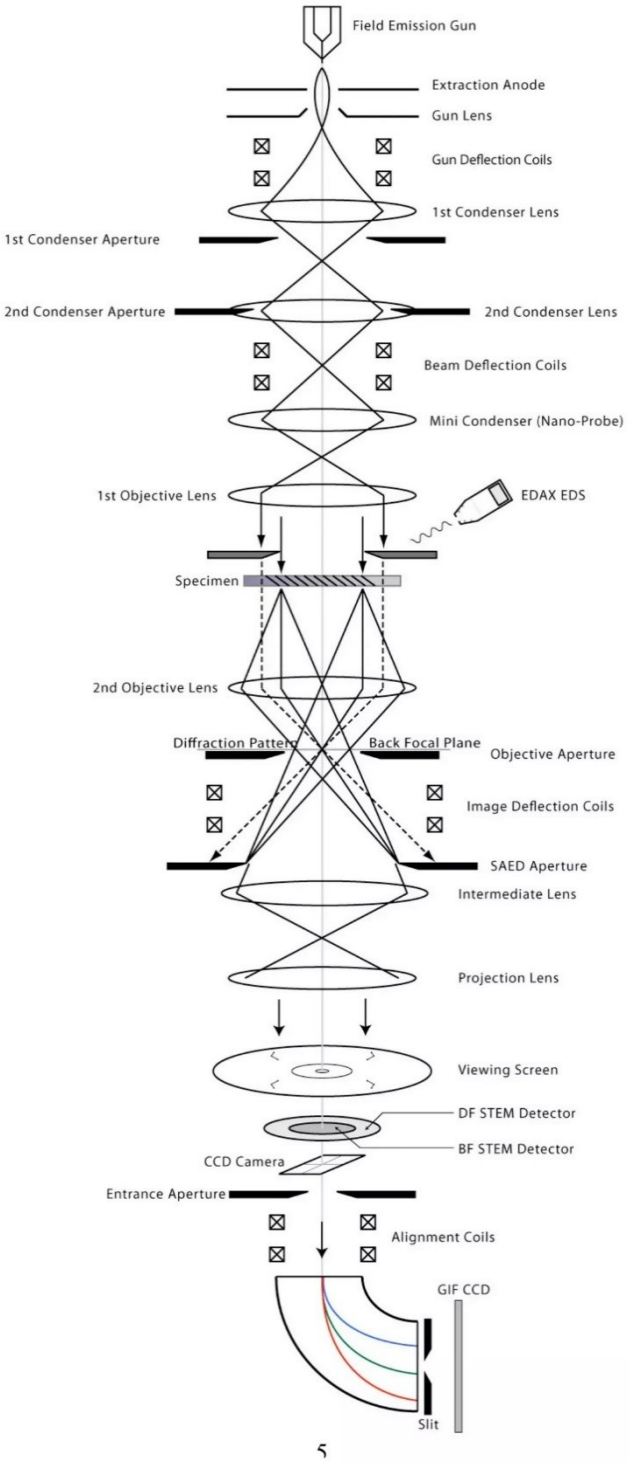

Figure 3.2.4 Scheme showing the components in a basic TEM [105]

The transmission electron microscope measurements performed in the frame of the present thesis have been collected by using a Fei Technai G2 F20 Twin TMP, whose picture is reported in Figure 3.2.5.

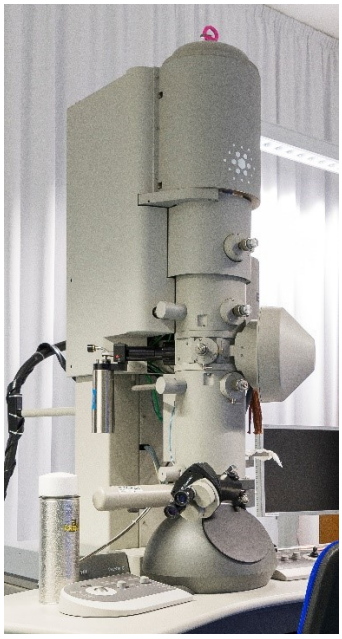

Figure 3.2.5: FEI Technai G20 F20 Twin TMP, CeSar laboratories, University of Sassari

3.3 Energy Dispersive X-Ray Spectrometry (EDS) [106]

The energy dispersive X-ray spectrometry is a characterization technique often associated with a TEM and SEM instruments. The EDS techniques is based on the analysis of characteristic X-ray generated by the interaction of the incident electron beam with the sample. Characteristic X-rays are generated likewise previously described in Chapter 3.1. The incident beam may excite an electron in an inner shell, ejecting it from the shell while creating an electron hole where the electron was. An electron from an outer, higher-energy shell then fills the hole, and the difference in energy between the higher energy shell and the lower energy shell may be released in the form of an X-ray. The number and energy of the X-rays emitted from a specimen can be measured by an energy-dispersive spectrometer. As the energies of the X-rays

are characteristic of the difference in energy between the two shells and of the atomic structure of the emitting element, EDS allows the elemental composition of the specimen to be measured. When coupled with secondary electron analysis an elemental map image can be acquired, thus enabling to identify uneven distributions in the atoms on the sample's surface.

EDS analysis have been acquired through EDAX (Energy Dispersive X-Ray Analysis) detector integrated on the FEI Q250 SEM (Figure 3.2.3).

3.4 Gas-Chromatographic analysis [107]

Chromatography is defined by IUPAC (International Union of Pure and Applied Chemistry) as a physical method of separation in which, the components to be separated are distributed between two phases, one of which is stationary (stationary phase) while the other (the mobile phase) moves in a definite direction [108]. The technique, in all its variants, proceed with the dissolution of the sample in the mobile phase that travels through the stationary phase. The different affinity and interactions between the different components of the sample and the mobile and stationary phases permits their separation and detection.

Gas chromatography, in particular, is the chromatography technique applied to gas samples. The mobile phase is an inert gas flow (carrier) while the stationary phase is solid. The mobile phase must not interact with the analytes, and the choice of the carrier is related both to the type of detector used and its efficiency under the specific experimental conditions. He or Ar flows are quite common carriers, due to their poor interaction with other gases. It is worth mentioning that H_2O and O_2 are some of the most common and damaging contaminants and their presence in the carrier gas can cause the degradation of the stationary phase in the column.

Different stationary phases have been employed in order to accurately separate the components of the gas mixture. The chemical nature of the stationary phase, which is

allocated in the column, the thickness, the length, and the diameter of the column are the key parameters to consider to achieve better separation efficiency.

Molecular sieves are packed columns filled with porous synthetic zeolites, with a dimension of the pores tuned to match the size of small molecules and are useful to separate inorganic gases with low molecular mass, such as H_2, O_2, N_2, CO or light hydrocarbons that can enter the pores.

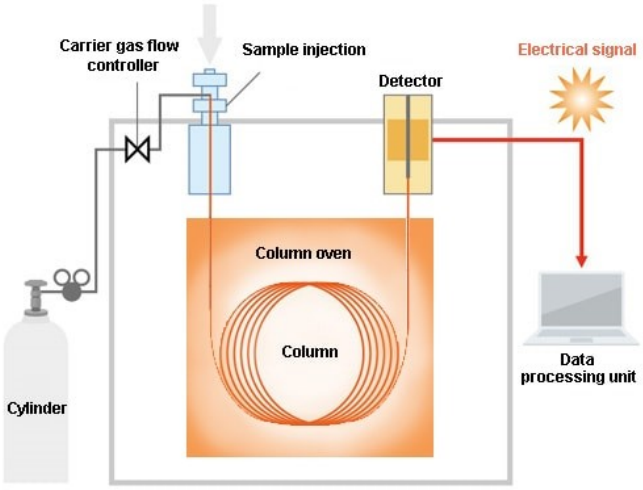

Figure 3.4.1: Gas chromatograph generic configuration

Conversely, capillary GC-columns are described as columns that have the stationary phase coating their inner surfaces rather than being packed into the cavity.

In GC-Chromatographers the column containing the stationary phase is enclosed in an oven that allow the temperature control during analysis (Figure 3.4.1). The sample is injected into the GC via an inlet valve (or *injector*), the mobile phase (*carrier gas*) passes through the inlet and drag the sample into the column. The chromatographic separation takes place when the mixture flows through the column and reaches the detector, which provides an electronic signal proportional to the concentration of the eluting analytes.

Specific detectors are suitable for the analysis of different classes of analytes. Flame Ionization detector (FID) is a detector where gaseous eluent is burnt in a flame

producing gas-phase ions. FID detectors typically work with He as carrier gas, they are unresponsive to air, H_2O or CO_2 but are very responsive to compounds containing carbon and hydrogen, providing high sensitivity (10^{-11} g) [109].

Thermal conductivity detector (TCD) provides a lower sensitivity (10^{-9}) but a wider range of application. This detector compares the thermal conductivities of two gas flows, the pure carrier and the gas plus the sample. Changes in the temperature of the electrically heated wires in the detector are affected by the thermal conductivity of the gas that flows around them. The changes are sensed as a change in electrical resistance and measured. TCD detectors are able to analyse inorganic gases (Ar, N_2, H_2, CO_2, CO and small hydrocarbons).

GC analyses were performed on GC Perkin Elmer 8500 equipped with a capillary column (GSQ 115-3432-J&W Scientific) and FID and TCD detectors respectively for hydrocarbons and CO_2 detection, and on Fisons 8000 equipped with a molecular sieve column (10 Å) with TCD detector able to detect H_2, O_2 and N_2.

3.5 Solar simulator [110]

Solar simulators are instrument able to simulate the wavelengths irradiated by the solar spectrum. The irradiance or intensity of light incident at the surface of the Earth's atmosphere on a plane normal to the angle of incidence is called Solar Constant. This is a way to measure the solar radiance, and it has been defined by the World Meteorological Organization to be 1367 $W \cdot m^{-2}$ [111]. The irradiance of the Sun on Earth's surface change depends on the absorption and scattering phenomena in the atmosphere. Below the atmosphere we can observe two components contributing to the solar irradiance: i) the direct radiation and ii) the scattered radiation from the sky including a part of radiation reflected back by the ground. The so called global (G) filters can be implemented to account for scattering sky and ground radiation.

Figure 3.5.1: Solar Simulator Sun 2000 ABET Technologies

The most used lamps to simulate the solar emission are the Xe lamp or Hg vapor lamps. Xe lamps contain two electrodes encapsuled in a glass bulb filled with Xe. A high voltage applied through the electrodes momentarily releases sparks that create light flashes. The emission spectra of a Xe source and the Sun are both close to the emission of a black body at 5800 K (Figure 3.5.1). The biggest difference is represented by the Xe lines present in the arc spectrum. The difference is pronounced in the range between 800 nm 1100 nm. The Air Mass filter reduces the effects so that the average level of specified bands matches solar levels better than 25 %. AM0 (Air Mass 0) regulates bands in order to simulate the level reached by solar irradiance above the atmosphere, whereas AM1.0 (air Mass 1.0) and AM1.5 (Air Mass 1.5) modify the visible and UV portion of the emission spectra in order to match the solar irradiance at sea level. Hg and Xe-Hg lamps provide better power levels for application in the UV region. The light emitted by the lamp is reflected and collimated by optical means into the irradiance window.

Solar Simulator are classified according to non-uniformity of spatial irradiance, spectral match to a reference spectral irradiance and temporal stability of irradiance.

The solar simulator Sun 2000 by Abet Technologies (Figure 3.5.1) used during the present project was calibrated to reproduce the median solar irradiance at median latitudes (A.M. 1.5G). The instrument is equipped with a Xe lamp, with a power of 150 W. The irradiance spectrum of the Sun 2000 solar simulator is reported in Figure 3.5.2.

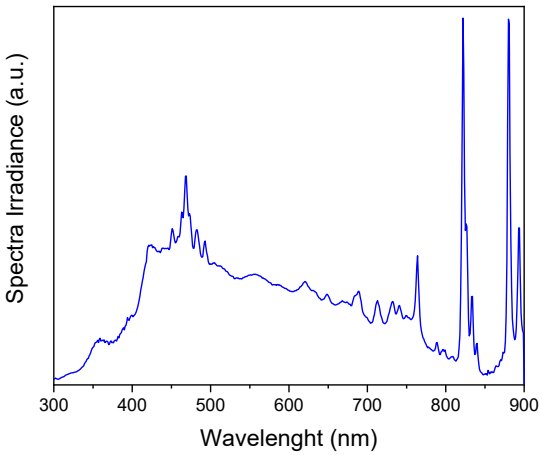

Figure 3.5.2: Irradiance spectrum of Solar Simulator Sun 2000 ABET Technologies

3.6 UV-vis spectroscopy

UV-vis spectroscopy is a widely known characterization technique based on the study of selectively absorption by molecules of radiation in the wavelength range between 10 nm and 780 nm. This wide range can be subdivided into far UV (10-200 nm), near UV (200-380 nm) and visible (380-780 nm). Near UV and visible regions are the most interesting by an analytical point of view [112].

The energy absorbed in the UV region produces changes in the electronic levels of a molecule. Indeed, as a molecule absorbs energy, an electron is promoted from an occupied molecular orbital to an unoccupied molecular one. Different transitions are triggered, among them, the most common are $\sigma \rightarrow \sigma^*$, $\pi \rightarrow \pi^*$, $n \rightarrow \sigma^*$ and $n \rightarrow \pi^*$.

UV/vis spectrometers usually measure the intensity of light passing through a sample solution and compare it to the intensity of the light source. The main components of

an UV/vis instrument are a light source, a sample holder, a dispersive device (monochromator) and a detector. Tungsten, quartz-iodine and tungsten-halogen lamps are used as source of radiation for the visible region, while deuterium or mercury vapor lamp are implemented for the UV region.

UV/vis measurements can be also used to determine the concentration of a specimen in solution by application of the Beer-Lambert law:

$$A = \varepsilon C d \tag{3.3}$$

where *A* is the absorbance, *ε* is the extinction coefficient, *C* the concentration and *d* the path length [113,114].

Reflectance UV/vis measurements allow to work with solid samples instead of liquid solutions. These instruments measure the light reflected by a solid sample after being irradiated. The reflected light consists of *specular* reflected light and *diffuse* reflected light. The light sent to the sample is called incident light while the angle between the incident light and the sample is called angle of incidence (Figure 3.6.1).

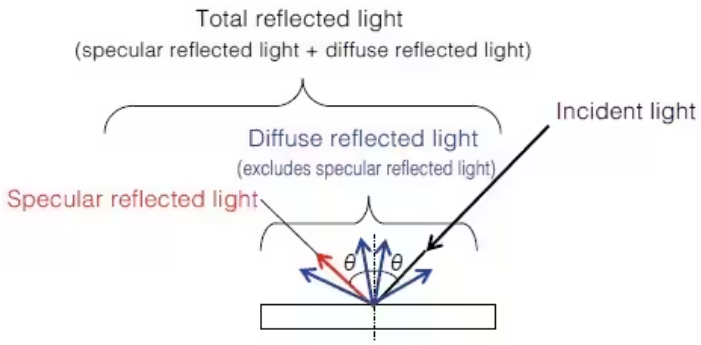

Figure 3.6.1: Reflectance UV/vis measurements scheme [114]

The specular reflected light comes from shiny mirror-like surfaces at the same angle as the incident angle, whereas the diffuse reflected light is reflected in random directions from rough surfaces. Reflectance measurements measure either the relative or the absolute reflected light, with measurement values expressed in terms of reflectance. Relative reflectance measurements calculate the proportional amount of reflected

light measured from a sample surface, with respect to the amount of reflected light measured from a reference plate, made by barium sulphate or simply by a mirror. The relative reflectance is calculated assuming that the reference plate has a reflectance of 100 %. Therefore, it is very important to manage reference plates properly because different reflectance values can be obtained if these are substituted or if they become contaminated or change characteristics. In contrast, absolute reflectance measurements calculate the proportional amount of reflected light relative to the amount of light measured directly from a light source, without using a reference plate. Reflectance measurement values are based on assuming a 100 % reflectance for air. Absolute reflectance measurements allow determining the true reflectance of samples, which is referred to as absolute reflectance.

Diffuse reflectance measurements with UV-vis spectrometer can be used to determine the optical properties of a powder material. It is possible to calculate the energy band gap of a material by applying the Kubelka-Munk theory. Proposed in 1931 by Paul Kubelka and Franz Munk, it describes the behaviour of light travelling through a light scattering sample. It is based on two different equations:

$$-di = -(S + K)idx + Sjdx \tag{3.4}$$

$$dj = -(S + K)jdx + Sidx \tag{3.5}$$

where *i* and *j* are the intensities of light travelling inside the sample towards its unilluminated and illuminated surfaces, respectively, *dx* is the differential part along the light path, *S* is the scattering coefficient and *K* is the adsorption coefficient. Kubelka-Munk theory holds its validity only when the particle size is smaller or equal to the wavelength of the incident light and the diffuse reflection no longer permits the secondary contributions of reflections, refractions and diffractions.

If this assumption is fulfilled, the Kubelka-Munk equation for any wavelength can be written as:

$$\frac{K}{S} = \frac{(1-R_\infty)^2}{2R_\infty} = F(R_\infty) \tag{3.6}$$

where (R_∞) is the diffuse reflectance and $F(R_\infty)$ is called the Kubelka-Munk function.

Energy band gap and adsorption coefficient are related via the Tauc plot relation:

$$ahv = A(hv - E_g)^n \tag{3.7}$$

where a is the linear absorption coefficient and $\mathrm{n} = \frac{1}{2}$ for direct energy band gap materials.

Considering perfect diffuse radiation scattering, K = 2a and if S is constant respect to the wavelength Kubelka-Munk function is proportional to the adsorption coefficient a.

$$[F(R_\infty)hv]^2 = A(hv - E_g) \tag{3.8}$$

This relation enables the calculation of the energy band gap (E_g) by extrapolating the intercept between the linear interpolation of the experimental data and the x axis on the $[F(\mathrm{R}_\infty)hv]^2$ vs hv plot (Figure 3.6.2).

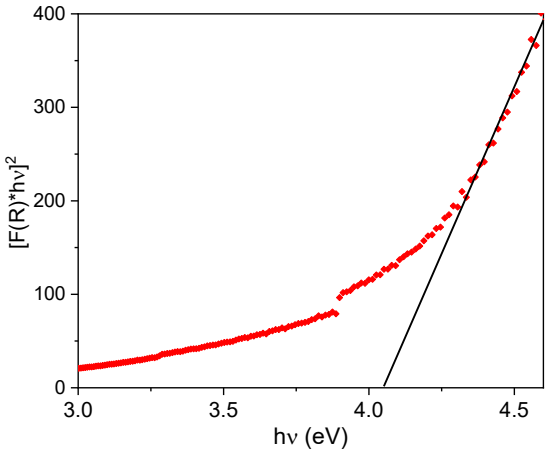

Figure 3.6.2: Energy band gap evaluation on $[F(R_\infty)hv]^2$ vs hv plot

UV-Vis measurements were performed on Perkin Elmer Lambda 650 UV/VIS spectrometer (Figure 3.6.3).

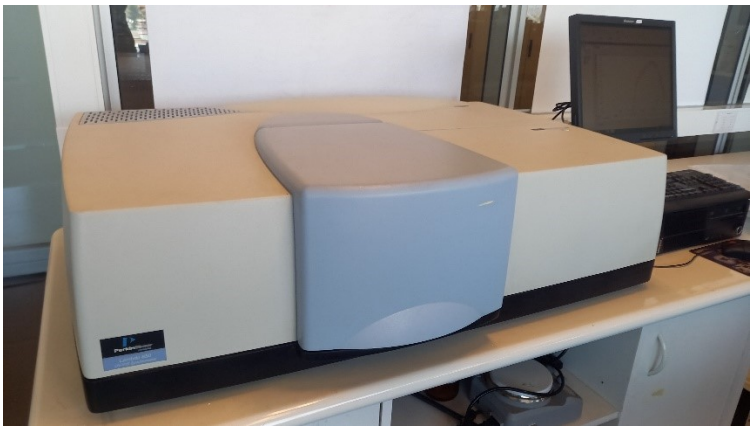

Figure 3.6.3: UV/vis spectrometer Perkin Elmer Lambda 650, Universidad de Chile, Santiago (Chile)

3.7 Infrared Spectroscopy [115]

Fourier transformed Infrared Spectroscopy (FT-IR) is a spectroscopy that studies the interaction between infrared light frequencies (0.7 µm – 300 µm) and matter. The mid-infrared region (MIRS), corresponding to wavelengths from 2.5 µm and 25 µm (4000 to 400 cm^{-1}), allows the study of fundamental vibrations of small molecules that cause a change in their dipole moment.

Infrared spectroscopy is a technique based on the vibrations of the atoms of a molecule. The radiation passing through a sample can be partially absorbed triggering atom vibrations in the molecules of the sample itself. In order for a molecule to show infrared absorption, the electric dipole moment of the molecule must change during the vibration (Selection rule for infrared spectroscopy). Infrared absorptions are not infinitely narrow, and several factors contribute to the broadening such as collisions between molecules and the finite lifetime of the states involved in the transition. Vibrations can involve a change in bond length (stretching) or bond angles (bending). Depending on the in-phase or out-of-phase stretch, stretching vibrations of molecules with same terminal atoms (like H_2O), can be further divided in symmetrical and

asymmetrical stretching, respectively. Bending vibrations can be subdivided in in-plane and out-of-plane ones. The intensity of IR signals depends on the dipole moment change, the larger the dipole moment change caused by a vibration, the more intense is the signal detected.

FT-IR Spectrometers are based on the interference of radiation between two beams to yield an interferogram. This is produced as a function of the change of the pathlength between the two beams. The two domains, distance and frequency can be interconverted by the use of the mathematical method of Fourier transformation.

Attenuated total reflectance (ATR) spectroscopy is based on the total internal reflection phenomenon. The beam of IR radiation from the source of the instrument undergoes total internal reflection entering in a crystal when the angle of incidence at the interface between the sample and the crystal is greater than the critical angle. The critical angle is dependent on the refractive indices of the two surfaces. The radiation beam loses energy due to selective absorption from the sample in close contact with the reflecting surface, so losing energy at the wavelength where the material under analysis absorbs. The resulting attenuated radiation is measured and plotted as a function of wavelength by the spectrometer and give rise to the absorption spectral characteristics of the sample. The depth of penetration in ATR spectroscopy is a function of the wavelength, λ, the refractive index of the crystal, n, and the angle of incident radiation, ϑ. Different materials are commonly used for their properties as crystal for ATR spectroscopy (Ge, ZnSe, KRS-5). ZnSe as a useful range between 20000 and 500 cm^{-1}, is insoluble in water, organic solvent and dilute acids and bases.

The mid-infrared spectrum (4000-400 cm^{-1}) can be approximately divided into four regions. The X-H stretching region, between 4000 and 2500 cm^{-1}, the triple bond region, from 2500 to 2000 cm^{-1}, the double bond region, from 2000 to 1500 cm^{-1} and the so-called fingerprint region, below 1500 cm^{-1}.

FT-IR analyses were conducted in solid-state on the JASCO FT/IR-4600 in ATR mode with ZnSe crystal (Figure 3.7.1).

Figure 3.7.1: JASCO FT/IR-4600 instrument

3.8 Physisorption phenomenon analysis and B.E.T. method

The gas adsorption analysis is widely used to evaluate the surface area and the porosity of a solid material. The solid sample is exposed to gases or vapours at different experimental conditions while evaluating the weight or the sample volume uptake. Sample characteristics such as porosity, total pore volume and pore size distribution can be gathered by those analysis. The Brunauer-Emmet-Teller (BET) theory, that aim to explain the physical adsorption of gas molecules on a solid surface, proposed in 1938 by Stephen Brunauer, Paul Hugh Emmett and Edward Teller, extended the concept of Langmuir theory, allowing the correlation of the measurements of adsorption phenomenon to relevant physical properties [116]. The Langmuir theory is able to explain a monolayer molecular adsorption., The BET theory is able to account for multilayer adsorption under a certain number of hypothesis: i) the formation of an infinite layer of gas molecules adsorbed on the solid, ii) the interaction of gas molecule only with adjacent layers, iii) the enthalpy of adsorption of the first layer is constant

and greater than the second layer, iv) the enthalpy of adsorption of the second layer is the same as the enthalpy of liquefaction. The BET theory is able to evaluate parameters like: total surface area, pore-size distribution, micropore analysis and porosity.

The physisorption process is characterized by low interaction energy and thermodynamic reversibility. BET equation can correlate surface coverage (ϑ) with the probe gas relative pressure, calculated as the ratio between the partial vapour pressure of adsorbate gas (P) and the saturation pressure of adsorbate gas (P_0).

$$\theta = \frac{CP}{\left(1-\frac{P}{P_0}\right)(P_0+P(C-1))} \tag{3.9}$$

where C is a constant referred as the BET constant. The above equation can be rearranged as:

$$\frac{\frac{P}{P_0}}{v\left[1-\left(\frac{P}{P_0}\right)\right]} = \frac{C-1}{v_m C}\left(\frac{P}{P_0}\right) + \frac{1}{v_m C} \tag{3.10}$$

where v_m is the monolayer adsorbed gas quantity and v the adsorbed gas quantity.

Total and specific surface area can be than calculated as follow:

$$S_{tot} = \frac{v_m N s}{V} \tag{3.11}$$

$$S_{BET} = \frac{S_{tot}}{a} \tag{3.12}$$

Where N is the Avogadro number, s is the cross section of the adsorbate, V the molar volume of the adsorbate gas and a is the mass of the solid sample or adsorbent.

The most common probe gas for physisorption analysis is N_2, exposed with the material under analysis, at the temperature of gas-liquid N_2 equilibrium (77 K). Other gases like Kr or Ar are used for low specific surface area measurements. The initial part (low P/P_0) of a typical adsorption isotherm can provide information about surface area since it depends by the monolayer coverage on the material surface, while the upper part (high P/P_0) provides information about the total pore volume. BET analysis allows the characterization of materials with pore sizes between 2 nm and 150 nm.

Physisorption analysis were performed with the Fisons Sorptomatic 1990 apparatus.

Figure 3.8.1: Fisons Sorptomatic 1990

3.9 Pulse chemisorption method

Isothermal chemisorption can be evaluated via dynamic chemisorption. The dynamic or flowing gas chemisorption technique operates at ambient pressure. After sample cleaning, small injections of accurately know quantities of adsorptive are administrated in pulses until the sample is saturated, thus the name, pulse chemisorption [117].

The instruments can follow the quantity of adsorptive that is not chemisorbed on the sample via TCD detector. This quantity is subtracted from the injected quantity yielding the quantity adsorbed from each injection. The sum of gas adsorbed after each injection determine the capacity of the sample mass. Since the endpoint (saturation) is the only point measured, the number of injections may be only a few and there are no pressure changes.

Temperature programmed chemisorption analysers have been recognized as valuable tools for characterizing catalysts. The method is sometimes simply referred to as temperature-programmed reactions, and includes Temperature-Programmed

Desorption (TPD), Temperature Programmed Reduction (TPR) and Temperature Programmed Oxidation (TPO). The dynamic chemisorption method is particularly suitable for temperature program analyses.

Pulse chemisorption analysis is a technique usually applied to determine active surface area, percent metal dispersion or active metal particle size by applying measured doses of reactant gas to the sample. At low temperatures pulse chemisorption analysis can allow the evaluation of the adsorbed gas quantity.

Pulse chemisorption analysis were performed with Thermo Scientific TPD/R/O 1100 catalytic surface analyser instrument, with automatic pulse gas injections (Figure 3.9.1).

Figure 3.9.1: TPD/R/O 1100, Sotacarbo Scpa laboratories, Carbonia (Italy)

3.10 Dynamic light scattering (DLS) [118,119]

Dynamic light scattering (DLS) is a characterization technique that deals with the study of how coherent light, scattered by a solution containing diffusing particles, changes with time. The sample is exposed to a monochromatic wavelenght and the detector is able to collect the scattered intensities. The time-correlation function of the scattered intensities provides information about the diffusivity and the size of the suspended particles. Light scattering was firstly developed and described by John Tyndall for colloidal suspension, only later John William Strutt Rayleigh described the scattering

from particles smaller that the incident light wavelength, the so-called Rayleigh scattering [120].

DLS instruments basic set-up is shown in Figure 3.10.1. A parallel beam of coherent light is directed onto a dilute colloidal suspension. If the fluid contains scattering particles, many speckles, which are tiny but macroscopically visible light dots, will form on the screen behind the sample, the so-called speckle pattern. The speckles will be visible at all scattering angles, θ, that lies in the plane of the incoming and unscattered outgoing beam. The speckle pattern generates from constructive and destructive interference of the light scattered by individual particles. As the particles diffuse in time, the conditions for constructive and destructive interference change, making the speckles move. The detector, under a fixed scattering angle, is able to evaluate the variation of the intensity of a speckle in time.

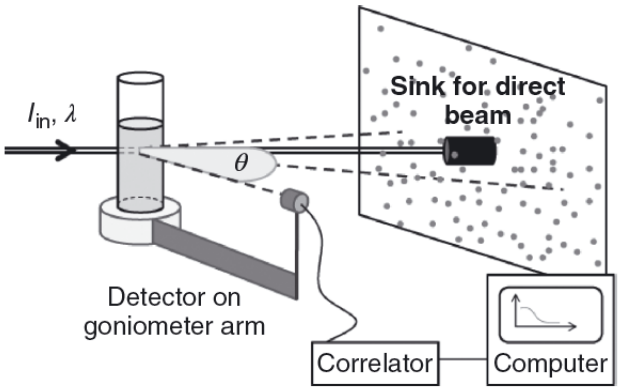

Figure 3.10.1: DLS basic set-up [118]

In a DLS experiments, it is necessary to measure the intensity of the autocorrelation function, $g^2(\tau)$. The autocorrelation function for very diluted monodisperse samples is related to the diffusion coefficient *D* of the scattering particles. The diffusion coefficient can be used in the Stokes-Einstein equation in order to evaluate the solvodynamic radii of the scattering particles.

$$D = \frac{k_B T}{6\pi\eta R_s} \tag{3.13}$$

where k_B is the Boltzmann constant, T is the temperature, η is the viscosity of the solvent and R_s is the solvodynamic radius. The Stokes-Einstein equation was firstly described for non-interacting spherical particles dispersed in water, therefore can be assumed valid only for very dilute solutions where the motion of the particles can be considered uncorrelated.

In general samples does not perfectly fit the assumption made by the Stokes-Einstein equation, having some spread in diameter, and sometimes in shape, or density. The size distribution can be taken into account by multiplying the electric-field correlation function with a normalized distribution function.

DLS measurements were performed on Malvern Zetasizer Nano S90 (Figure 3.10.2) with red light laser beam (632.8 nm).

Figure 3.10.2: Malvern Zetasizer Nano S90

4 RESULTS AND DISCUSSION - OLIVINE

As previously reported, the main goal of the thesis has been the study of CO_2 conversion processes induced by photochemical activation on silicate-based materials, including olivine and electric-arc steel slags. The present Chapter will focus on the investigation of both structural characteristics and reactivity of olivine-based materials. Bulk and surface features of pristine, modified, and exhausted olivine were evaluated by several instrumental techniques. The reactivity towards CO_2 conversion was tested under batch conditions, in a customized photochemical reactor, highlighting the potential efficacy of this approach for CO_2 conversion strategies. The whole pattern of experimental data and kinetic trends allowed us to suggest some mechanistic inferences relevant to CO_2 conversion processes.

4.1 Mineral olivine characterization

The survey of the experimental investigation started with the structural characterisation of pristine olivine, which was provided by Satef-HA. Phase composition, relative abundance, and microstructural features have been investigated via X-Ray Diffraction (XRD) analysis applying least squares refinement procedure, based on Rietveld method, for semi-quantitative evaluation, as described in the previous Chapter.

XRD reported in Figure 4.1.1 reveals the presence of three different phases in the pristine material, namely forsterite $(Mg_{0.8}Fe_{0.2})SiO_4$, enstatite ferroan $(Mg,Fe)SiO_3$ and clinochlore $(Mg_{4.66}Fe_{0.33})(Al_{0.7}Mg_{0.3})(Si_{3.02}Al)O_{10}(OH)_8$. The quantitative analysis shows that forsterite is the main component (90 wt. %), while the two other silicates, enstatite and clinochlore, are present with a relative abundance of 7 wt. % and 3.7 wt. %, respectively. Such a composition is not surprising, since these three phases are

commonly gathered in natural olivine. The detail of the estimated composition is reported in Table 4.1, together with the refined cell parameters for each phase.

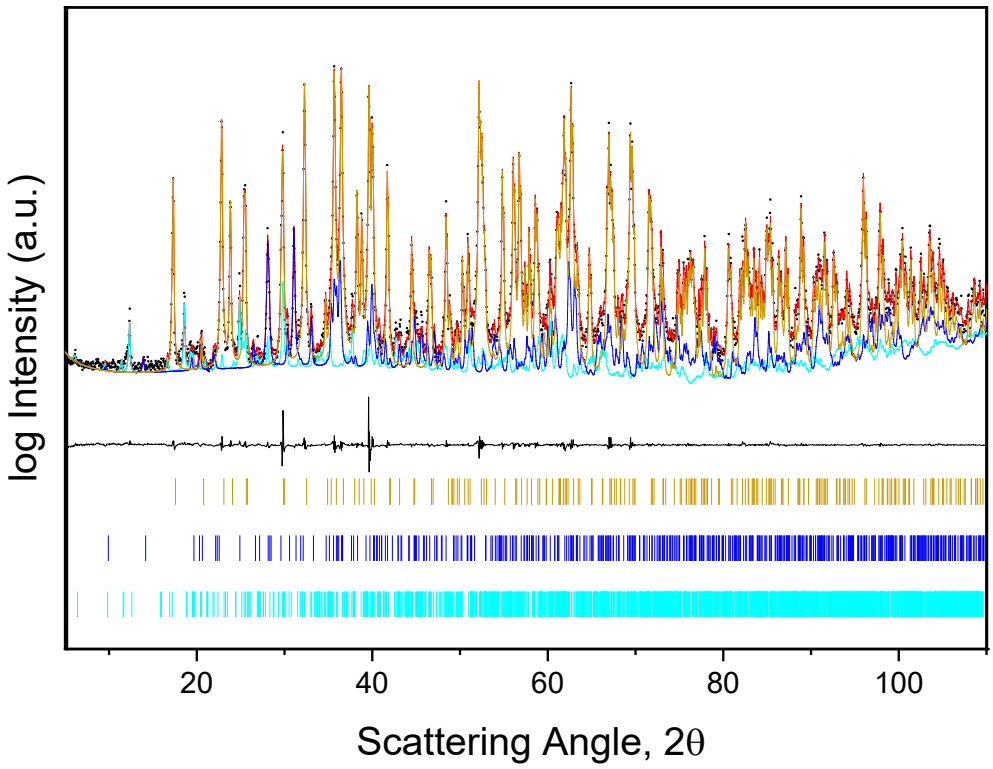

Figure 4.1.1: Characterization analysis of pristine mineral olivine: XRD measurement and Rietveld Refining. Experimental data (black dots), calculated intensity (red line), forsterite (ocher line), enstatite (blue line) and clinochlore (cyan line) are reported. The difference between experimental and calculated data in linear scale and the stick pattern for all the phases, listed in descending order as above, are provided

Table 4.1.1: Phase weight percentage and cell parameter calculated via Rietveld Refining on olivine powder XRD pattern, Rwp = 10.2

Crystalline phase	Wt %	Space Group	Cell parameters					
			a (Å)	b (Å)	c (Å)	α (°)	β (°)	γ (°)
Forsterite ($Fe_{0.2}Mg_{1.8}SiO_4$)	90 ± 1	*Pbnm*	4.76(3)	10.22(4)	5.99(4)	-	-	-
Enstatite ferroan ($Fe_{0.3}Mg_{0.7}SiO_3$)	7 ± 1	*Pbca*	18.24(7)	8.84(1)	5.19(4)	-	-	-
Clinochlore ($Mg_{4.96}Fe_{0.33}Al_{1.7}Mg_{0.3}Si_{3.02}O_{18}H_8$)	3.7 ± 0.2	$P\bar{1}$	5.36(1)	9.20(6)	14.43(8)	90.4(6)	97.9(3)	89.7(7)

Further structural inferences of as-received olivine were gained by FTIR spectroscopy: the analysis displayed in Figure 4.1.2 agrees with the data reported in the literature, showing the signals relevant to Si-O bonds [18,121]. In particular, the bands around 900 cm^{-1} are attributable to symmetrical and asymmetrical stretching of the Si-O bond, while the bands around 630 cm^{-1} pertain to Si-O symmetrical and asymmetrical bending.

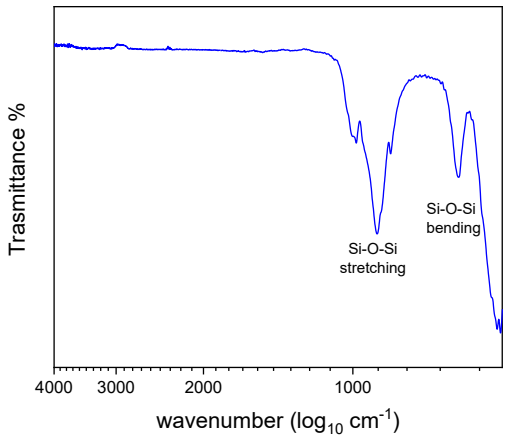

Figure 4.1.2: FTIR spectra of pristine olivine powders

N_2 physisorption analysis was conducted on the pristine olivine powders in order to evaluate the surface area; the relative isotherm is reported in Figure 4.1.3. The system is characterised by a isotherm of type III, and the value of specific surface area, as

estimated according to B.E.T. method, is equal to 4.81 m^2/g. The narrow hysteresis and the apparent lack of B point in the analysis, suggest a very low porosity of the powders.

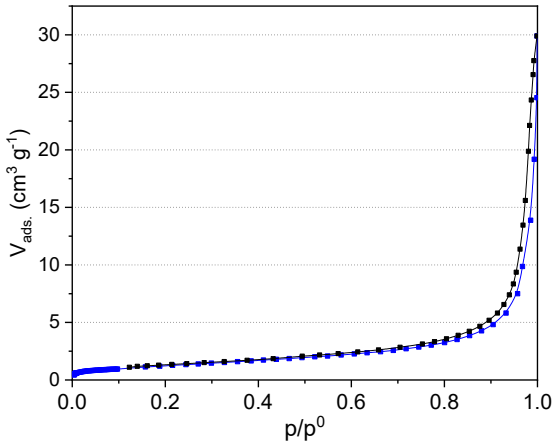

Figure 4.1.3: N_2 physisorption isotherm, adsorption data are reported in blue while desorption data are reported in black

Adsorbable CO_2 was quantified by pulse chemisorption analysis. The samples were purged with He flow (40 ml·min^{-1}) for 5 minutes before being heated to 450 °C with 10 °C·min^{-1} rate to desorb any gas contaminant. After 1 hour at 450 °C the temperature was decreased to the experimental one (40 °C) always under He flow. Pulse chemisorption analysis was held under 20 ml·min^{-1} He flow, sending to the sample 15 pulse of a gas mixture 10 % V/V CO_2/He. The gas not being adsorbed was measured via TCD detector. Mineral olivine was able to adsorb 4.3 ± 0.2 µmol of CO_2/g_{sample}. These experimental data agree with adsorbable CO_2 on comparable silicates materials [122].

As cited above, olivine is a component of mafic rocks, whose characteristics include the ability to induce basic reaction to water solution. olivine powders confirmed such behaviour, and the measured pH for olivine dispersed in H_2O is 9.0, beyond the experimental uncertainty.

The direct energy band gap associated with olivine was evaluated from UV-vis spectroscopy measurements using total reflectance method, and applying the Kubelka-Munk equation (Chapter 3.6) assuming perfect diffuse radiation scattering and the

scattering coefficient, S, constant respect to the wavelength [123]. The spectroscopic analysis is reported in Figure 4.1.4a; the direct energy band gap was evaluated, under these assumption with a linear regression on the plot *hv vs.* $[F(R)\cdot hv]^2$ (Figure 4.1.4b).

The mineral olivine is characterized by a direct energy band gap in solid-state of 4.2 eV. This energy corresponds to a wavelength of 293 nm, which lies within the range of wavelengths of UV-B. It is interesting to note that the wavelengths of UV-B, between 280 and 315 nm, are a portion of the solar spectra mostly adsorbed by ozone layer in Earth atmosphere. Therefore, these wavelengths do not reach the Earth surface and materials like olivine, characterised by the cited band gap, are not useful to harvest such a range of energy.

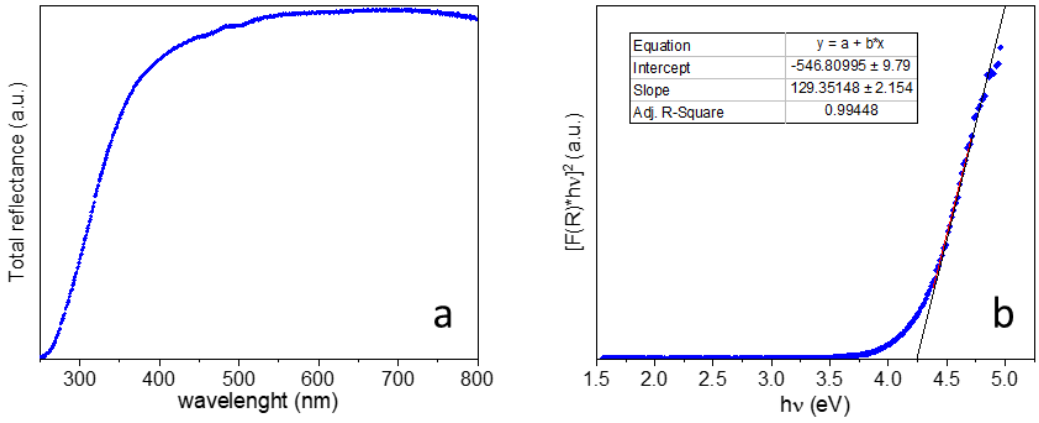

Figure 4.1.4: Total reflectance UV-vis analysis on olivine (a) and linear regression on total reflectance UV-vis measurements by application of the Kubelka-Munk theory for direct energy band gap evaluation (b)

4.2 Mineral olivine Modification by chemical doping

The electronic characteristics of olivine make it an inefficient system to harvest solar energy with wavelengths in the range of visible light, being only effective in a specific range UV, and it opens the possibility to a band gap modification through chemical doping and structural modification approaches, according to strategies reported in the literature [14] . With such aim, mineral olivine has been doped to decrease the value

of energy band gap and to allow for the activation of the CO_2 photoconversion process irradiating the material with wavelength included in the solar spectrum inside the Earth's atmosphere. Olivine has then been treated with different metal oxides (TiO_2, Cr_2O_3, NiO, Fe_3O_4) and metals (Fe, Ni). Olivine doping was pursued by both mechanical treatment processes and the impregnation method.

Modification by mechanical treatment was carried out by ball-milling the powders, using a SPEX mixer/mill with a steady rotational speed of 875 rpm, for 1 hour.

In the following Tables, some details of the measured variation of the band gap values are reported, as a function of the dopants.

Table 4.2.1: Direct Energy Band Gap measured through Kubelka-Munk theory application on Total Reflectance UV-vis measurements in solid-state (a), via Tauc plot from Absorbance Uv-vis measurements in solid-state (b), via Tauc plot from Absorbance UV-vis measurements in water-dispersed samples (c)

Material	Direct energy band gap (eV)		
	(a)	(b)	(c)
Pristine olivine	4.2(1)	3.94(5)	4.7(5)
TiO_2	3.6(2)		3(1)
Dopant (concentration)	Direct energy band gap (eV)		
	(a)	(b)	(c)
TiO_2 (10 wt. %)	3.48(5)	3.32(4)	4.1(6)
Fe_2O_3 (10 wt. %)			
Fe_3O_4 (10 wt. %)	4.27(5)		
Ni (10 wt. %)	5.51(4)		
Co (10 wt. %)	5.40(4)		
WO_3 (10 wt. %)			5.5(1)
GeO_2 (10 wt. %)			5.2(5)

The direct energy band gap associated with each doped material was evaluated via UV-vis measurements in solid-state and water dispersion (Table 4.2.1). Energy band gap was determined via Tauc Plot method for the spectra acquired in absorbance and via application of Kubelka-Munk theory for spectra acquired in total reflectance. The modification with pure metals like Ni and Co and oxides like GeO_2, WO_3 brought to an increase of the energy band gap of the material. The modification with Fe_3O_4 magnetite does not lower the energy band gap either. The modification with TiO_2 allows for lowering the energy band up to 3.5 eV. TiO_2-modified olivine was then selected as most promising candidate for photochemical activated CO_2 conversion, resulting a material with lower energy band gap then its pure components (olivine and TiO_2).

TiO_2-modified olivine was characterized by means of X-Ray Diffraction (Figure 4.2.1). XRD analysis highlights the presence of the added TiO_2 anatase phase together with forsterite, enstatite ferroan and clinochlore, which are the phases constituting the mineral olivine. No significant variation in the weight percentage ratio between the phases already present in the pristine mineral was observed after the ball-milling treatment. The weight percentage of TiO_2 anatase phase calculated by applying the Rietveld refinement is very close to the nominal percentage added, thus supporting the hypothesis of low Ti substitution in the olivine phases (Table 4.2.2). The lack of significant variations of the cell parameters of forsterite and enstatite ferroan phases support that hypothesis (Table 4.2.3).

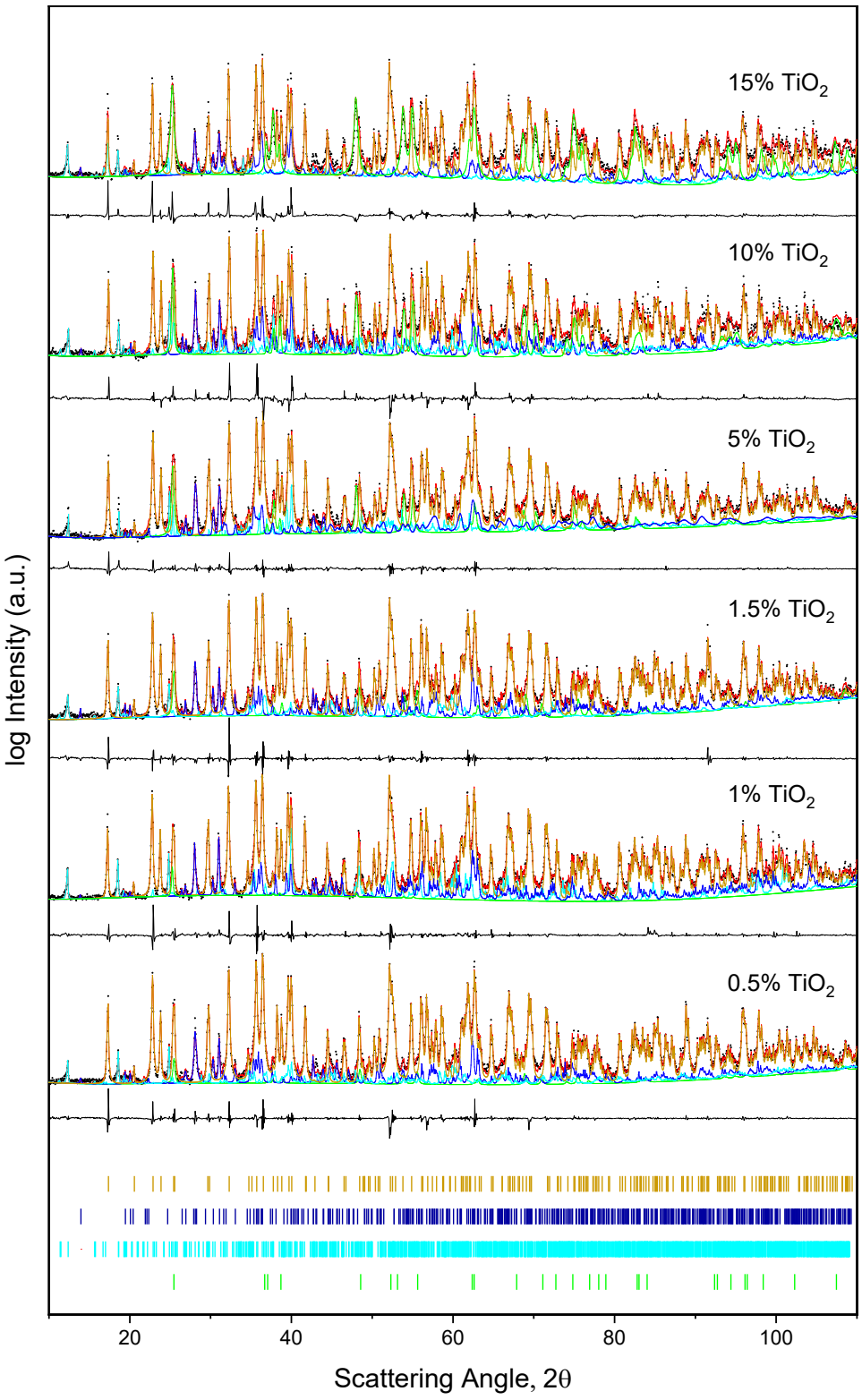
15% TiO2
10% TiO2
5% TiO2
1.5% TiO2
1% TiO2
0.5% TiO2
log Intensity (a.u.)
20
40
60
80
100
Scattering Angle, 2θ

Figure 4.2.1: XRD patterns for olivine-titania anatase materials prepared via 1-hour high-energy ball-milling. Experimental data (black dots), calculated intensity (red line), forsterite (ocher line), enstatite (blue line), clinochlore (cyan line) and anatase TiO_2 (light green line) are reported. The difference between experimental and calculated data in linear scale and the stick pattern for all the phases, listed in descending order as above, are provided

Table 4.2.2: Phase weight percentage calculated by Rietveld Refinement from XRD data for the different olivine Titania anatase materials prepared via 1 hour of mechanical ball-milling.

bulk	***Wt % Anatase Nominal***	***Wt % Forsterite***	***Wt % Enstatite***	***Wt % Clinochlore***	***Wt % TiO_2 Anatase***	***R_{wp}***
Olivine	*0.5*	*90 ± 1*	*6 ± 1*	*3 ± 1*	*0.5 ± 0.1**	*10.3*
Olivine	*1*	*89 ± 1*	*7.9 ± 0.5*	*1.7 ± 0.2*	*1.0 ± 0.1*	*12.0*
Olivine	*1.5*	*89 ± 2*	*7.9 ± 0.4*	*1.6 ± 0.9*	*1.6 ± 0.5*	*10.5*
Olivine	*5*	*87 ± 1*	*6.4 ± 0.5*	*1.6 ± 0.2*	*4.6 ± 0.1*	*11.3*
Olivine	*10*	*81 ± 2*	*7.6 ± 0.6*	*1.6 ± 0.6*	*10.0 ± 0.2*	*17.9*
Olivine	*15*	*76 ± 1*	*7 ± 1*	*1.6 ± 0.3*	*16 ± 2*	*18.2*

**The weight percentage of TiO_2 anatase is reported even though 0.5 wt % is under the detection limit of the technique, because TiO_2 anatase was added in the ball-milled powders, and the total accuracy of the fit increases when performed by adding TiO_2 anatase.*

Table 4.2.3: Cell Parameters refined via application of Rietveld method on the experimental XRD pattern with the help of the program MAUD for olivine-titania samples prepared via mechanical ball-milling

Sample	Crystalline phase	Space Group	Cell parameters					
			a (Å)	b (Å)	c (Å)	α (°)	β (°)	γ (°)
Olivine	Forsterite	$Pbnm$	4.76(3)	10.22(4)	5.99(4)	-	-	-
	Enstatite ferroan	$Pbca$	18.24(7)	8.84(1)	5.19(4)	-	-	-
	Clinochlore	$P\bar{1}$	5.36(1)	9.20(6)	14.43(8)	90.4(6)	97.9(3)	89.7(7)
Olivine 0.5 wt % TiO_2	Forsterite	$Pbnm$	4.76(3)	10.22(3)	5.99(4)	-	-	-
	Enstatite ferroan	$Pbca$	18.24(8)	8.83(8)	5.19(3)	-	-	-
	Clinochlore	$P\bar{1}$	5.31(8)	9.26(1)	14.43(0)	90.4(2)	97.6(2)	90.3(3)
	Anatase TiO_2	$I4_1/a$	3.75(2)	-	9.5(2)	-	-	-
Olivine 1 wt % TiO_2	Forsterite	$Pbnm$	4.76(3)	10.22(2)	5.99(4)	-	-	-
	Enstatite ferroan	$Pbca$	18.25(0)	8.83(4)	5.18(4)	-	-	-
	Clinochlore	$P\bar{1}$	5.35(0)	9.17(6)	14.41(5)	90.5(6)	97.3(7)	89.7(7)
	Anatase TiO_2	$I4_1/a$	3.78(0)	-	9.51(0)	-	-	-
Olivine 1.5 wt % TiO_2	Forsterite	$Pbnm$	4.76(2)	10.22(2)	5.99(4)	-	-	-
	Enstatite ferroan	$Pbca$	18.24(0)	8.84(6)	5.19(1)	-	-	-
	Clinochlore	$P\bar{1}$	5.31(7)	9.26(3)	14.41(6)	90.3(1)	97.4(2)	90.2(5)
	Anatase TiO_2	$I4_1/a$	3.75(3)	-	9.50(0)	-	-	-
Olivine 5 wt % TiO_2	Forsterite	$Pbnm$	4.76(4)	10.22(6)	5.99(5)	-	-	-
	Enstatite ferroan	$Pbca$	18.25(5)	8.84(4)	5.20(2)	-	-	-
	Clinochlore	$P\bar{1}$	5.27(6)	9.33(9)	14.48(1)	91.0(2)	99.27(4)	88.9(7)
	Anatase TiO_2	$I4_1/a$	3.78(8)	-	9.51(6)	-	-	-
Olivine 10 wt % TiO_2	Forsterite	$Pbnm$	4.76(4)	10.22(6)	5.99(6)	-	-	-
	Enstatite ferroan	$Pbca$	18.24(9)	8.84(3)	5.19(0)	-	-	-
	Clinochlore	$P\bar{1}$	5.28(3)	9.25(5)	14.40(3)	90.9(2)	96.1(6)	90.9(6)
	Anatase TiO_2	$I4_1/a$	3.78(9)	-	9.51(7)	-	-	-
Olivine 15 wt % TiO_2	Forsterite	$Pbnm$	4.76(6)	10.23(1)	5.99(7)	-	-	-
	Enstatite ferroan	$Pbca$	18.24(5)	8.84(7)	5.18(9)	-	-	-
	Clinochlore	$P\bar{1}$	5.29(7)	9.26(1)	14.44(3)	91.1(5)	97.3(9)	89.5(8)
	Anatase TiO_2	$I4_1/a$	3.78(9)	-	9.52(3)	-	-	-

SEM/EDS mapping, performed on the prepared sample powders, confirmed the uniform distribution of TiO_2 added during the ball-milling modification of the olivine (Figure 4.2.2).

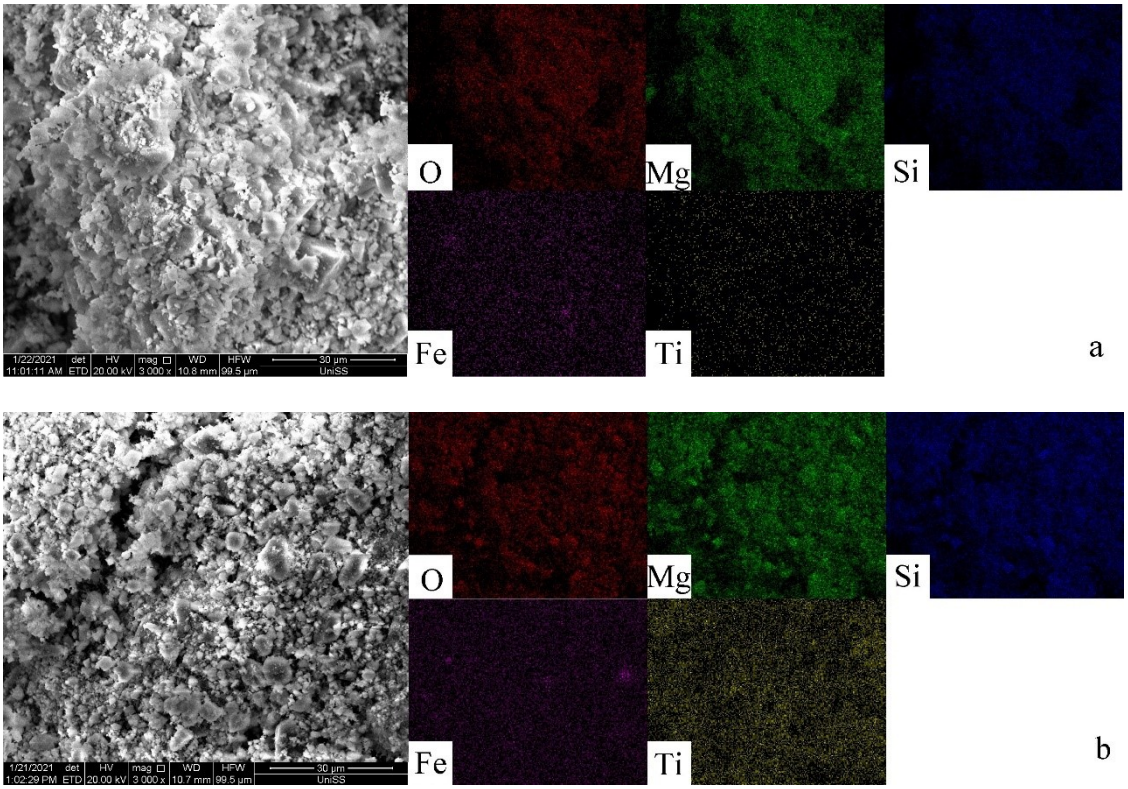

Figure 4.2.2: EDS mapping on olivine 1 wt % TiO_2 anatase 1hBM powders (a) and olivine 5 wt % TiO_2 anatase 1hBM powders (b)

Adsorbable CO_2 was quantified by pulse chemisorption analysis with the same condition reported in Paragraph 4.1 for pristine olivine (Table 4.2.4). The TiO_2 addition does not seem to significantly affect the samples capacity to adsorb CO_2. The slightly decrease in CO_2 adsorption capacity observed for the modified samples, compared to pristine olivine, is attributable to the lower olivine weight percentage in the modified samples because while olivine has a quite strong interaction with the gaseous CO_2, TiO_2 has not. Adsorbable CO_2 quantity is still very close for all prepared samples.

Table 4.2.4: Adsorbed CO_2 calculated via pulse chemisorption experiments on olivine and modified olivine powders

Sample	CO_2 adsorbed (µmol/g $_{sample}$)
Olivine	4.3(2)
Olivine 0.5 wt TiO_2 1hBM	3.7(2)
Olivine 1 wt TiO_2 1hBM	4.2(1)
Olivine 1.5 wt TiO_2 1hBM	3.9(1)
Olivine 5 wt TiO_2 1hBM	4.0(1)
Olivine 10 wt TiO_2 1hBM	3.8(2)
Olivine 15 wt TiO_2 1hBM	3.5(4)

Further olivine-based compounds were obtained by wet impregnation of mineral olivine with Ti-isopropoxide ($Ti\{OCH(CH_3)_2\}_4$), and with $Ni(NO_3)_2 \cdot 6H_2O$ as precursors of Ti and NiO dopants, respectively.

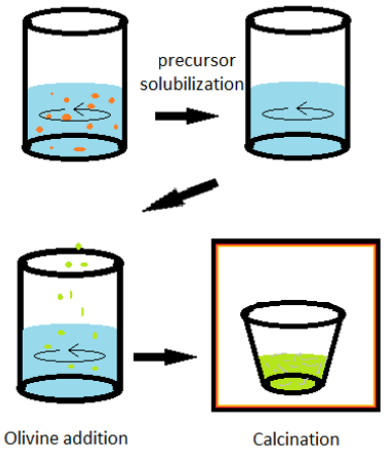

Figure 4.2.3: olivine impregnation route, schematical representation

Ti-isopropoxide was dissolved in 95/5 Ethanol/water solution, after solubilization proper amount of olivine powders were added to the solution under stirring. The powders after drying were calcinated for 5 hours at 600 °C to eliminate the organic component and obtain the desired titanium oxide-doped olivine (Figure 4.2.3). NiO-

doped olivine was obtained by adopting the same experimental procedure but dissolving the precursor nickel nitrate in distilled water and calcinating the powders for 3 hours at 500 °C.

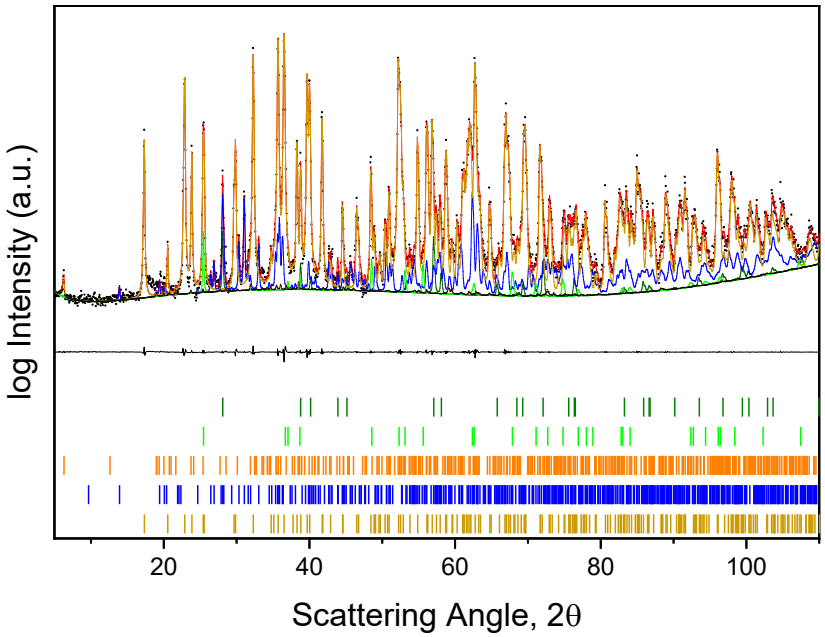

Figure 4.2.4: XRD pattern and Rietveld refinement for olivine-impregnated 1 wt % TiO_2. Experimental data (black dots), calculated intensity (red line), forsterite (ocher line), enstatite (blue line), vermiculite (orange line), TiO_2 anatase (light green line) and TiO_2 rutile (dark green line) are reported. The difference between experimental and calculated data in linear scale and the stick pattern for all the phases, listed in ascending order, are provided

Olivine-impregnated materials have been characterized via XRD measurements (Figure 4.2.4 and 4.2.5) and microstructural features were evaluated by Rietveld refinement. In the TiO_2 impregnated sample, forsterite and enstatite ferroan phases are not strongly affected by the impregnation procedure: indeed, their abundance and cell parameters did not change significantly (Table 4.2.5). Two different TiO_2 phases were formed after impregnation procedure, anatase and rutile, which were observed in the experimental XRD pattern.

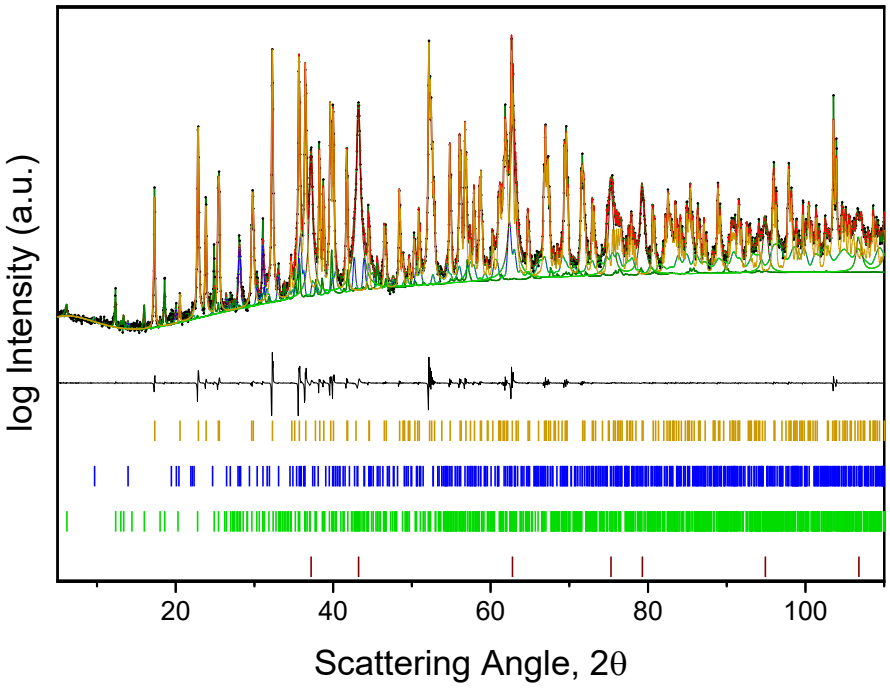

Figure 4.2.5: XRD pattern and Rietveld refinement for olivine impregnated 10 wt % NiO. Experimental data (black dots), calculated intensity (red line), forsterite (ocher line), enstatite (blue line), clinoclorite (green line) and NiO (dark red line) are reported. The difference between experimental and calculated data in linear scale and the stick pattern for all the phases, listed in descending order as above, are provided

Moreover, their total abundance matches the nominal Ti amount in the prepared samples. Clinochlore phase of pristine olivine is not observed after the impregnation procedure. A Vermiculite-like phase can be instead individuated as part of the prepared samples. This phyllosilicate can be formed from weathering processes on silicates of the chlorite group like clinochlore in natural condition [124,125]. The NiO-impregnated olivine sample is characterized by no significant changes in the cell parameters of forsterite and enstatite ferroan phases if compared to pristine olivine. The clinochlore phase is not observed in the prepared samples. Clinochlorite can be recognized from the experimental patterns. The weight fraction ratio between forsterite and enstatite

ferroan seems to be affected by the impregnation treatment, with an increase of the enstatite relative fraction. NiO oxide is formed after the impregnation treatment, only in cubic lattice. The weight percentage of NiO is coherent with the nominal weight percentage of Nickel precursor.

Table 4.2.5: Phase weight percentage and cell parameter calculated via Rietveld Refining on olivine impregnated samples XRD patterns, Rwp = 10.4 (TiO_2 impregnated sample, Rwp = 8.7 (NiO impregnated sample)

Sample	Crystalline phase	Wt %	Space Group	Cell parameters					
				a (Å)	b (Å)	c (Å)	α (°)	β (°)	γ (°)
Olivine 1 wt % TiO_2 impr.	Forsterite ($Fe_{0.2}Mg_{1.8}SiO_4$)	90 ± 1	*Pbnm*	4.76(4)	10.22(1)	5.98(3)	-	-	-
	Enstatite ferroan ($Fe_{0.3}Mg_{0.7}SiO_3$)	7.6 ± 0.5	*Pbca*	18.26(5)	8.83(7)	5.20(2)	-	-	-
	Vermiculite ($Al_{3.36}$ $Ca_{0.86}$ $Fe_{0.41}$ $H_{16.74}$ $Mg_{4.04}$ $O_{30.42}$ $Si_{5.53}$ $Ti_{0.08}$)	0.5 ± 0.1#	$C2/m$	5.5(2)	8.8(6)	14.1(5)	-	97.(7)	-
	Anatase (TiO_2)	0.5 ± 0.1*	$I4_1/a$	3.74(9)	-	9.7(0)	-	-	-
	Rutile (TiO_2)	0.6 ± 0.1*	$P4_2/m$	4.48(8)	-	2.71(2)	-	-	-
Olivine 10 wt % NiO impr.	Forsterite ($Fe_{0.2}Mg_{1.8}SiO_4$)	77 ± 2	*Pbnm*	4.76(4)	10.22(5)	5.99(3)	-	-	-
	Enstatite ferroan ($Fe_{0.3}Mg_{0.7}SiO_3$)	7.2 ± 0.6	*Pbca*	18.25(0)	8.84(7)	5.20(1)	-	-	-
	Clinochlorite ($Mg_5Al_2Si_3O_{18}H_8$)	3.6 ± 0.3	$C2/c$	3.37(6)	13.57(7)	28.6(2)	-	91.6(2)	-
	NiO	12.2 ± 0.9	$Fm\bar{3}m$	4.18(6)	-	-	-	-	-

**The weight percentage of TiO_2 anatase and TiO_2 rutile are reported even though 0.5-0.6 wt % are under the detection limit of the technique, because the total accuracy of the fit increases when performed with the two TiO_2 phases.*

#The weight percentage of vermiculite is reported even though 0.5 wt % is under the detection limit of the technique, because an isolated peak attributable to this phase is clearly visible in the experimental pattern.

Pulse chemisorption analysis held on TiO_2-impregnated olivine sample allowed for the determination of the adsorbable CO_2 quantity. The CO_2 adsorbed by the sample impregnated with 1 wt % of TiO_2 is 4.4 ± 0.5 μmol/g $_{sample}$, thus resulting comparable, within the experimental error, to the pristine olivine sample.

The influence of the impregnation method on the properties of the material also affects its pH in water solution. The pH, measured in water solution with dissolved impregnated TiO_2 olivine powders, is 9.7, higher than the one measured for pristine olivine (9.0).

4.3 Synthetic olivine

In order to overcome the problem arising from the consumption of the olivine material during CO_2 conversion processes, where it is a reagent, and to obtain a starting material with more suitable characteristics for catalysis, a synthetic route to artificially produce olivine was implemented. The synthesis was developed with the aim of increasing the surface area of the mineral olivine. In order to verify the viability of the method, pure Magnesium synthetic olivine was synthetized. The methodology developed by Hassanzadeh-Tabrizi et al. [126] has been applied to perform the synthesis of the new porous material.

Cetyltrimethlammonium bromide (CTAB) was selected as surfactant for the building of a mesoporous structured olivine. CTAB was solubilized in distilled water under magnetic stirring. The pH of the solution was adjusted to 12, by addition of aqueous NH_3 solution. TEOS and $Mg(NO_3)_2{\cdot}6H_2O$ were then added as precursors for silicate structure and Mg, respectively. After 12 hours under magnetic stirring, the solution was filtered, washed and then calcinated at 900 °C for 3 hours.

XRD analysis performed on the obtained powders highlighted the presence of two magnesium silicate phases, namely forsterite (Mg_2SiO_4) and enstatite ($MgSiO_3$), and the presence of a silicate-based amorphous phase. The two crystalline phases are the Mg-

only correspondent of the two most abundant phases we observe in the mineral olivine material (Table 4.1.1). Thus, the terminology synthetic olivine may be applied to the synthetized material. It may be also surmised that the amorphous phase is produced as a consequence of the presence of the templating agent that prevents the growth of crystalline phases.

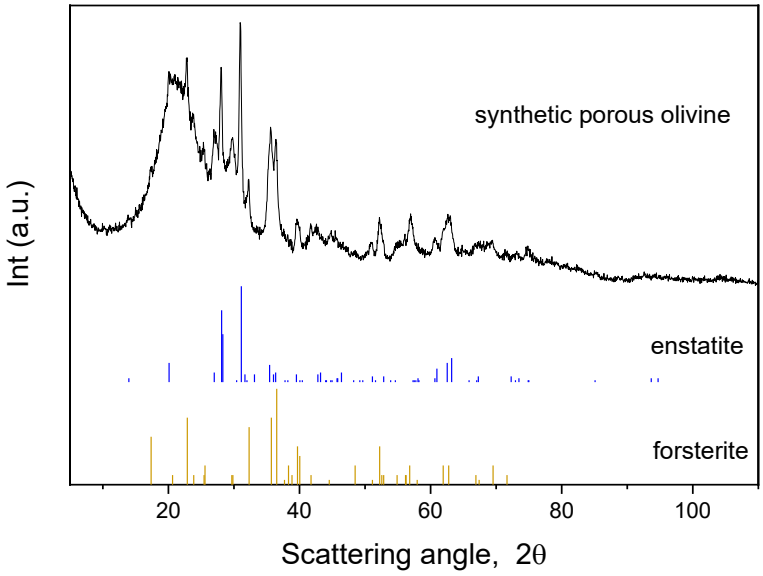

Figure 4.3.1: XRD pattern of synthetic olivine and stick patterns of forsterite and enstatite phases

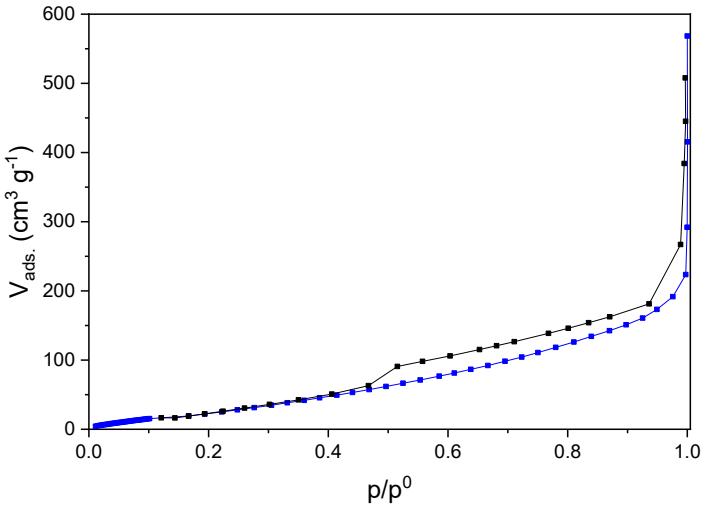

Figure 4.3.2: N_2 Physisorption analysis isotherm on synthetic olivine powders

N_2 physisorption analysis was conducted to evaluate the surface area of the synthetic olivine. The system is characterized by an isotherm, reported in Figure 4.3.2, classified as type II b, and the value of specific surface area, estimated according to B.E.T. method, is equal to 121 $m^2 g^{-1}$. While an increase in the surface area was observed with respect to mineral olivine (B.E.T. surface area 1.46 $m^2 g^{-1}$) the TEM analysis evidenced the collapse of the ordered porous system after the calcination process (Figure 4.3.3).

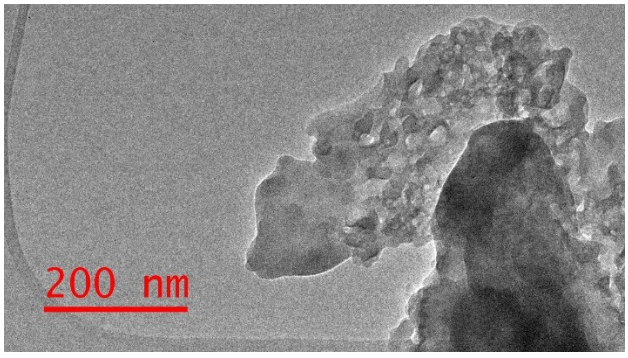

Figure 4.3.3: TEM image on synthetic olivine powders

4.4 Photochemical reactor

Photochemical tests were conducted in a photochemical reactor customized *ad hoc*, consisting of a cylindrical stainless-steel main body. Two screw stainless-steel hole caps allow for the insertion of the solid sample inside the reactor and allow for two quartz windows to be enclosed. The sealing between each quartz window and the stainless-steel body is granted by one rubber O-ring and mastic (Figure 4.4.1).

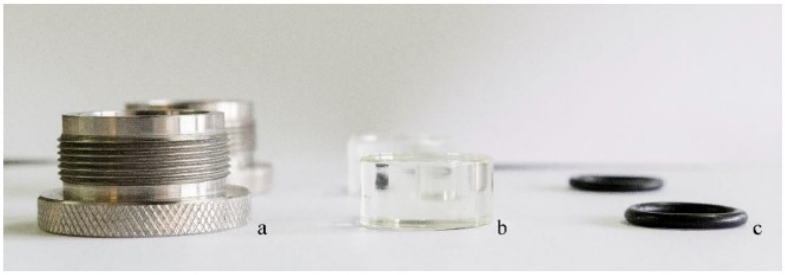

Figure 4.4.1: stainless-steel cup (a), quartz window (b) and sealing O-ring (c)

The cylindrical main body is provided with three inlet/outlet valves available for gas injection, gas flow inlet and outlet, gas sampling.

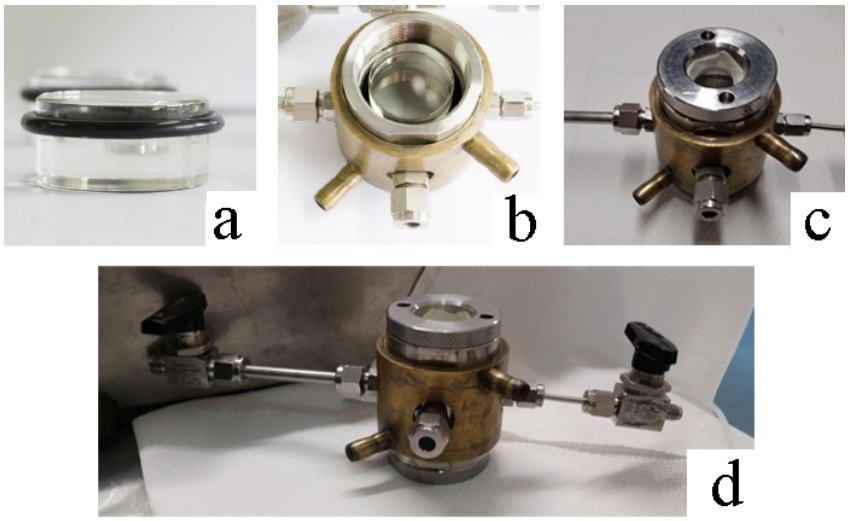

Figure 4.4.2: O-ring engulfing the quartz window (a), quartz window enclosure in the photochemical reactor (b), photochemical reactor (c), photochemical reactor in batch configuration (d)

The total internal volume of the reactor in the configuration used for batch experiment (Figure 4.4.2d) is around 12 cm^3.

The photochemical reactor offers various advantages like the user-friendly sample handling, the easy experimental set-up condition modification, the possibility of gas sampling during the analysis and temperature control via external cooling system.

4.5 Photochemical Conversion Tests: Ball-milled Samples

Pellets of 1.2 g of material were prepared with the titania modified olivine powders. For each pellet the powders were pressed for 30 minutes with 200 kg cm^{-2} of pressure with the aid of a hydraulic press (Figure 4.5.1).

Figure 4.5.1: sample pellet

Tests were performed in batch conditions for 12 hours irradiation with solar simulator. Each test was conducted inserting into the photochemical reactor one pellet, deposing 200 µL of water on top of the pellet (Figure 4.5.2). The tests were conducted with pure CO_2. The pellet was irradiated from the top with the solar simulator offering a surface exposed to the radiation of 133 mm^2.

Preliminary photochemical tests highlighted a temperature rise within the rector during solar irradiation, and the T value, experimentally measured by a thermocouple placed inside the reactor during any irradiation test, has been stabilized at 40 ± 2 °C. Therefore, the possible occurrence of a thermal effect in the activation of the system

was tested by heating to 40°C the photochemical reactor in a sand bath. The conversion of CO_2 was observed after 12 hours of heating, approaching the value of 10%, and no products arising from CO_2 reduction, *i.e.* light hydrocarbons evolution, were detected.

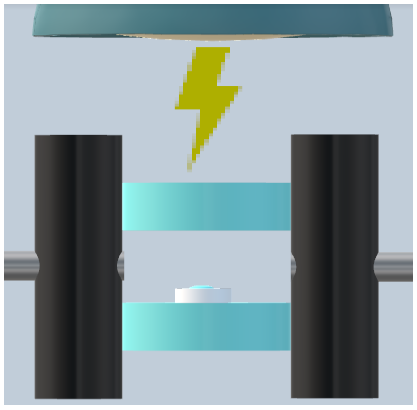

Figure 4.5.2: Photochemical test scheme

We then moved to the photochemical activation tests. In Figure 4.5.3 are reported the conversion percentages of CO_2 observed after 12 hours of irradiation, calculated as difference between the area of CO_2 standardized before the solar irradiation and the GC area after 12 hours of irradiation. Repeatability tests were conducted for each sample. Test were conducted with the same experimental condition on 1-hour ball-milled olivine in form of pellet, and β-TiO_2 in form of pellet. No appreciable conversion of CO_2 was observed irradiating the pellet of pure anatase. After 12 hours of solar irradiation a conversion above 40 % was observed with the pellet of olivine without titania. The conversion of CO_2 increases with the increasing of titania percentage, reaching values above 50% of conversion. GC analysis highlighted the transformation of CO_2 into light hydrocarbons. Methane, ethene and ethane were detected. Methane evolution reaches a value above 200 ppm after 12 hours of irradiation on the sample with 15 wt % of titania. The maximum amount of ethane (65 ppm) and ethene (110 ppm) were observed with the same amount of titania added. Methane is the predominant hydrocarbon produced by the photochemical reaction on the CO_2. Selectivity to ethane and ethene increase with the increase of titania percentage in the

tested samples (Figure 4.5.4). Hydrogen was detected as secondary product in all tests performed and was evaluated via GC analysis always below 5 % v/v.

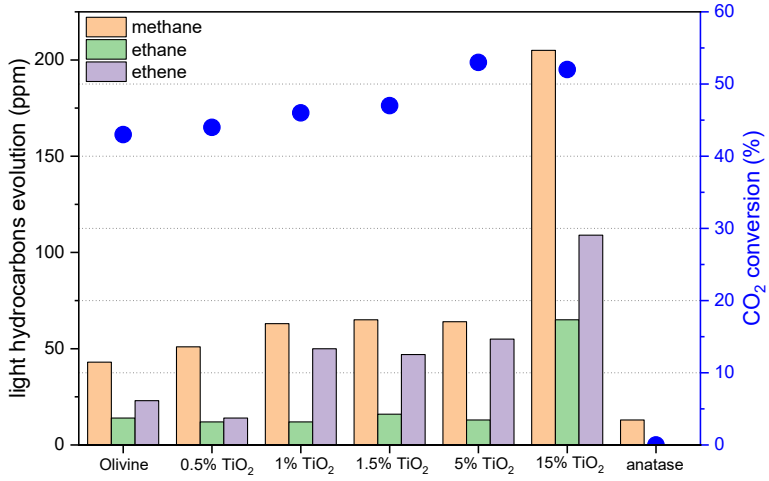

Figure 4.5.3: CO_2 conversion (blue dots) and light hydrocarbons evolution (histograms) on olivine titania modified ball-milled samples after 12 hours of solar irradiation

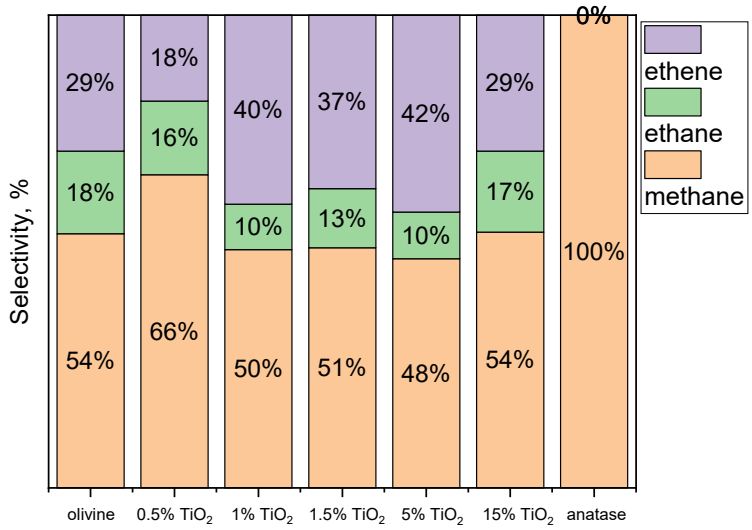

Figure 4.5.4: Light hydrocarbons selectivity on ball-milled titania olivine modified samples after 12 hours of solar irradiation, selectivity calculated as percentage of light hydrocarbon detected considering 100 % the total amount (in ppm) of the hydrocarbon detected with GC analysis

The photochemical tests confirmed the potential of modified olivine material for providing photochemically activated CO_2 conversion. The quantity of hydrocarbons produced does not justify completely the CO_2 conversion that has been observed. The presence of other conversion products and the adsorption of CO_2 in the solid material are the root causes to this discrepancy. In order to identify other conversion products, the tested pellets have been further characterized via XRD, SEM/EDS and FTIR analysis. The XRD analysis held on the tested pellet highlighted the formation of CO_2 conversion products only for the sample with 15 wt % of TiO_2 (Figure 4.5.5). In this sample $MgCO_3 \cdot 3H_2O$ (nesquehonite) was observed, but the weight percentage is still low (0.7 wt %) (Table 4.5.1). The cell parameters determined from Rietveld Refinement performed on the obtained pattern are reported in Table 4.6.2. No significant changes were observed concerning the cell parameters and the relative phase weight percentage calculated for the olivine phases (forsterite, enstatite and clinochlore). $MgCO_3 \cdot 3H_2O$ has been identified but the grow of crystals is not uniform, affecting the possible quantitative identification. A bulk technique like XRD fail to identify metal carbonate formation on the tested pellet with low amount of TiO_2 added where a lower CO_2 conversion was observed.

FTIR analysis held on the moist pellet after the analysis were not able to identify any liquid CO_2 conversion products as only signal attributable to water could be observed (Figure 4.5.6a). The ATR-FTIR analysis on the dried pellet did not show any signal due to lack of proper experimental conditions (lack of proper contact between the pellet surface and the ATR crystal (Figure 4.5.6b). The FTIR analysis on the powders after the pellet being ground was only able to identify the Si-O signal of olivine but the large dilution (1.2 g of olivine for very small amounts of nesquehonite on the pellet surface) has most certainly hampered the observation of any signal attributable to carbonates.

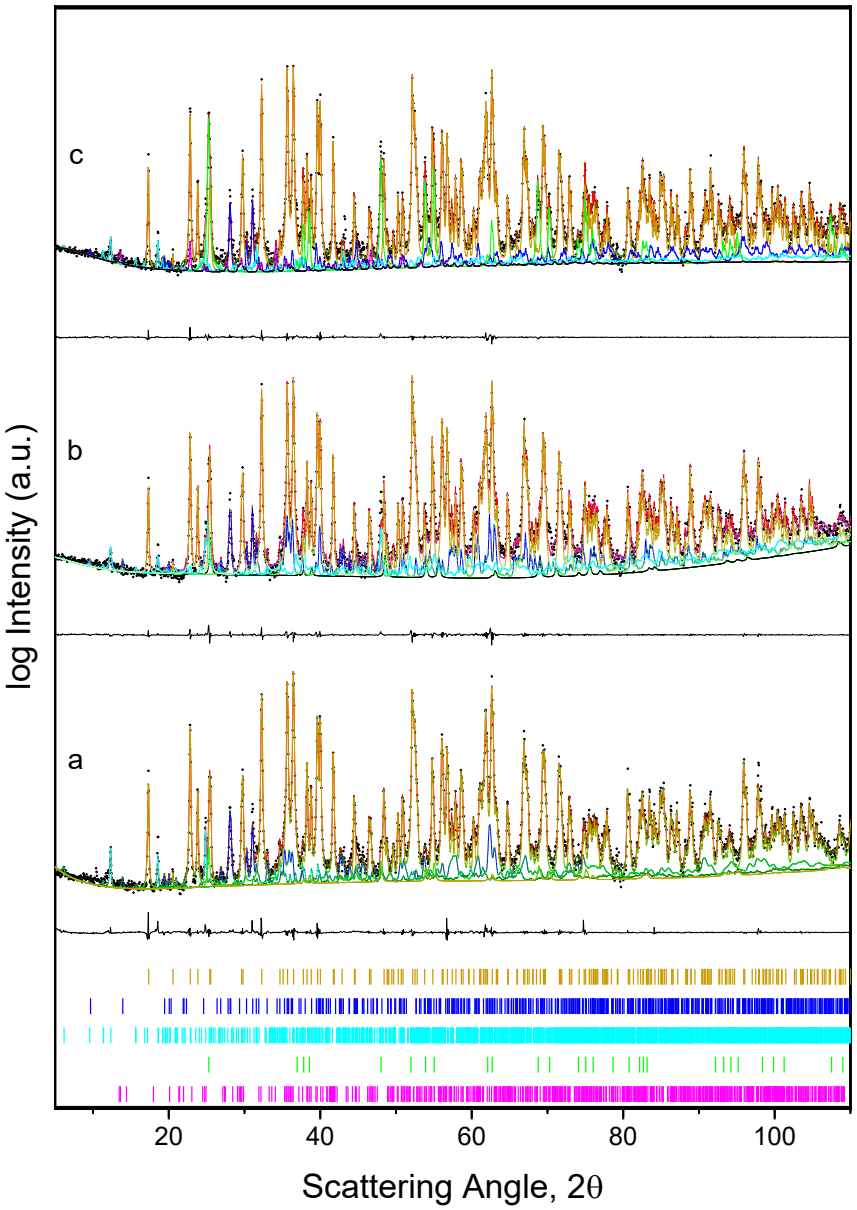

Figure 4.5.5: XRD pattern of pellets after 12 hours batch irradiation tests on (a) olivine 1 wt % anatase TiO_2, (b) olivine 5 wt % anatase TiO_2, (c) olivine 15 wt % anatase TiO_2. Experimental data (black dots), calculated intensity (red line), forsterite (ocher line), enstatite (blue line), clinochlore (cyan line), TiO_2 anatase (light green line) and nesquehonite (magenta line) are reported. The difference between experimental and calculated data in linear scale and the stick pattern for all the phases, listed in descending order as above, are provided

Table 4.5.1: Phase weight percentage and Rwp parameter calculated with Rietveld refinement from experimental XRD analysis held on ball-milled titania olivine modified pellets

bulk	***Wt % Anatase Nominal***	***Wt % Forsterite***	***Wt % Enstatite***	***Wt % Clinochlore***	***Wt % TiO_2 Anatase***	***Wt % Nesquehonite***	***R_{wp}***
Olivine	*1*	*89 ± 2*	*8 ± 1*	*1.7 ± 0.6*	*0.9 ± 0.2*	*-*	*12.2*
Olivine	*5*	*85 ± 2*	*7 ± 1*	*2.9 ± 0.8*	*5.5 ± 0.2*	*-*	*12.3*
Olivine	*15*	*78 ± 2*	*5.4 ± 0.6*	*2.2 ± 0.2*	*14 ± 1*	*0.7 ± 0.4*	*9.7*

Table 4.5.2: Cell Parameters refined via application of Rietveld method on the experimental XRD pattern with the help of the software MAUD for olivine titania pellet after 12 hours solar irradiation test in batch condition with pure CO_2

Sample	Crystalline phase	Space Group	Cell parameters					
			a (Å)	b (Å)	c (Å)	α (°)	β (°)	γ (°)
Olivine 1 wt % TiO_2	Forsterite	$Pbnm$	4.76(5)	10.22(8)	5.99(7)	-	-	-
	Enstatite ferroan	$Pbca$	18.26(5)	8.84(5)	5.20(2)	-	-	-
	Clinochlore	$P\bar{1}$	5.31(3)	9.26(8)	14.44(8)	90.3(8)	97.6(2)	89.9(9)
	Anatase TiO_2	$I4_1/a$	3.78(7)	-	9.5(0)	-	-	-
Olivine 5 wt % TiO_2	Forsterite	$Pbnm$	4.76(5)	10.22(7)	5.99(6)	-	-	-
	Enstatite ferroan	$Pbca$	18.26(5)	8.85(1)	5.19(4)	-	-	-
	Clinochlore	$P\bar{1}$	5.31(9)	9.2(9)	14.4(3)	90.(6)	97.(3)	88.(9)
	Anatase TiO_2	$I4_1/a$	3.74(7)	-	9.5(2)	-	-	-
Olivine 15 wt % TiO_2	Forsterite	$Pbnm$	4.76(3)	10.22(5)	5.99(5)	-	-	-
	Enstatite ferroan	$Pbca$	18.24(1)	8.84(6)	5.20(8)	-	-	-
	Clinochlore	$P\bar{1}$	5.33(7)	9.24(1)	14.42(0)	91.1(5)	97.3(9)	89.5(8)
	Anatase TiO_2	$I4_1/a$	3.78(7)	-	9.51(7)	-	-	-
	Nesquehonite	$P2_1/c$	7.71	5.36	12.11	-	90.08	-

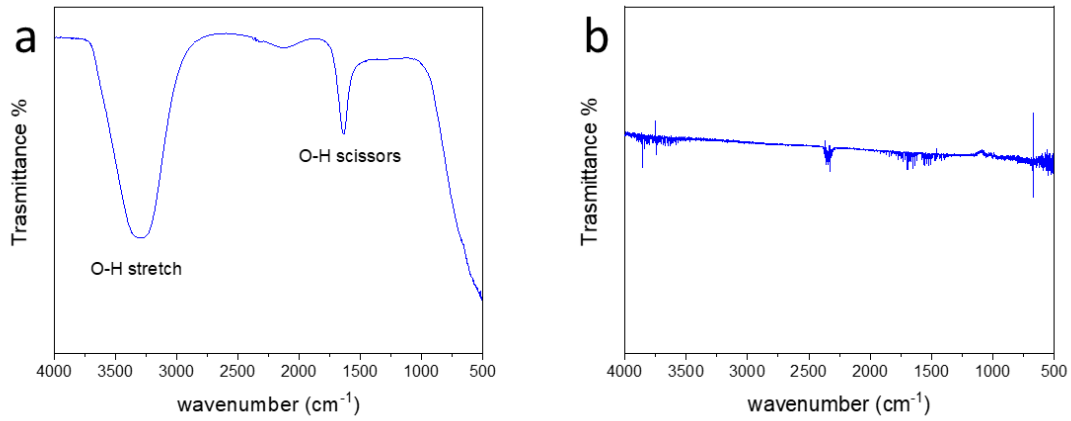

Figure 4.5.6: FTIR on moist pellet of olivine 1.5 wt % TiO_2 after 12 hours solar irradiation test, only signals attributable to water can be observed (a) and FTIR on dried pellet of olivine 1 wt % TiO_2 after 12 hours solar irradiation test (b)

SEM/EDS analysis on the pellet surface after irradiation test have instead allowed for the identification of the nesquehonite crystals derived from the converted CO_2 (Figure 4.5.7). The nesquehonite crystals can be recognized by their shape from literature confrontation and via EDS elemental mapping [127,128]. Only few nesquehonite crystals scattered on the pellet surfaces were observed but their presence is attested also in the 1 wt % TiO_2 pellet where XRD analysis was not able to identify them.

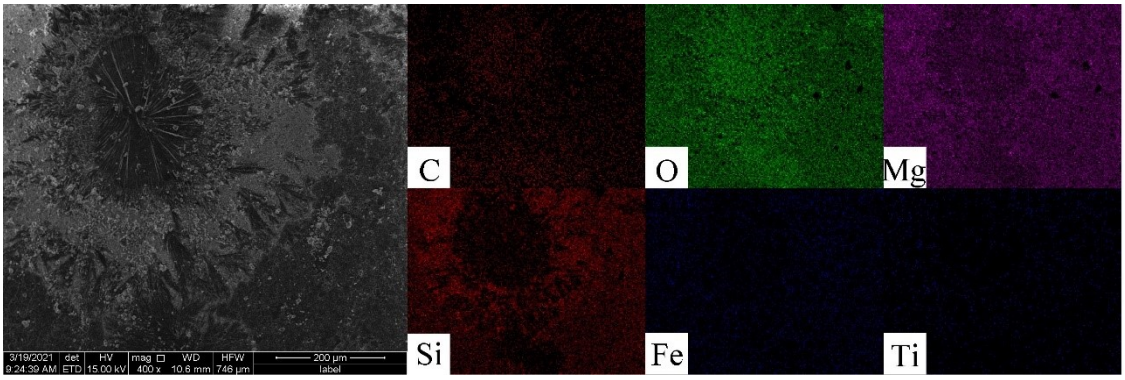

Figure 4.5.7: SEM image and EDS mapping were the $MgCO_3 \cdot 3H_2O$ is characterized by the C, O and Mg higher concentration and Si and Fe lower concentration on olivine 1 wt % TiO_2 pellet after 12 hours solar irradiation test

Along with light hydrocarbons and metal carbonates, the observed CO_2 conversion can be explained considering that GC analysis does evaluate the CO_2 decrease in gas phase. CO_2 conversion can be partially attributed to adsorption on the pellet surface: for instance, CO_2 adsorption on magnesium-rich minerals has indeed been proved very effective in trapping gaseous CO_2 in between grain boundaries [129].

It can then be surmised that, although a thermally activated process seems to be present, the rise of CO_2 conversion indicated by the experimental findings suggests the occurrence of an effective photochemical activation of the process. The photochemical route leads to a different products distribution, supporting the hypotesis of two distinct reaction pathways all leading to the CO_2 consumption. One involving the reduction of CO_2 to light hydrocarbons (photochemical route) and one involving an acid base reaction leading to the formation of metal carbonates on the pellet surface (both the activation routes seem to be effective in this process).

Moreover, the resuts shown above seem to suggest that the reaction paths start from the CO_2 dissolution in water. The basic pH given by olivine in water solution promote the dissolution of CO_2 and the formation of HCO_3^- and CO_3^{2-} ions in solution. The occurrence of carbonates in H_2O appears then a key step able to influence the subsequent the CO_2 reaction path.

4.6 Photochemical Conversion Tests: Impregnated Samples

The test performed on mechanical ball-milled modified olivine sample highlighted the possibility of CO_2 conversion on olivine-based materials with photochemical activation. In order to achieve information on both the efficiency of the photoconversion process and the kinetics of the conversion, the photochemical tests on impregnated samples were carried out in batch condition, while following the gas conversion change *vs.* the irradiation time. Different tests were conducted using the photochemical reactor (Figure 4.4.2d), each with 200 µL of water and 99.99% v/v CO_2 atmosphere and 1 pellet

of 1.2 g of the tested material. CO_2 conversion, followed via GC analysis as previously described, highlighted the early start of the conversion process after only 1 hour of solar irradiation (Figure 4.6.1). The conversion after that stint of solar irradiation is quite low (below 5%) but steadily increased with the irradiation time. After 12 hours of irradiation, the conversion reaches fairly appreciable values of conversion, around 70%. The conversion increased with the increase of irradiation time and the kinetics of conversion seems to have a linear behaviour. The conversion achieved by the impregnated sample after 12 hours of solar irradiation is higher than what observed for the mechanical ball-milled sample with equivalent TiO_2 amount (on identical experimental condition it converted less than 50%).

GC analysis highlighted no light hydrocarbons evolution associated with the CO_2 conversion.

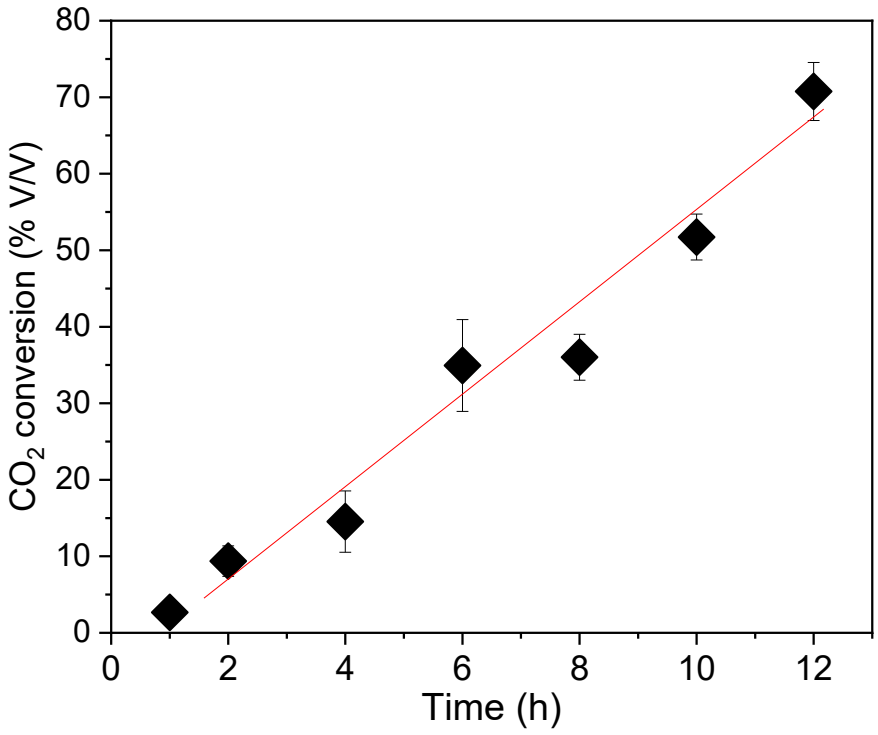

Figure 4.6.1: CO_2 conversion vs irradiation time on different batch test, each repetitively conducted on pellets of olivine impregnated 1 wt % TiO_2 with 200 µL of water and atmosphere of pure CO_2

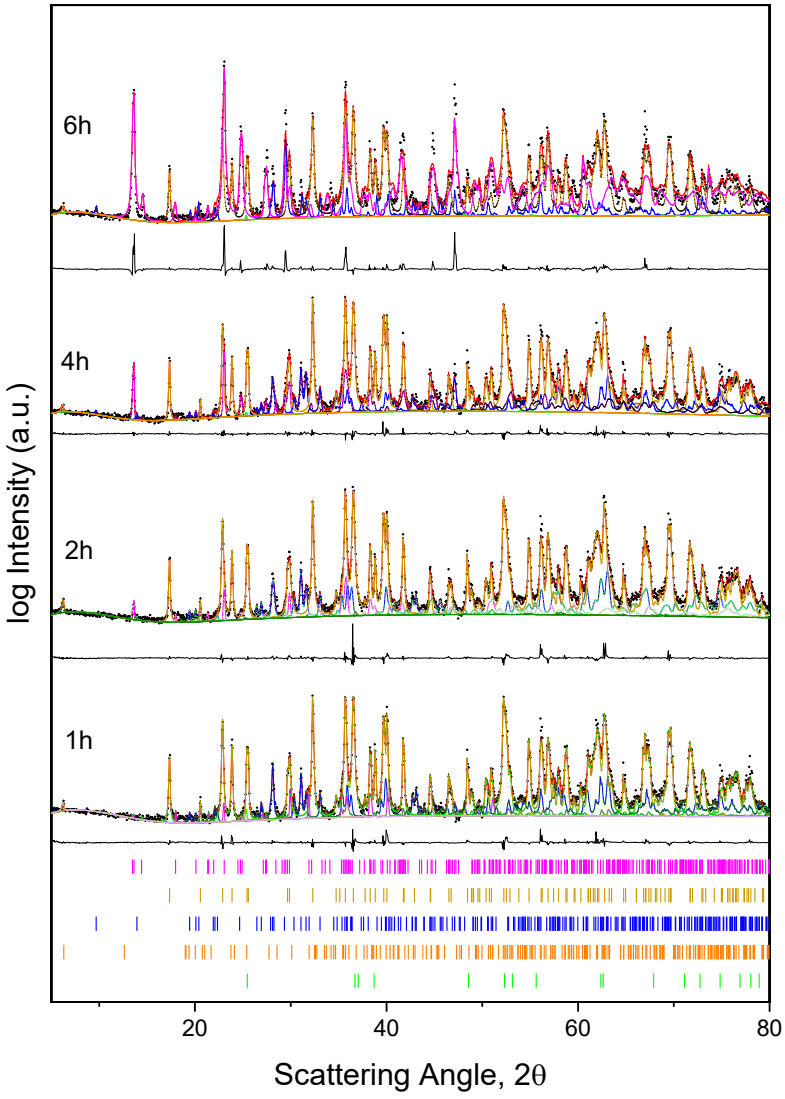

Figure 4.6.2: XRD pattern and Rietveld refinement on olivine impregnated 1 wt % TiO_2 pellet after solar irradiation test for 1h, 2h, 4h and 6h. Experimental data (black dots), calculated intensity (red line), nesquehonite (magenta line), forsterite (ocher line), enstatite (blue line), vermiculite (orange line) and TiO_2 anatase (light green line) are reported. The difference between experimental and calculated data in linear scale and the stick pattern for all the phases, listed in descending order as above, are provided

Table 4.6.1: Phase weight percentage calculated by Rietveld Refinement from XRD data for the different olivine 1 wt % impregnated Titania pellets after irradiation tests

Irradiation time	***Wt % Nesquehonite***	***Wt % Forsterite***	***Wt % Enstatite***	***Wt % Vermiculite***	***Wt % TiO_2 Anatase***	***R_{wp}***
0h	*-*	*90 ± 1*	*7.6 ± 0.5*	*0.5 ± 0.1*	*0.5 ± 0.1*	*10.4*
1h	*4 ± 1*	*87 ± 1*	*9 ± 1*	*0.15 ± 0.04*	*0.13 ± 0.06*	*13.9*
2h	*6 ± 1*	*86 ± 2*	*7.3 ± 0.9*	*0.28 ± 0.05*	*0.05 ± 0.02*	*13.2*
4h	*13 ± 1*	*79 ± 1*	*8 ± 1*	*0.13 ± 0.04*	*0.04 ± 0.3*	*12.0*
6h	*40 ± 2*	*53 ± 3*	*6 ± 1*	*0.10 ± 0.05*	*1.4 ± 0.6*	*21.8*

Table 4.6.2: Cell Parameters refined via application of Rietveld method on the experimental XRD pattern with the help of the program MAUD for impregnated olivine titania pellets after irradiation tests

Irradiation time	Crystalline phase	Space Group	Cell parameters					
			a (Å)	b (Å)	c (Å)	α (°)	β (°)	γ (°)
1h	Forsterite	$Pbnm$	4.76(3)	10.21(8)	5.98(1)	-	-	-
	Enstatite ferroan	$Pbca$	18.25(4)	8.82(7)	5.19(9)	-	-	-
	Vermiculite	$C2/m$	4.7(0)	8.5(7)	29.2(6)	-	106.(1)	-
	Anatase TiO_2	$I4_1/a$	3.78(0)	-	9.5(1)	-	-	-
	Nesquehonite	$P2_1/c$	7.72(8)	5.38(4)	12.23(5)	-	90.8(7)	-
2h	Forsterite	$Pbnm$	4.76(4)	10.22(1)	5.98(4)	-	-	-
	Enstatite ferroan	$Pbca$	18.26(2)	8.84(7)	5.19(4)	-	-	-
	Vermiculite	$C2/m$	5.5(3)	9.4(6)	28.5(9)	-	98.(6)	-
	Anatase TiO_2	$I4_1/a$	3.78(0)	-	9.5(1)	-	-	-
	Nesquehonite	$P2_1/c$	7.71(3)	5.38(2)	12.3(0)	-	90.7(7)	-

Irradiation time	Crystalline phase	Space Group	Cell parameters					
			a (Å)	b (Å)	c (Å)	α (°)	β (°)	γ (°)
4h	Forsterite	$Pbnm$	4.76	10.21	5.98	-	-	-
	Enstatite ferroan	$Pbca$	18.26	8.83	5.20	-	-	-
	Vermiculite	$C2/m$	4.91	8.52	28.67	-	97.93	-
	Anatase TiO_2	$I4_1/a$	3.78	-	9.51	-	-	-
	Nesquehonite	$P2_1/c$	7.71	5.40	12.24	-	90.54	-
6h	Forsterite	$Pbnm$	4.76(3)	10.22(2)	5.98(2)	-	-	-
	Enstatite ferroan	$Pbca$	18.1(8)	8.8(5)	5.2(0)	-	-	-
	Vermiculite	$C2/m$	5.5(0)	9.3(2)	28.3(3)	-	97.0(2)	-
	Anatase TiO_2	$I4_1/a$	3.7(8)	-	9.5(1)	-	-	-
	Nesquehonite	$P2_1/c$	7.71(3)	5.4(2)	12.12(9)	-	90.4(2)	-

The CO_2 was converted to $MgCO_3$, identified via XRD analysis and SEM/EDS mapping on the pellet after the photochemical tests. XRD analysis performed on the pellet after the photochemical test highlighted the formation of $MgCO_3 \cdot 3H_2O$ (nesquehonite). The uncontrolled growth of the carbonate crystals during the photoconversion test due to the static condition in which the process is held leads to preferential plane growths that limit the efficiency of the Rietveld refinement applied on the experimental pattern acquired. The non uniformity of the carbonate growth on the pellet surface also affects the accuracy of the total carbonate phase weight percentage evaluation. Even considering all of this we can clearly see the increase of carbonate phase percentage up to 6 hours of solar irradiation (Figure 4.6.2). Nesquehonite reaches indeed a weight percentage of 40% and emerges as the main phase on the pellet surface.

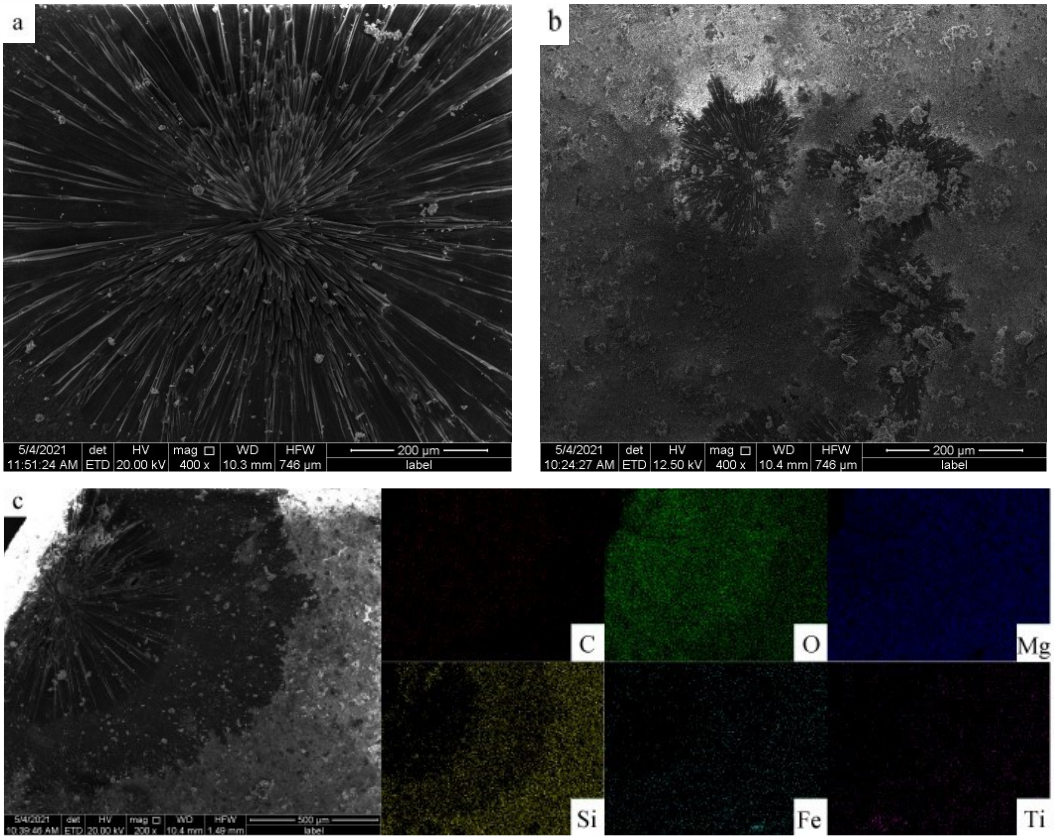

Figure 4.6.3: SEM images of $MgCO_3 \cdot 3H_2O$ of different size on the surface of the pellet of olivine Impregnated 1 wt % TiO_2 after 12 hours of solar irradiation (a,b) and EDS mapping were the $MgCO_3 \cdot 3H_2O$ is clearly characterized by the C, O and Mg higher concentration and Si and Fe lower concentration (c)

Nesquehonite crystal growth was observed with SEM paired with EDS. SEM images highlighted the presence of $MgCO_3$ crystals with a typical flower-like shape, ranging from a diameter size fo hundreds of nanometer to micrometers (Figure 4.6.3a and 4.6.3b). EDS analysis highlighted higher concentration of O paired with C and Mg and the absence of Si confirming that crystals are actually made of $MgCO_3$ (Figure 4.6.3c).

The uneven growth of nesquehonite crystals upon the surface of the pellet can be clearly seen in Figure 4.6.4. The dark dots on the SEM image are the metal carbonate on the pellet surface, recognizable by EDS mapping for the high C and O content. The

growth is randomized in the pellet surface, and it does not appear as if there is a correlation even with the presence of Ti in the pellet surface.

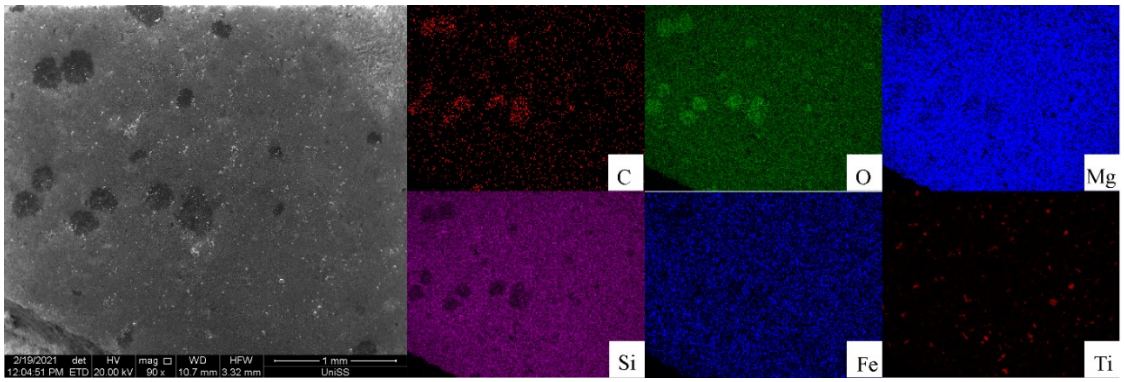

Figure 4.6.4: EDS mapping on SEM on a pellet of olivine impregnated 1 wt % TiO_2 after 12 hours of solar irradiation highlighting the non-homogeneous growth of $MgCO_3 \cdot 3H_2O$ crystals

The increase of the pH values in water solution that the impregnated sample gives if compared with the untreated olivine (from around 9.0 to around 9.7) strongly affects the CO_2 reaction path. The conversion of CO_2 on the TiO_2 impregnated samples indeed favours the fixation of the gas in the form of metal carbonates over the reduction of the CO_2 to light hydrocarbons. The process is more efficient in terms of CO_2 conversion and more selective to the products obtained as only metal carbonates were observed.

4.7 Conclusions

TiO_2-doped olivine has proved to be effective for activating the CO_2 conversion process towards light hydrocarbons and metal carbonates, in presence of H_2O and CO_2, via solar-driven photochemical activation. The effect of different doping methods has been evaluated: namely, the doping through mechanical ball-milling and the doping through impregnation with solvent.

GC analysis highlighted, after 12 hours of solar irradiation in batch conditions, values of conversion above 50% for the samples prepared via mechanical ball-milling and above 70% for the samples prepared via impregnation method, which are comparable, or even higher, respect to those observed in the literature for similar systems [130].

GC analysis allowed for the evaluation of the light hydrocarbons formed while XRD and SEM analysis enabled the identification of $MgCO_3 \cdot 3H_2O$ on the sample's pellet surfaces. The experimental tests support the hypothesis that two different reaction routes lead to these products.

The efficiency of conversion and the selectivity towards the conversion products has proven being influenced by factors like the TiO_2 weight percentage and modification of the pH of the H_2O solution.

5 RESULTS AND DISCUSSION: EAF STEEL SLAG

The experimental results of the photochemical activation of CO_2 conversion processes over olivine and olivine-doped systems prompted us to investigate the reactivity of further silicate-based compounds, which were obtained as industrial slags from iron and steel production processes, namely electric arc furnace steel slags. The study of the reactivity, towards CO_2 conversion processes, of such chemical systems appears to be of great relevance in view of a greener route for CO_2 conversion. Indeed, it aims also to the reutilization of waste materials, in CO_2 conversion processes activated via solar irradiation. In the following paragraph of the present chapter the experimental results of materials characterisation and photochemical CO_2 conversion tests over such steel slags are showcased.

5.1 Material Characterization

Electric arc furnace steel slag powders, which were produced by Acciaieria Arvedi Spa, have been structurally characterized via X-Ray Diffraction (XRD) and the experimental patterns were quantitatively evaluated by Rietveld refinement according to the procedure previously described. The XRD pattern of the pristine steel slag is reported in the trace a of Figure 5.1.1.

The steel slag powders are a complex system characterized by the presence of multiple crystalline phases, Ca_2SiO_4 (larnite), FeO (wurstite), Fe_3O_4 (magnetite), $Ca_2(Al,Fe)_2O_5$ (browmillerite) and smaller amount of quartz SiO_2. In Table 5.1.1 we reported the cell parameters calculated via Rietveld refinement and the weight percentage of each crystalline phase. Ca_2SiO_4 is the main phase (49.8 wt %) in the pristine steel slag. The amount of iron oxides in the sample is still quite high and contribute to the properties of the steel slag powders.

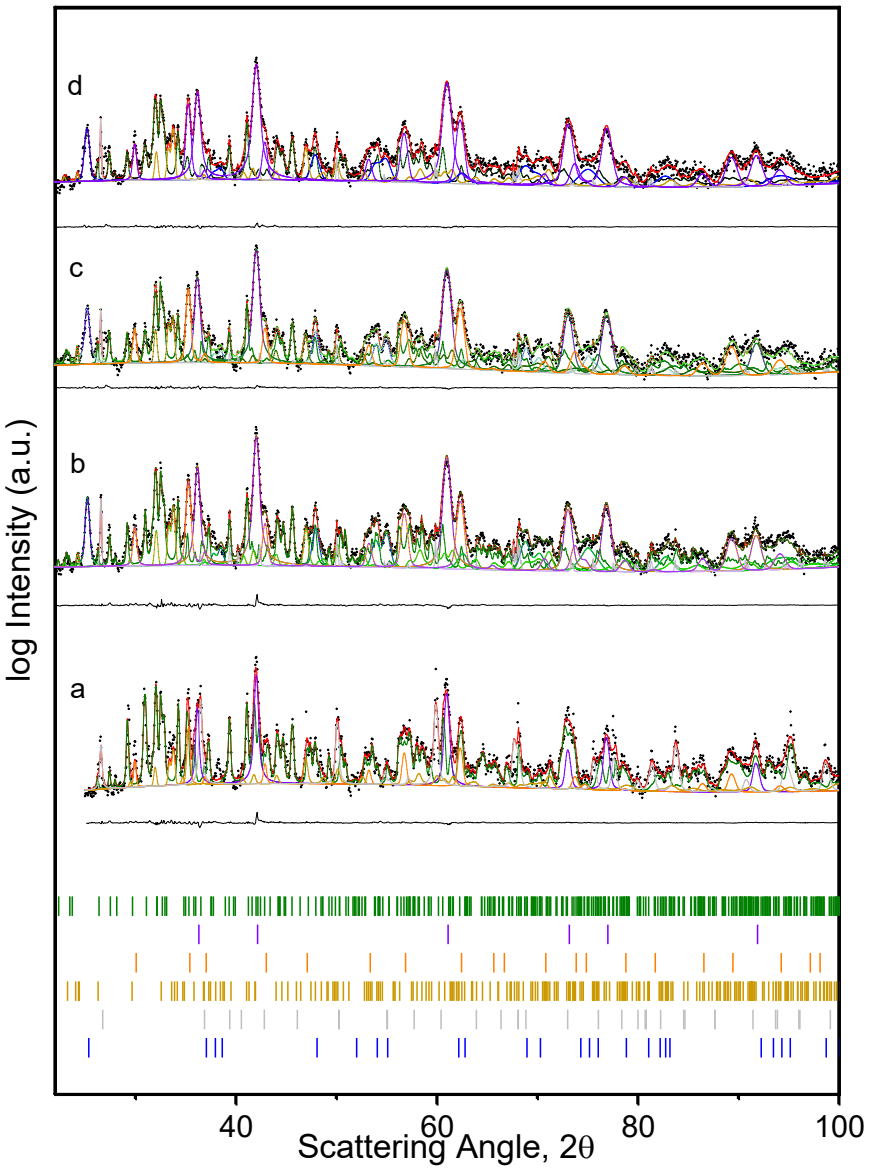

Figure 5.1.1: XRD pattern and Rietveld refinement on steel slag (a), steel slag 10 wt % TiO_2 1hBM powders (b), steel slag 10 wt % TiO_2 2hBM powders (c) and steel slag 10 wt % TiO_2 4hBM powders (d). Experimental data (black dots), calculated intensity (red line), larnite (green line), wurstite (violet line), magnetite (orange line), brownmillerite (ocher line), quartz (gray line) and anatase TiO_2 (blue line) are reported. The difference between experimental and calculated data in linear scale and the stick pattern for all the phases, listed in descending order as above, are provided

Table 5.1.1: Crystalline phase abundance in EAF steel slag as received and respective cell parameters calculated via Rietveld Refinement

Crystalline phase	Wt %	Space Group	Cell parameters					
			a (Å)	b (Å)	c (Å)	α (°)	β (°)	γ (°)
Larnite (Ca_2SiO_4)	50 ± 1	$P2_1/c$	5.51(3)	6.76(5)	9.31(6)	-	94.4(8)	-
Wurstite (FeO)	31 ± 1	$Fm\bar{3}m$	4.29(3)	-	-	-	-	-
Magnetite (Fe_3O_4)	7.9 ± 0.7	$Fm\bar{3}m$	8.41(9)	-	-	-	-	-
Brownmillerite ($Ca_2(Al,Fe)_2O_5$)	8.6 ± 0.8	$Pcmn$	5.57(0)	14.54(0)	5.35(4)	-	-	-
Quartz (SiO_2)	1.2 ± 0.1	$P3_221$	4.91(6)	-	5.40(7)	-	-	-

N_2 physisorption analysis conducted on pristine steel slag powders was performed to evaluate the specific surface area (Figure 5.1.2). Steel slag are a non-porous material characterized by a physisorption isotherm of type III. BET surface area was evaluated as 4.0 $m^2 \cdot g^{-1}$.

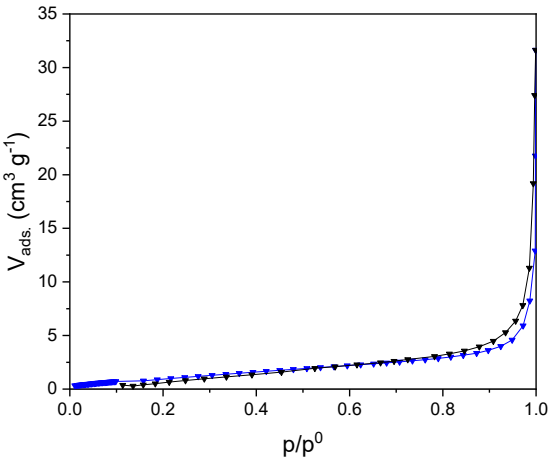

Figure 5.1.2: N_2 physisorption analysis isotherm on pristine steel slag

The energy band gap of the steel slag has been characterized by applying of the Kubelka-Munk theory on total reflectance UV-vis measurements (Figure 5.1.3). The

energy band gap of the pristine steel slag is 4.0 eV, corresponding to a wavelength of 310 nm. The minimum energy required to promote an electron to the lowest unoccupied orbital can be, then, provided by irradiating the sample with light having wavelength in the near-UV region of the solar spectrum.

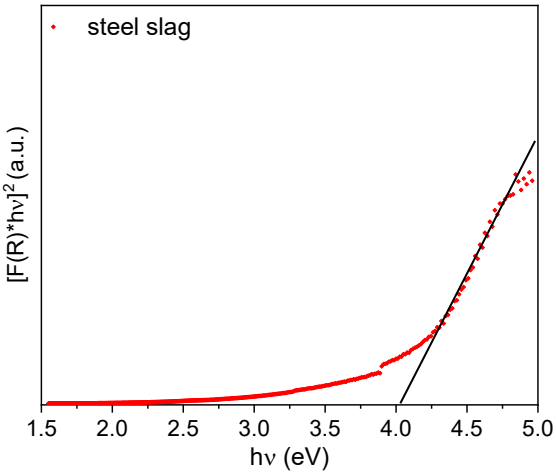

Figure 5.1.3: Energy band gap calculated via application of the Kubelka-Munk theory on total reflectance UV-vis measurements on steel slag powders

In order to extend the wavelength range that allows the activation of a photochemical process on the steel slag, the powders have been modified with different oxides and mixture of oxides (as reported in Table 5.1.2) selected for their narrow band gap, stability and effective response to solar radiation [131]. Therefore, steel slag powders have been treated by ball-milling for 1 hour, as specified in the following Table 5.1.2 with a total amount of 10 wt % of dopant materials and the energy band gap of the resulting powders has been checked according to the above cited procedure.

Table 5.1.2: Energy band gap calculated on the modified steel slag powder via application of the Kubelka-Munk theory on UV-vis measurements in solid state

Steel slag dopant	**Milling time**	**Energy Band Gap**
10 wt % TiO_2	1h	3.6(2) eV
10 wt % Fe_3O_4	1h	no significant change with respect to pristine steel slag
10 wt % Cu_2O	1h	no significant change with respect to pristine steel slag
5 wt % Cu_2O/5 wt % TiO_2	1h	2.97(2) eV
5 wt % Cu_2O/5 wt % Fe_3O_4	1h	no significant change with respect to pristine steel slag
5 wt % Cu_2O/5 wt % ZnO	1h	3.00(6) eV

As reported in the Table, a significant decrease in the band gap value was observed in the samples of several systems, indicating the success of the present approach to prepare composite systems potentially active in photochemical CO_2 conversion processes. In particular, the samples modified with the TiO_2 and with the mixed oxides Cu_2O/TiO_2 and Cu_2O/ZnO highlighted the most significant lowering of the energy band gap. While the experimental research on mixed oxides doped materials is still ongoing, the focus in the current thesis project was then set on the 10 wt % TiO_2 doped materials, which were selected by analogy with the systems prepared starting from the olivine.

Further specimens of steel slag - 10 wt % TiO_2 composite materials were then prepared by mechanically treating the powders for 1, 2 and 4 hours in the above cited conditions. As reported in Table 5.1.3, the extension of the mechanical treatment up to 4 hours did not further modify the band gap value. The structural characterisation by XRD of the TiO_2-modified steel slag systems ball milled for increasing times are reported in the upper traces of Figure 5.1.1.

Table 5.1.3: *Energy band gap calculated on the TiO_2 modified steel slag powders via application of the Kubelka-Munk theory on UV-vis measurements in solid state*

Steel slag dopant	**Milling time**	**Energy Band Gap**
10 wt % TiO_2	1h	3.6(2) eV
10 wt % TiO_2	2h	3.5(1) eV
10 wt % TiO_2	4h	3.6(2) eV

The experimental data and the evaluation of the microstructural parameters by Rietveld refinement, highlighted the peaks pertaining to the pristine steel slag powders, together with those accounting for the anatase polymorph of TiO_2, suggesting that no significant changes occurred in the phase composition as a result of the mechanical treatment: data are summarised in Table 5.1.4. Moreover, not significant changes in the cell parameters of the phases before and after the ball-milling treatment were observed, supporting the hypothesis that no relevant titanium insertion in the crystal structures of silicate (larnite, Ca_2SiO_4), and iron oxides (wurstite, FeO and magnetite, Fe_3O_4) occurred. The crystallite size of the most abundant phase (larnite) decreased with the increase of milling time from 899 Å (1hBM) to 546 Å (2hBM) and 418 Å (4hBM). The first milling hour is the most impactful on the size, no coalescence phenomena were observed up to 4 hours of ball-milling.

Table 5.1.4: Cell parameters and phase composition calculated via Rietveld refinement on XRD patterns for steel slag 10 wt % TiO_2 samples prepared via mechanical ball-milling;

Sample	Crystalline phase	Wt %	Space Group	Cell parameters					
				a (Å)	b (Å)	c (Å)	α (°)	β (°)	γ (°)
Steel slag 10 wt % TiO_2 1hBM Rwp = 10	Larnite (Ca_2SiO_4)	44 ± 1	*$P2_1/c$*	5.51(2)	6.76(4)	9.32(3)	-	94.50(7)	-
	Wurstite (FeO)	29 ± 1	$Fm\bar{3}m$	4.29(3)	-	-	-	-	-
	Magnetite (Fe_3O_4)	8.9 ± 0.4	$Fd\bar{3}m$	8.41(8)	-	-	-	-	-
	Brownmillerite ($Ca_2(Al,Fe)_2O_5$)	7.5 ± 0.5	*Pcmn*	5.56(8)	14.55(4)	5.36(2)	-	-	-
	Quartz (SiO_2)	3.4 ± 0.3	*$P3_221$*	4.91(6)	-	5.40(9)	-	-	-
	TiO_2 anatase	6.8 ± 0.3	*$I4_1/a$*	3.78(9)	-	9.50(2)	-	-	-
Steel slag 10 wt % TiO_2 2hBM Rwp = 10	Larnite (Ca_2SiO_4)	40 ± 1	*$P2_1/c$*	5.51(1)	6.76(2)	9.32(3)	-	94.5(1)	-
	Wurstite (FeO)	30 ± 1	$Fm\bar{3}m$	4.29(1)	-	-	-	-	-
	Magnetite (Fe_3O_4)	9.7 ± 0.5	$Fd\bar{3}m$	8.41(6)	-	-	-	-	-
	Brownmillerite ($Ca_2(Al,Fe)_2O_5$)	8.1 ± 0.7	*Pcmn*	5.57(3)	14.55(8)	5.36(4)	-	-	-
	Quartz (SiO_2)	2.5 ± 0.3	*$P3_221$*	4.91(4)	-	5.40(7)	-	-	-
	TiO_2 anatase	9.5 ± 0.6	*$I4_1/a$*	3.78(9)	-	9.48(6)	-	-	-
Steel slag 10 wt % TiO_2 4hBM Rwp = 11	Larnite (Ca_2SiO_4)	44 ± 1	*$P2_1/c$*	5.51(1)	6.76(5)	9.32(5)	-	94.5(1)	-
	Wurstite (FeO)	30 ± 1	$Fm\bar{3}m$	4.29(0)	-	-	-	-	-
	Magnetite (Fe_3O_4)	9.3 ± 0.7	$Fd\bar{3}m$	8.41(9)	-	-	-	-	-
	Brownmillerite ($Ca_2(Al,Fe)_2O_5$)	7.7 ± 0.7	*Pcmn*	5.55(9)	14.55(5)	5.36(9)	-	-	-
	Quartz (SiO_2)	2.7 ± 0.3	*$P3_221$*	4.91(6)	-	5.40(8)	-	-	-
	TiO_2 anatase	5.7 ± 0.4	*$I4_1/a$*	3.79(2)	-	9.5(0)	-	-	-

5.2 Photochemical Conversion tests

Steel slag powders have been tested under gas-flow conditions in presence of water under solar irradiation. Conversion tests were performed using the previously described photochemical reactor, reported in Figure 5.2.1, made by stainless steel, and equipped with quartz windows and inlet/outlet valves for gas flow and injection. The tests have been conducted irradiating one pellet of 2.0 g of material in presence of 200 µL of distilled water under continuous gas-flow injection conditions, and testing different values of gas flow, as specified in the followings. The pellets have been prepared by uniaxially pressing the powders for 25 minutes applying 100 Kg cm^{-2}. CO_2 conversion has been monitored via GC analysis with GC instrument featuring a TCD detector. The CO_2 percentage conversion has been calculated as the difference between the area of CO_2 measured for the flowing gas mixture standardized after equilibration before the irradiation test and the area of CO_2 measured during the irradiation test after each injection.

Figure 5.2.1: Photochemical reactor

Preliminary tests were performed to evaluate a possible thermic contribution to the CO_2 conversion on steel slags. As previously reported, these tests were carried out with one steel slag pellet and 10/90 CO_2/N_2 gas mixture, flowing through the reactor at a rate of 1 $ml \cdot min^{-1}$, and heating the photochemical reactor in a sand bath until setting

a temperature around 40 ± 5 °C, which is the temperature reached, inside the reactor, during solar irradiation tests, and experimentally measured by a thermocouple placed within the reactor. The gas cromatographoic analyses of the gas mixture eluited from the reactor indicated that a CO_2 decrease was induced by heating the reactants at 40 °C even in absence of solar irradiation. To this regard, the Figure 5.2.2 displays a comparison of the CO_2 conversion kinetics trends relevant to the processes activated by solar irradiation and by thermal treatment, over the steel slags system.

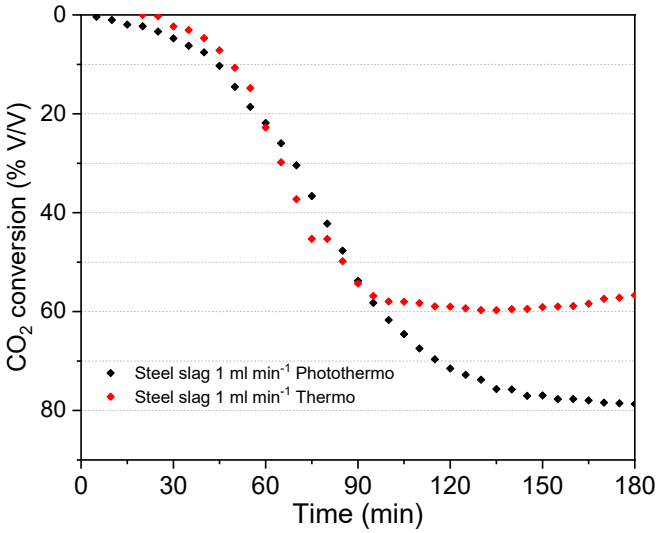

Figure 5.2.2: CO_2 conversion thermal activation (red dots) vs solar irradiation (black dots) on pellet of steel slag in presence of water and flow of 1 ml·min^{-1} of a gas mixture 10/90 CO_2/N_2

It emerges that both the two plotted curves display a sigmoidal shaped behaviour, and they overlap in the initial steps of the process. The conversion starts after the first few minutes of irradiation, but the CO_2 converted in the first 50 minutes is below 10%. After 50 minutes the conversion increases significantly and the conversion of the thermally activated sample approaches a steady value at about 55%, whereas the kinetics of the solar irradiated process indicates that CO_2 conversion still increases approaching the 80% by 150 minutes of treatment and keeping this value at least until 180 minutes of treatment. Such a sigmoidal trend suggests the presence of an initial induction step in

the CO_2 activation, and their overlapping seem to indicate that the thermic effect may be predominant in activating the CO_2 conversion, at least until 80-90 minutes of treatment, while the highest conversion values observed in the following step under solar irradiation, it seems to signify that a photochemical activation is prevalent during the latter part of the process.

Before analysing the structural evolution and possible mechanistic inferences related to the observed kinetic trends, we report in the followings the experimental data relevant to further CO_2 conversion kinetics. The subsequent runs were performed over the pellets of steel slag modified with 10 wt % of TiO_2 by 1 hour of mechanical treatment. A comparison of the kinetic trends relevant to the two solar irradiated samples, the steel slag itself and the one modified by the addition of TiO_2 is presented in Figure 5.2.3.

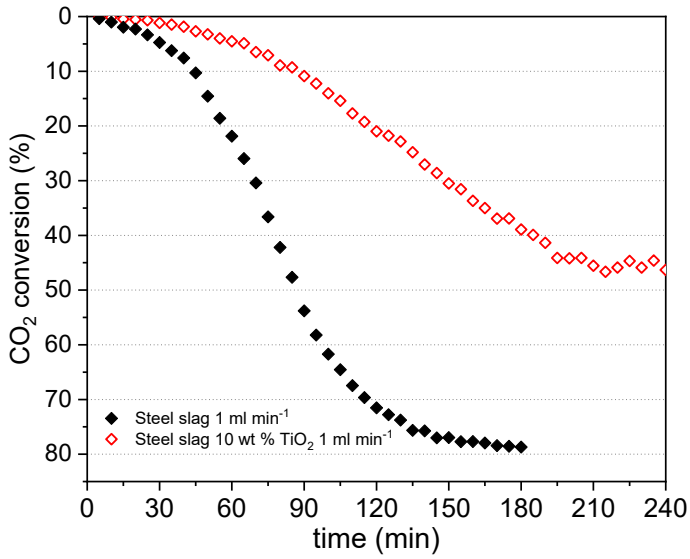

Figure 5.2.3: CO_2 conversion vs solar irradiation time under 1 ml·min^{-1} flow of a gas mixture 10/90 CO_2/N_2 for pristine steel slag (black dots) and for steel slag 10 wt % TiO_2 1hBM (empty red dots). CO_2 conversion has been calculated as difference between the GC area of CO_2 of the standardized gas mixture before the analysis and the GC area of CO_2 after each chromatographic injection

A similar trend characterises the two traces, but the modified steel slag sample appears to be less efficient, displaying lower conversion values and slower kinetics, approaching 50% of conversion after 240 minutes.

The increase in the feed of the gas mixture did not induce evident beneficial effects: the same behaviour was observed increasing the total gas flow from 1 ml·min^{-1} to 5 ml·min^{-1}, and a comparison of the kinetics relevant to the pristine and the modified steel slag systems under the two gas flow regimes, is shown in Figure 5.2.4.The CO_2 conversion trends have the same behaviour for the two systems, at the higher flow rate, but the latter reaches only a maximum of conversion around 30%. Considering that the amount of CO_2 entering the reactor and the sample is 5 times higher, the total amount of CO_2 converted is greater even if the process seems less efficient overall.

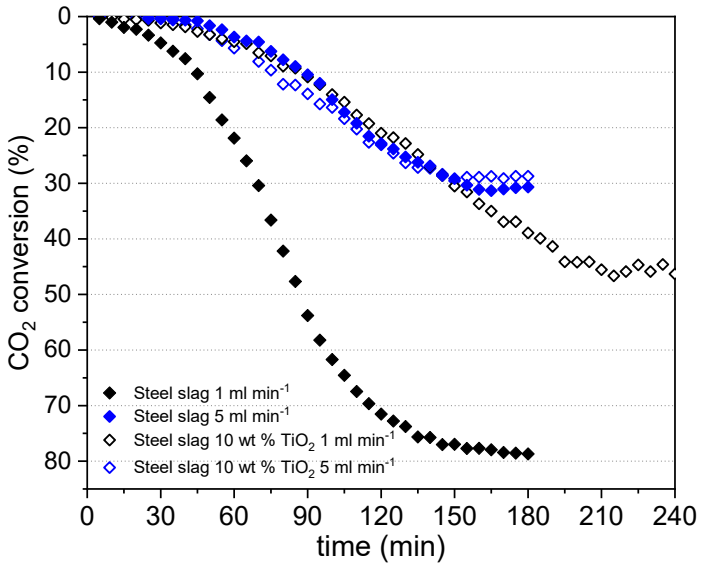

Figure 5.2.4: CO_2 conversion vs solar irradiation time for pristine steel slag under 1 ml·min^{-1} (black dots) and 5 ml·min^{-1} (blue dots) flow of a gas mixture 10/90 CO_2/N_2 and for steel slag 10 wt % TiO_2 1hBM under 1 ml·min^{-1} (empty black dots) and 5 ml·min^{-1} (empty blue dots) flow of a gas mixture 10/90 CO_2/N_2.

The gas-chromatographic analyses of the eluted gas did not reveal the formation of any other gaseous product arising from the chemical transformation of CO_2, whose concentration was strongly reduced in gas phase.

The XRD analysis and relevant microstructural data reported in the following Figures and Tables, revealed that, for both the systems, the main CO_2 conversion product was the $CaCO_3$. In particular, the analysis held on the pristine steel slag pellet after the irradiation tests, highlighted the formation of $CaCO_3$ in the calcite phase (Figure 5.2.5)., and its formation was matched by a decrease in the $CaSiO_4$ content in the sample, while the iron oxides were not consumed during the CO_2 conversion reaction (Table 5.2.1).

Table 5.2.1: *Cell parameters and phase composition calculated via Rietveld refinement on XRD patterns for steel slag pellet after irradiation test at 1 ml·min^{-1} and at 5 ml·min^{-1} gas flow and steel slag 10 wt % TiO_2 1hBM pellet after irradiation test at 5 ml·min^{-1} gas flow*

Sample	Crystalline phase	Wt %	Space Group	Cell parameters					
				a (Å)	b (Å)	c (Å)	α (°)	β (°)	γ (°)
Steel slag 1hBM After test 1 $ml \cdot min^{-1}$ Rwp = 15	Larnite (Ca_2SiO_4)	29 ± 1	$P2_1/c$	5.51(1)	6.78(4)	9.31(1)	-	94.4(5)	-
	Wurstite (FeO)	22 ± 1	$Fm\bar{3}m$	4.29(5)	-	-	-	-	-
	Magnetite (Fe_3O_4)	6.9 ± 0.8	$Fd\bar{3}m$	8.42(1)	-	-	-	-	-
	Brownmillerite ($Ca_2(Al,Fe)_2O_5$)	6.2 ± 0.8	*Pcmn*	5.55(6)	14.57(4)	5.36(7)	-	-	-
	Quartz (SiO_2)	3.2 ± 0.4	$P3_221$	4.91(7)	-	5.40(7)	-	-	-
	Calcite ($CaCO_3$)	31 ± 2	$R\bar{3}c$	4.99(1)	-	17.08(7)	-	-	-
Steel slag 1hBM After test 5 $ml \cdot min^{-1}$ Rwp = 15	Larnite (Ca_2SiO_4)	22 ± 2	$P2_1/c$	5.51(0)	6.78(3)	9.29(7)	-	94.4(7)	-
	Wurstite (FeO)	26 ± 2	$Fm\bar{3}m$	4.29(2)	-	-	-	-	-
	Magnetite (Fe_3O_4)	6.4 ± 0.8	$Fd\bar{3}m$	8.41(7)	-	-	-	-	-
	Brownmillerite ($Ca_2(Al,Fe)_2O_5$)	7 ± 1	*Pcmn*	5.55(5)	14.5(5)	5.35(5)	-	-	-
	Quartz (SiO_2)	5.5 ± 0.7	$P3_221$	4.91(7)	-	5.40(6)	-	-	-
	Calcite ($CaCO_3$)	33 ± 3	$R\bar{3}c$	4.99(1)	-	17.07(8)	-	-	-
Steel slag 10 wt % TiO_2 1hBM After test 5 $ml \cdot min^{-1}$ Rwp = 12	Larnite (Ca_2SiO_4)	16.7 ± 0.9	$P2_1/c$	5.51(3)	6.77(3)	9.24(2)	-	95.4(5)	-
	Wurstite (FeO)	24.7 ± 0.8	$Fm\bar{3}m$	4.29(2)	-	-	-	-	-
	Magnetite (Fe_3O_4)	6.8 ± 0.3	$Fd\bar{3}m$	8.42(0)	-	-	-	-	-
	Brownmillerite ($Ca_2(Al,Fe)_2O_5$)	11 ± 1	*Pcmn*	5.5(1)	14.7(3)	5.3(3)	-	-	-
	Quartz (SiO_2)	0.25 ± 0.04	$P3_221$	4.88(8)	-	5.4(4)	-	-	-
	TiO_2 anatase	5.8 ± 0.3	$I4_1/a$	3.79(0)	-	9.49(1)	-	-	-
	Calcite ($CaCO_3$)	28.8 ± 0.9	$R\bar{3}c$	4.99(1)	-	17.07(8)	-	-	-
	Aragonite ($CaCO_3$)	4.9 ± 0.6	*Pnma*	5.75(9)	4.98(3)	7.96(5)	-	-	-

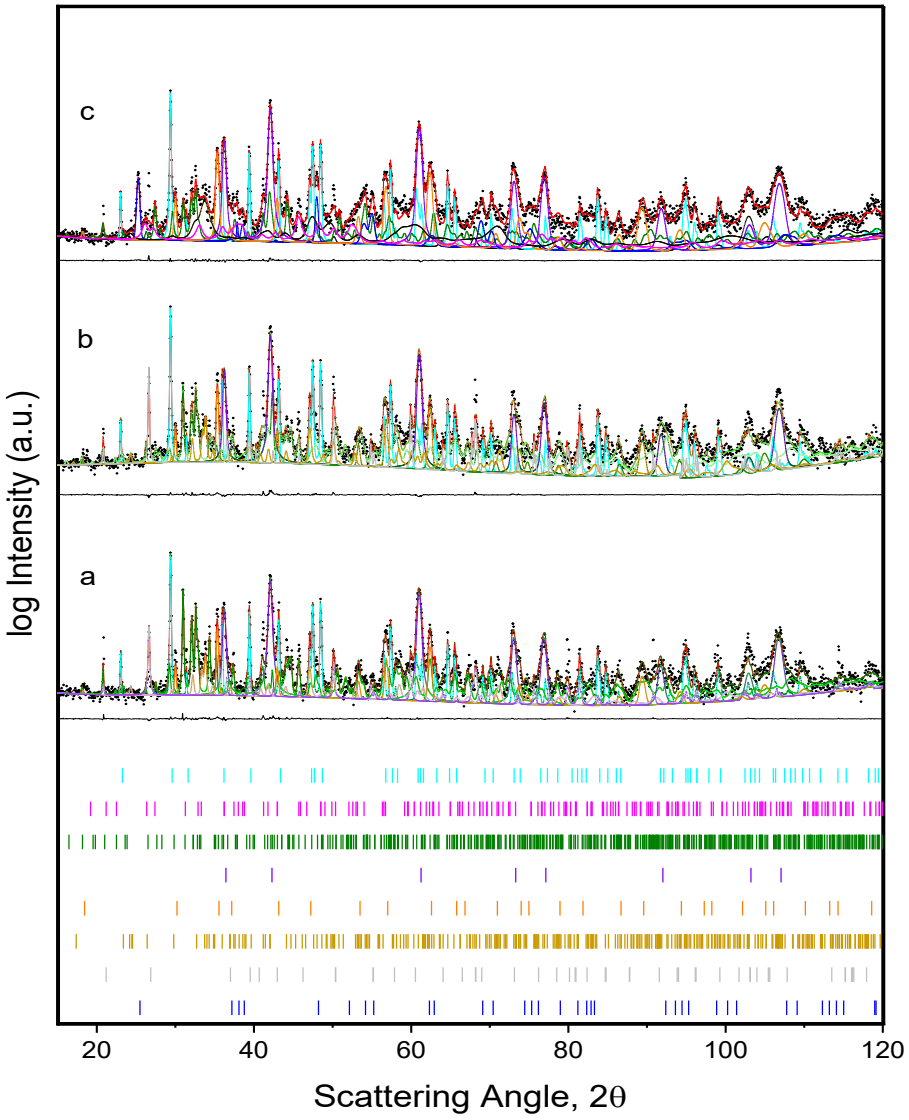

Figure 5.2.5: *Rietveld Refinement on XRD Pattern of pellet of steel slag after solar irradiation under 1 ml·min^{-1} gas flow (a), of pellet of steel slag after irradiation under 5 ml·min^{-1} gas flow (b) and of pellet of steel slag 10 wt % TiO_2 1hBM after solar irradiation under 5 ml·min^{-1} gas flow (c). Experimental data (black dots), calculated intensity (red line), calcite (cyan line), aragonite (magenta line), larnite (green line), wurstite (violet line), magnetite (orange line), brownmillerite (ocher line), quartz (gray line) and anatase TiO_2 (blue line) are reported. The difference between experimental and calculated data in linear scale and the stick pattern for all the phases, listed in descending order as above, are provided*

SEM images confirmed the formation of calcite crystals on the surface of the pellet after solar irradiation, as reported in the nice image of Figure 5.2.6, displaying the typical *pseudo-cubic shaped $CaCO_3$ calcite crystals*.

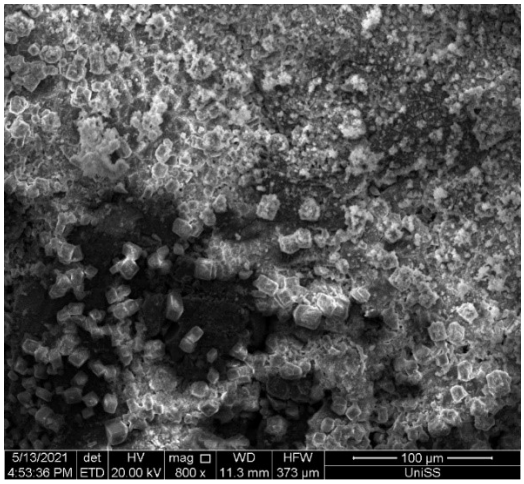

Figure 5.2.6: SEM image of steel slag pellet after irradiation test, pseudo-cubic shaped $CaCO_3$ calcite crystals can be recognized on the pellet surface[132]

XRD analysis on pellet of steel slag 10 wt % TiO_2 1hBM highlighted the formation of two polymorphous phases of calcium carbonate, $CaCO_3$ either in the phase calcite or in the phase aragonite (Figure 5.2.4). The total amount of carbonate produced was comparable with the amount observed with pristine steel slag after 3 hours of irradiation. The two calcium carbonate phases are produced by consumption of the larnite phase (Table 5.2.1).

The sigma-type shape of the kinetic curves and the relevant effect of the thermally induced CO_2 activation deserves some comments. The process under investigation occurs in heterogeneous phase, including a solid system, the steel slag pellet, a liquid phase, H_2O, which is adsorbed in the solid surface at the beginning of the reaction, and a gas mixture, CO_2/N_2, which flows along the reactor. It is likely that the CO_2 conversion process requires several steps including CO_2 physical and chemical adsorption, probably additional diffusion steps and subsequent absorption in the bulk, then the

chemical conversion itself, eventual subsequent desorption. The complexity of the process requires further insights, but at the present level of investigation it can be surmised that the initial stages of the process concern the CO_2 adsorption over the solid system together with its dissolution in the adsorbed H_2O. This agrees with the CO_2 decrease in the gas mixture outgoing from the reactor, which is observable since the very beginning of the treatment, although at a very low extent, and is followed by an increase in the conversion rate. These stages may be activated either by heating the chemical systems even at relatively low T, or by solar irradiation. The subsequent steps involving the chemical transformation of CO_2 may be more likely related to the photo activated processes.

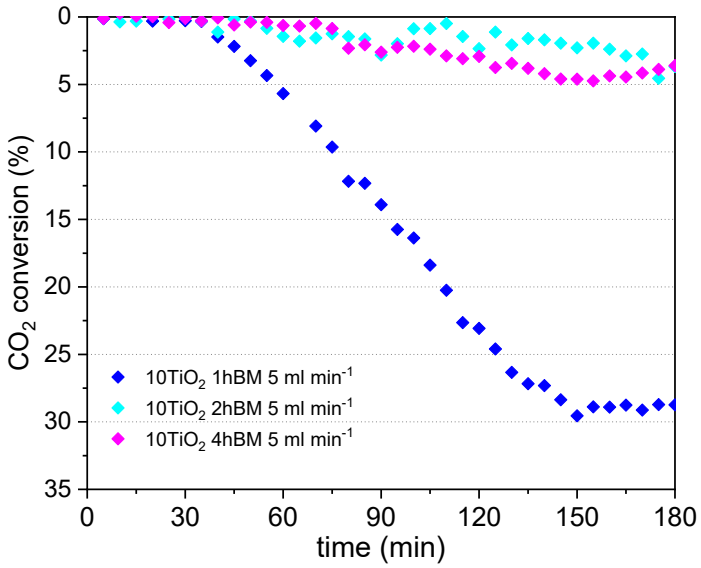

Figure 5.2.7: CO_2 conversion vs solar irradiation time for test conducted on pellet of steel slag modified with 10 wt % TiO_2 prepared with 1h (blue dots), 2h (cyan dots) and 4h (magenta dots) of high energy ball-milling under total gas flow of 5 ml·min^{-1} of a 10/90 CO_2/N_2 gas mixture

The previous results seem to indicate that, in spite of the widening of the band gap, the TiO_2 doped steel slag specimens did not show better performances in the CO_2

conversion with respect to the pristine steel slag systems. We then investigated the possible influence of extension of the ball-milling time of the TiO_2 modified systems, on the CO_2 conversion efficiency. Test in gas flow regime of the usual gas mixture were realised at a total flow of 5 $ml \cdot min^{-1}$

GC analysis performed during solar irradiation test highlighted the lower efficiency, in terms of CO_2 conversion, of the modified steel slag prepared for 2 hours and 4 hours of mechanical ball-milling if compared with the sample prepared for 1 hour of mechanical ball-milling (Figure 5.2.7). The two samples prepared for longer milling time show conversion below 5 % up to 4 hours of solar irradiation. In both cases, conversion start after the begin of the test and increases approximately linearly with respect to the irradiation time. The two modified materials seem to act roughly the same in terms of CO_2 conversion efficiency and they do not reach the conversion observed for the sample prepared with 1 hour of mechanical ball-milling treatment.

The Rietveld refinement on experimental XRD pattern acquired on pellet of modified steel slag after irradiation test in flow condition highlighted the formation of two different calcium carbonate phases (Figure 5.2.8). As for the already cited sample mechanically treated for 1 hour, both trigonal (calcite) and orthorhombic (aragonite) phases of $CaCO_3$ were formed by conversion of CO_2 by consumption of $CaSiO_4$ (larnite) phase. The significant decrease of larnite, from 44 wt % to 17-26 wt %, supports the hypothesis that the reaction of conversion occurs on this phase generating the two carbonates (Table 5.2.2). The trigonal calcite phase results the most abundant phase produced by on the pellet surfaces with a ratio varying from 5:1 to 3:1. As expected, considering the different conversion rates reached by the irradiation tests the total amount of carbonate produced by gaseous CO_2, the conversion is higher for the sample prepared with 1 hour of mechanical ball-milling. The total amount of carbonates on the surface results comparable for the samples obtained after 2 hours and 4 hours of mechanical ball-milling in accordance with the CO_2 conversion data observed.

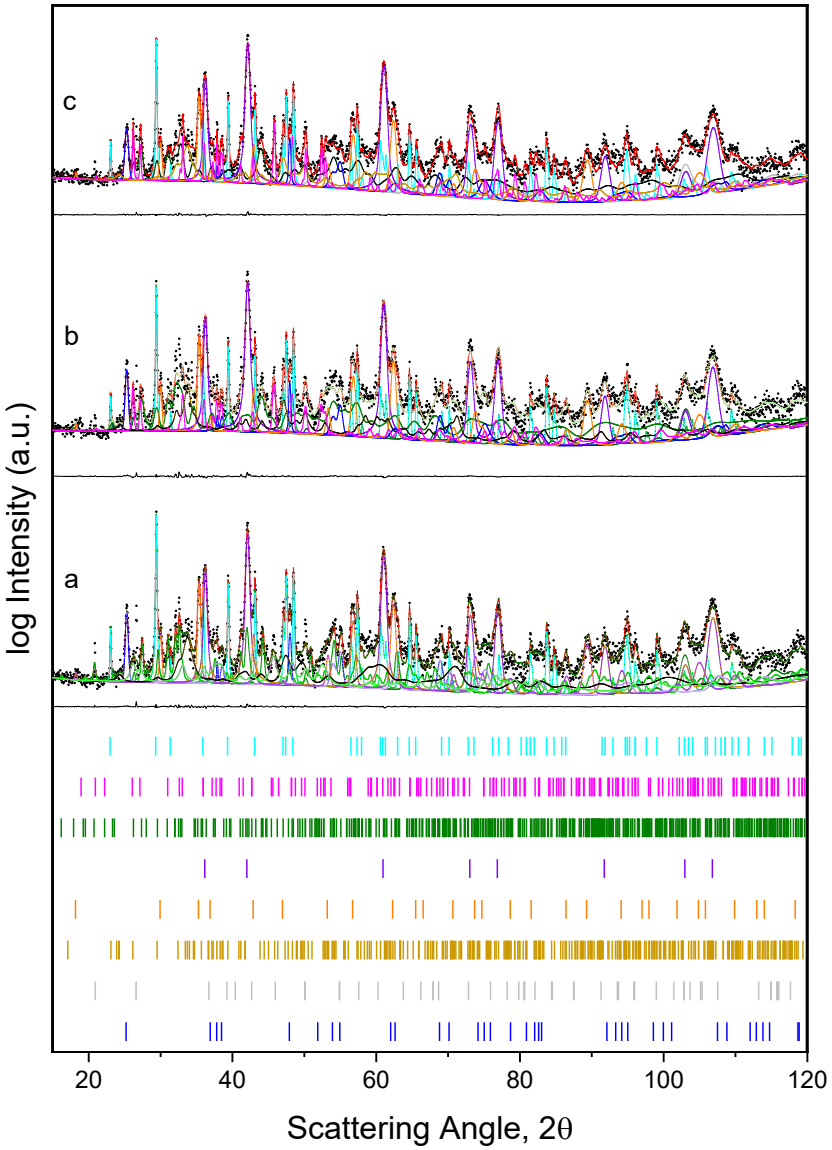

Figure 5.2.8: Rietveld Refinement on XRD Pattern of pellet of steel slag 10 wt % TiO_2 1hBM after solar irradiation (a), pellet of steel slag 10 wt % TiO_2 2hBM after solar irradiation (b), pellet of Steel slag 10 wt % TiO_2 4hBM after solar irradiation (c) . Experimental data (black dots), calculated intensity (red line), calcite (cyan line), aragonite (magenta line), larnite (green line), wurstite (violet line), magnetite (orange line), brownmillerite (ocher line), quartz (gray line) and anatase TiO_2 (blue line) are reported. The difference between experimental and calculated data in linear scale and the stick pattern for all the phases, listed in descending order as above, are provided

Table 5.2.2: Phase composition and cell parameters calculated via Rietveld refinement from XRD pattern on titania modified steel slag pellet after solar irradiation tests under flow of 10/90 CO_2/N_2 gas mixture 5 ml·min^{-1}

Sample	Crystalline phase	Wt %	Space Group	Cell parameters					
				a (Å)	b (Å)	c (Å)	α (°)	β (°)	γ (°)
Steel slag 10 wt % TiO_2 1hBM After test Rwp = 12	Larnite (Ca_2SiO_4)	16.7 ± 0.9	$P2_1/c$	5.51(3)	6.77(3)	9.24(2)	-	95.4(5)	-
	Wurstite (FeO)	24.7 ± 0.8	$Fm\bar{3}m$	4.29(2)	-	-	-	-	-
	Magnetite (Fe_3O_4)	6.8 ± 0.3	$Fd\bar{3}m$	8.42(0)	-	-	-	-	-
	Brownmillerite ($Ca_2(Al,Fe)_2O_5$)	11 ± 1	$Pcmn$	5.5(1)	14.7(3)	5.3(3)	-	-	-
	Quartz (SiO_2)	0.25 ± 0.04	$P3_221$	4.88(8)	-	5.4(4)	-	-	-
	TiO_2 anatase	5.8 ± 0.3	$I4_1/a$	3.79(0)	-	9.49(1)	-	-	-
	Calcite ($CaCO_3$)	28.8 ± 0.9	$R\bar{3}c$	4.99(1)	-	17.07(8)	-	-	-
	Aragonite ($CaCO_3$)	4.9 ± 0.6	$Pnma$	5.75(9)	4.98(3)	7.96(5)	-	-	-
Steel slag 10 wt % TiO_2 2hBM After test Rwp = 14	Larnite (Ca_2SiO_4)	26 ± 1	$P2_1/c$	5.52(7)	6.77(2)	9.3(1)	-	95.5(4)	-
	Wurstite (FeO)	29 ± 1	$Fm\bar{3}m$	4.29(3)	-	-	-	-	-
	Magnetite (Fe_3O_4)	7.3 ± 0.4	$Fd\bar{3}m$	8.41(9)	-	-	-	-	-
	Brownmillerite ($Ca_2(Al,Fe)_2O_5$)	8.2 ± 0.9	$Pcmn$	5.56(9)	14.5(6)	5.35(3)	-	-	-
	Quartz (SiO_2)	0.26 ± 0.04	$P3_221$	4.89(3)	-	5.4(2)	-	-	-
	TiO_2 anatase	5.9 ± 0.4	$I4_1/a$	3.79(2)	-	9.50(4)	-	-	-
	Calcite ($CaCO_3$)	18.7 ± 0.9	$R\bar{3}c$	4.99(3)	-	17.07(8)	-	-	-
	Aragonite ($CaCO_3$)	4.4 ± 0.5	$Pnma$	5.75(7)	4.97(7)	7.96(8)	-	-	-

Sample	Crystalline phase	Wt %	Space Group	Cell parameters					
				a (Å)	b (Å)	c (Å)	α (°)	β (°)	γ (°)
Steel slag 10 wt % TiO_2 4hBM After test Rwp = 11	Larnite (Ca_2SiO_4)	19 ± 1	$P2_1/c$	5.50	6.78	9.37	-	95.73	-
	Wurstite (FeO)	29 ± 1	$Fm\bar{3}m$	4.29	-	-	-	-	-
	Magnetite (Fe_3O_4)	7.5 ± 0.4	$Fd\bar{3}m$	8.42	-	-	-	-	-
	Brownmillerite ($Ca_2(Al,Fe)_2O_5$)	8.3 ± 0.9	*Pcmn*	5.55	14.60	5.37	-	-	-
	Quartz (SiO_2)	0.31 ± 0.5	$P3_221$	4.89	-	5.40	-	-	-
	TiO_2 anatase	4.9 ± 0.3	$I4_1/a$	3.79	-	9.50	-	-	-
	Calcite ($CaCO_3$)	22 ± 2	$R\bar{3}c$	4.99	-	17.07	-	-	-
	Aragonite ($CaCO_3$)	6.7 ± 0.5	*Pnma*	5.75	4.97	7.97	-	-	-

Modified steel slag particle size after the mechanical ball-milling treatment has been investigated via DLS analysis. A decrease in the particle size can be seen comparing the powders treated for 1 hour and 2 hours of ball-milling, respectively. It seems that after two hours of ball-milling the treatment is not able to affect further the particle size. The size distribution calculated from DLS analysis highlighted, indeed that particle size of the powders after 2 hours and 4 hours of mechanical ball mill are superimposable (Figure 5.2.9).

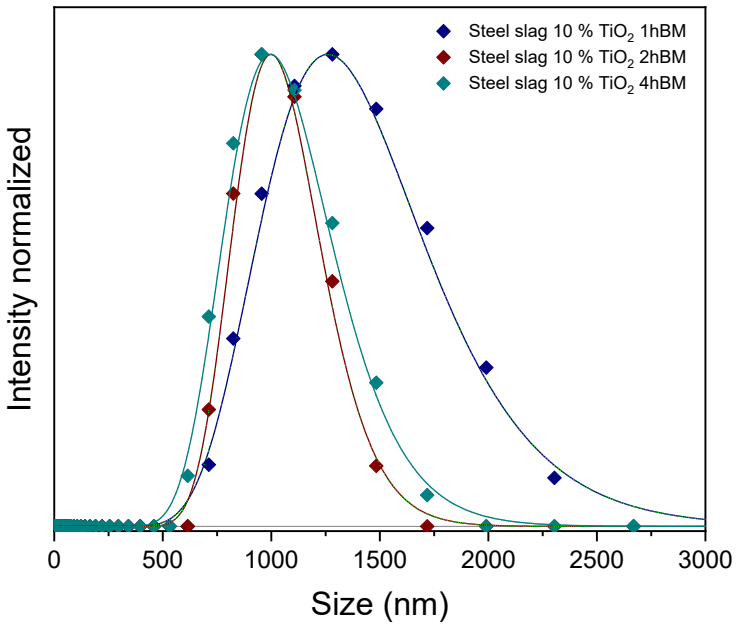

Figure 5.2.9: Particle size of steel slag modified with 10 wt % TiO_2 prepared with 1 hour, 2 hours and 4 hours of mechanical milling powders measured via DLS analysis

The mechanical ball-milling treatment causes a decrease in the crystallite size of the larnite in the sample and increase the number of lattice defects that eventually reduces the conversion efficiency of the material, as highlighted by GC and XRD analyses. DLS analysis suggests a trend of decrease conversion efficiency with the decrease of the particle size of the powders. This can also be attributed to a greater packing of the particle when in form of pellet. This is also supported by the decrease of the density of the pellet calculated via geometric method with the increase of mechanical ball-milling hours.

The conversion process observed on steel slag is attributable to an acid-base reaction. The influence of the material on the pH of water when dispersed and partially dissolved has been evaluated. Steel slag in water solution changes the pH from neutrality to slight basicity (9.8), this effect is emphasized by the TiO_2 doping (10.5). Those basic pH in water solution affect the $CO_2/HCO_3^-/CO_3^{2-}$ equilibrium promoting the formation of

CO_3^{2-} ions and so promoting the dissolution of CO_2 in water and, its fixation in form of metal carbonates on the pellet surfaces. The occurrence of carbonate species in water equilibrium further influences CO_2 reaction paths.

5.3 Conclusions

The experimental results highlighted the potentials of steel slag for CO_2 conversion processes. Pristine steel slag has shown high CO_2 conversion efficiency in the experimental condition tested. At low gas flow (1 ml·min^{-1}) the system are very efficient in terms of CO_2 conversion. At higher flow (5 ml·min^{-1}) the conversion process is characterized by a lower efficiency but high total CO_2 conversion. The tests support the hypothesis that both thermal and photochemical activation contribute to the final conversion observed. In order to increase the viability of photochemically-activated conversion on steel slag, the pristine powders have been modified with different oxides that allowed the decrease of the energy band gap of the material. The decrease of the energy band gap does not increase the efficiency of the conversion process for the sample modified with TiO_2 tested, especially at low gas flow condition.

The CO_2 was converted into calcium carbonate materials and fixated on the tested material surfaces as highlighted by XRD and SEM analysis.

6 RESULTS AND DISCUSSION: DUAL-PHASE MEMBRANES

Metal carbonate materials are employed in membrane preparation for high temperature (around 500 - 650 °C) applications [90]. Polymer membranes , typically used for low temperature purpose, offer better efficiency and selectivity but they are too fragile for high-stress applications [133]. The final goal is to test different metal carbonates compositions to achieve good permeation rates at lower temperatures and thus combining the good mechanical properties of metal supported dual-phase molten carbonate membranes with appreciable permeation rates.

6.1 Membranes preparation

Different binary and ternary alkaline carbonate mixtures were chosen for membrane preparation for their low melting temperatures.

The carbonate mixtures selected are reported in table 6.1.1. The carbonates salts were provided within Monolithos Catalysts and Recycling Ltd. supply chain with no further details provided other than the purity (Li_2CO_3 99.7%, Na_2CO_3 99.5%, K_2CO_3 99.9%). The three binary mixtures were selected within the compositions characterized by a melting temperature below 500 °C; two of them, Li_2CO_3/Na_2CO_3 52/48 mol % and Li_2CO_3/K_2CO_3 62/38 mol %, are the eutectic mixtures for their respective composition. The sodium-potassium carbonates eutectic mixture was not investigated due to its high melting temperature (710 °C) [92]. Ternary alkaline carbonate mixtures, namely $Li_2CO_3/Na_2CO_3/K_2CO_3$, were selected for their low melting temperatures. In particular, the study was focused on the eutectic ternary mixture (43.5/31.5/25 mol %), on the equimolar ternary mixture (33.3/33.3/33.3 mol %) , on the ternary mixtures prepared adding 5, 15 and 25 mol % of K_2CO_3, on the binary mixture Li_2CO_3/Na_2CO_3 52/48 mol %, on the ternary mixtures prepared adding 5, 15 and 25 mol % of Na_2CO_3, on the binary

mixture Li_2CO_3/K_2CO_3 62/38 mol %, and on the ternary mixtures prepared adding 5, 15 and 25 mol % of Na_2CO_3 on the binary mixture Li_2CO_3/K_2CO_3 52/48 mol %.

The melting temperature ranges were experimentally determined whereas the impregnation of the membrane was performed at higher temperatures with respect to the melting point.

Table 6.1.1: Tested carbonate mixtures molar ratio and melting temperatures

Carbonate Mixture	Molar Ratio (%)	Experimental Melting Temperature (°C)
Li_2CO_3/Na_2CO_3	52/48	500-550
Li_2CO_3/K_2CO_3	52/48	480-520
Li_2CO_3/K_2CO_3	62/38	500-530
$Li_2CO_3/Na_2CO_3/K_2CO_3$	49.4/45.6/5	500-530
$Li_2CO_3/Na_2CO_3/K_2CO_3$	44.2/40.8/15	500-530
$Li_2CO_3/Na_2CO_3/K_2CO_3$	39/36/25	450-520
$Li_2CO_3/Na_2CO_3/K_2CO_3$	49.4/5/45.6	480-530
$Li_2CO_3/Na_2CO_3/K_2CO_3$	44.2/15/40.8	470-520
$Li_2CO_3/Na_2CO_3/K_2CO_3$	39/25/36	450-500
$Li_2CO_3/Na_2CO_3/K_2CO_3$	58.9/5/36.1	500-550
$Li_2CO_3/Na_2CO_3/K_2CO_3$	52.7/15/32.3	480-530
$Li_2CO_3/Na_2CO_3/K_2CO_3$	46.5/25/28.5	470-520
$Li_2CO_3/Na_2CO_3/K_2CO_3$	43.5/31.5/25	430-500
$Li_2CO_3/Na_2CO_3/K_2CO_3$	33.3/33.3/33.3	500-550

Hollow stainless-steel cylinders with controlled porosity were chosen as membrane supports (Figure 6.1.1a), and the membrane impregnation was performed as follows. The carbonate mixtures were melted in a stainless-steel cylinder inside a cylindrical furnace with a thermocouple for temperature control. The stainless-steel porous supports were pre-heated in a furnace to avoid a rapid increase of the temperature during the impregnation procedure. The metal support was left in contact with the molten carbonates mixture for 10 s to ensure the diffusion of the carbonates into the

pores of the support. The impregnated membranes were then cooled at room temperature (Figure 6.1.1b) and subsequently calcinated in the furnace at appropriate temperature to eliminate the carbonate excess on the external parts of the membranes (Figure 6.1.1c). The mass of impregnated carbonates mixtures was evaluated by weighting the membrane before and after the impregnation procedure. The impregnation and calcination temperatures and the mass of carbonates obtained are reported in Table 6.1.2.

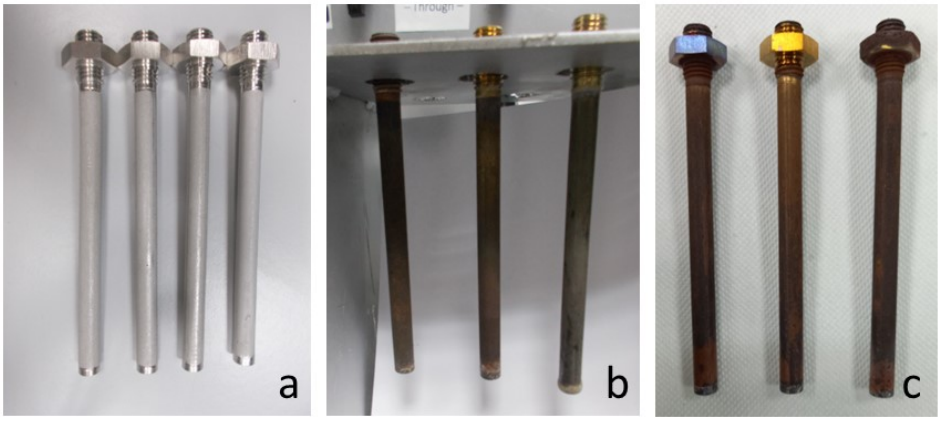

Figure 6.1.1: Stainless-steel support (a), membranes before calcination treatment (b) and after calcination (c)

Table 6.1.2: impregnation temperatures (°C) [a], calcination temperatures (°C) [b] and mass of impregnated carbonates for the prepared membranes (g) [c]

Carbonate Mixture		***a***	***b***	***c***
Li_2CO_3/Na_2CO_3	*52/48 mol %*	*630*	*600*	*2.85* *2.30*
Li_2CO_3/K_2CO_3	*62/38 mol %*	*600*	*600*	*3.80* *2.50*
Li_2CO_3/K_2CO_3	*52/48 mol %*	*570*	*570*	*2.85* *3.15*
$Li_2CO_3/Na_2CO_3/K_2CO_3$	*49.5/45.6/5 mol %*	*570*	*570*	*1.75* *3.65* *1.41*
$Li_2CO_3/Na_2CO_3/K_2CO_3$	*44.2/40.8/15 mol %*	*570*	*570*	*3.70* *2.55*
$Li_2CO_3/Na_2CO_3/K_2CO_3$	*39/36/25 mol %*	*580*	*580*	*2.00* *1.95* *3.23*
$Li_2CO_3/Na_2CO_3/K_2CO_3$	*49.5/5/45.6 mol %*	*570*	*570*	*3.30* *3.35*
$Li_2CO_3/Na_2CO_3/K_2CO_3$	*44.2/15/40.8 mol %*	*550*	*550*	*3.60* *4.35* *3.60*
$Li_2CO_3/Na_2CO_3/K_2CO_3$	*39/25/36 mol %*	*550*	*550*	*1.90* *3.65*
$Li_2CO_3/Na_2CO_3/K_2CO_3$	*58.9/5/36.1 mol %*	*570*	*570*	*3.60*
$Li_2CO_3/Na_2CO_3/K_2CO_3$	*52.7/15/32.3 mol %*	*570*	*570*	*2.58* *2.96*
$Li_2CO_3/Na_2CO_3/K_2CO_3$	*46.5/25/28.5 mol %*	*550*	*550*	*3.50* *3.22*
$Li_2CO_3/Na_2CO_3/K_2CO_3$	*58.9/5/36.1 mol %*	*570*	*570*	*3.35*
$Li_2CO_3/Na_2CO_3/K_2CO_3$	*52.7/15/32.3 mol %*	*570*	*570*	*4.20*
$Li_2CO_3/Na_2CO_3/K_2CO_3$	*33.3/33.3/33.3 mol %*	*600*	*600*	*2.10* *3.60*
$Li_2CO_3/Na_2CO_3/K_2CO_3$	*33.3/33.3/33.3 mol %*	*530*	*530*	*2.65* *3.44*
$Li_2CO_3/Na_2CO_3/K_2CO_3$	*43.5/31.5/25 mol %*	*530*	*530*	*3.95* *2.45*

6.2 Permeation Tests

Permeation tests were performed in the temperature range of 300-750 °C. The prepared membranes (Figure 6.1.1c) were screwed in a threaded stainless-steel cylinder with inlet and outlet line for gas flow as schematically reported in Figure 6.2.1. During the permeation test a gas mixture $CO_2/O_2/N_2$ (12/8/80 V/V %) was introduced with a final flow of 300 ml·min^{-1}. The mixture simulate the concentration of a combustion petroleum-based engine flue gasses [88]. The cylinder with the screwed membranes was allocated inside a furnace and the temperature inside the cylinder was monitored with a thermocouple inside the cylinder. The gas not permeating the membrane was then analysed via GC measurements.

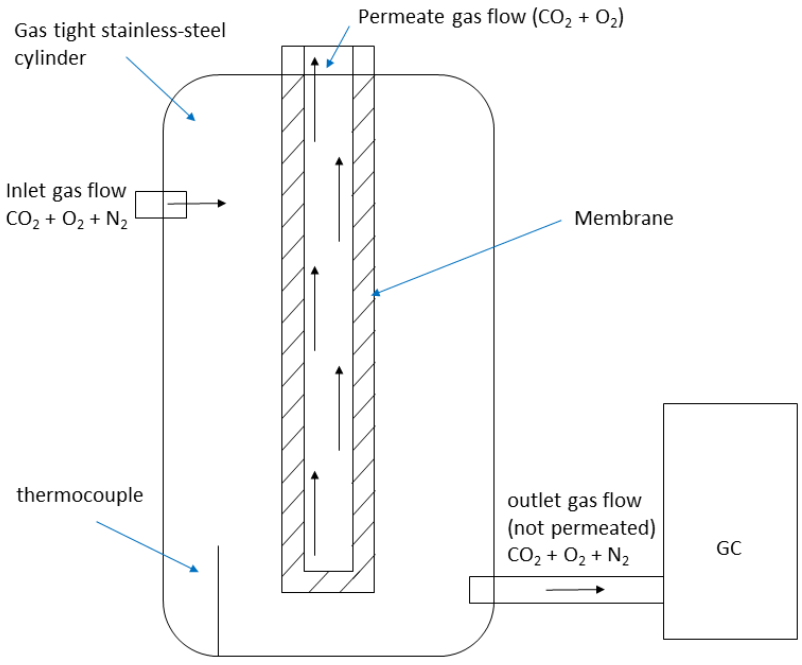

Figure 6.2.1: Experimental membrane gas permeation test section scheme

The Gas permeation rate, *r*, was calculated using the following formula:

$$r_x = \frac{G\left(C_{x(in)} - C_{x(out)}\right)}{V_m A} \tag{6.1}$$

where $C_{x(in)}$ and $C_{x(out)}$ are, respectively, the inlet and outlet gas concentration, G is the total gas flow, V_m is the molar volume and A the external surface membrane area. The gas outlet concentration was evaluated via GC area measurement.

The tests highlighted that O_2 and CO_2 permeation increase at high temperature (above 600 °C) for all the carbonates mixture tested (Figure 6.2.2). The best result, considering the maximum CO_2 permeation, was achieved with the 44.2/40.8/15 mol % $Li_2CO_3/Na_2CO_3/K_2CO_3$ mixture above 700 °C (CO_2 permeation rate above 0.20 $mol \cdot m^{-2} \cdot s^{-1}$). At lower temperatures, between 400 °C and 500 °C, any of the membranes tested shows the desired gas permeation rates (<0.5 $mol \cdot m^{-2} \cdot s^{-1}$). During the first tests, a problem concerning the ratio of permeated O_2 and CO_2 was observed. The two gasses permeate through a metal carbonate membrane in the form of CO_3^{2-} ions, as reported more extensively in paragraph 2.5, reacting at the membrane internal and external surface with the semi reactions:

$$CO_2 + \frac{1}{2}\, O_2 + 2e^- \rightarrow CO_3^{2-} \tag{6.2}$$

$$CO_3^{2-} \rightarrow CO_2 + \frac{1}{2}\, O_2 + 2e^- \tag{6.3}$$

The ratio between O_2 and CO_2 permeation rate is therefore determined by the reaction molar ratio. The O_2 permeation rate should be half those of CO_2. However, the experimental evidence, on different carbonate mixtures, shows comparable O_2 and CO_2 permeation rates, as reported in the Figures from 6.2.2a to 6.2.2d, or higher O_2 permeation rates (Figure 6.2.2e and Figure 6.2.2f). These experimental findings may suggest the occurrence of undesired O_2 consuming reactions affecting the molar ratio of the outlet gasses measured by GC analysis, which consequently leads to an increase in the apparent O_2 permeation rate.

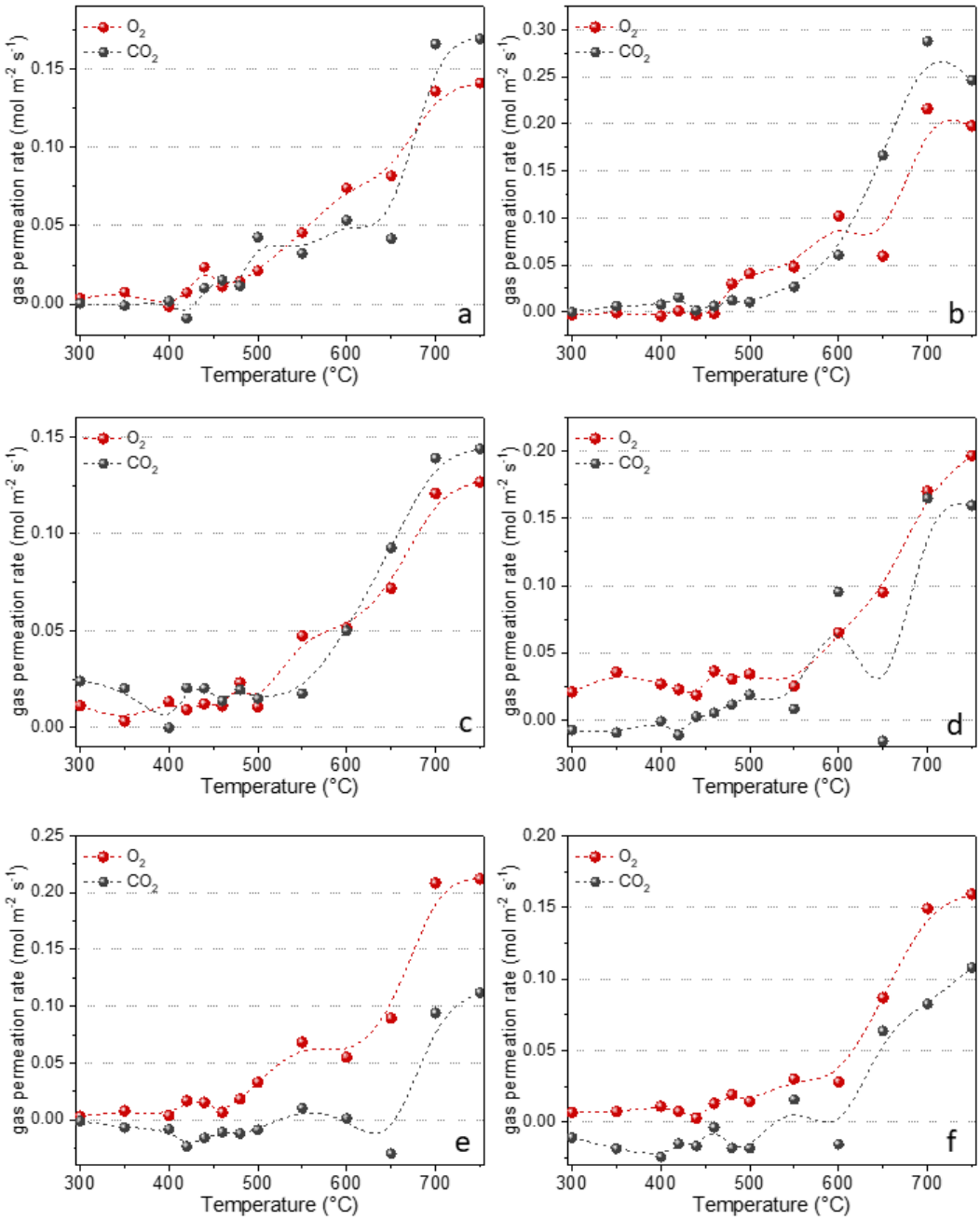

Figure 6.2.2: Gas permeation rates for tested membranes impregnated with carbonate mixtures $Li_2CO_3/Na_2CO_3/K_2CO_3$ 49.5/45.6/5 mol % (a), $Li_2CO_3/Na_2CO_3/K_2CO_3$ 44.2/40.8/15 mol % (b), $Li_2CO_3/Na_2CO_3/K_2CO_3$ 49.5/5/45.6 mol % (c), $Li_2CO_3/Na_2CO_3/K_2CO_3$ 44.2/15/40.8 mol % (d), $Li_2CO_3/Na_2CO_3/K_2CO_3$ 52.7/15/32.3 mol % (e) and $Li_2CO_3/Na_2CO_3/K_2CO_3$ 46.5/25/28.5 mol % (f)

A test performed on the stainless-steel support sustains the hypothesis that the O_2 reaction occurs at high temperatures. Furthermore, the analysis of the outlet gases, highlighted a decrease of the oxygen concentration while the carbon dioxide concentration kept constant (Figure 6.2.3). In absence of any reaction, the ratio between the gas should have been constant and no permeation should have been measured. During the test the gas mixture, flowing through the inlet, should have been split between the outlet and the pores of the membranes. That's because the pores are large enough to let all the gaseous molecules (N_2, CO_2, O_2) to cross the support.

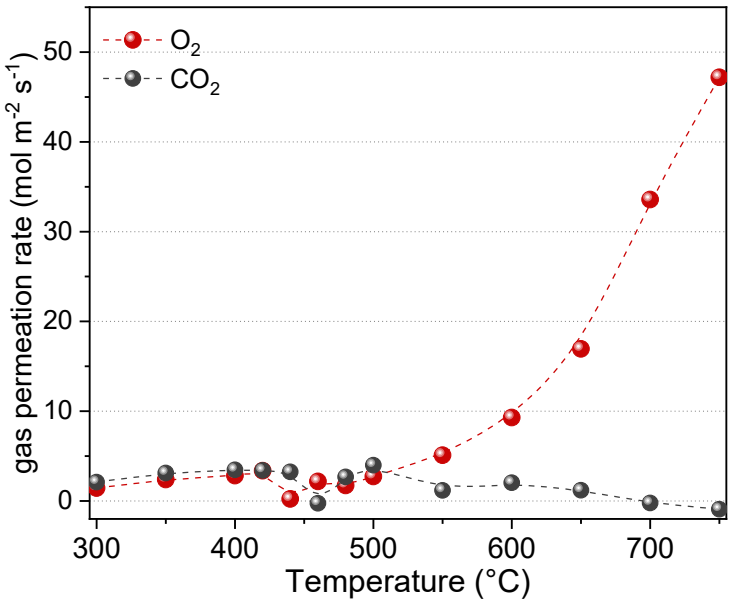

Figure 6.2.3: O_2 and CO_2 percentage concentration reduction for a stainless-teel support in the temperature range 300 °C – 750 °C

In order to confirm that hypothesis, a further test was performed on the pristine support measuring the outlet flow and the permeate flow changes vs the temperature. The flow was measured first during the heating and then during the cooling. As highlighted in Figure 6.2.4 the outlet flow increases while the permeate flow decrease as increasing the temperature. This could be ascribable to thermal dilatation phenomenon but also to O_2 reaction with the stainless-steel support. During cooling it

was observed that the permeation rate is lower than the one measured before the treatment supporting the hypothesis of an irreversible change affecting the pore size of the membrane, therefore not attributable to thermal dilatation. The lesser efficiency can be attributed to O_2 reaction with stainless-steel support.

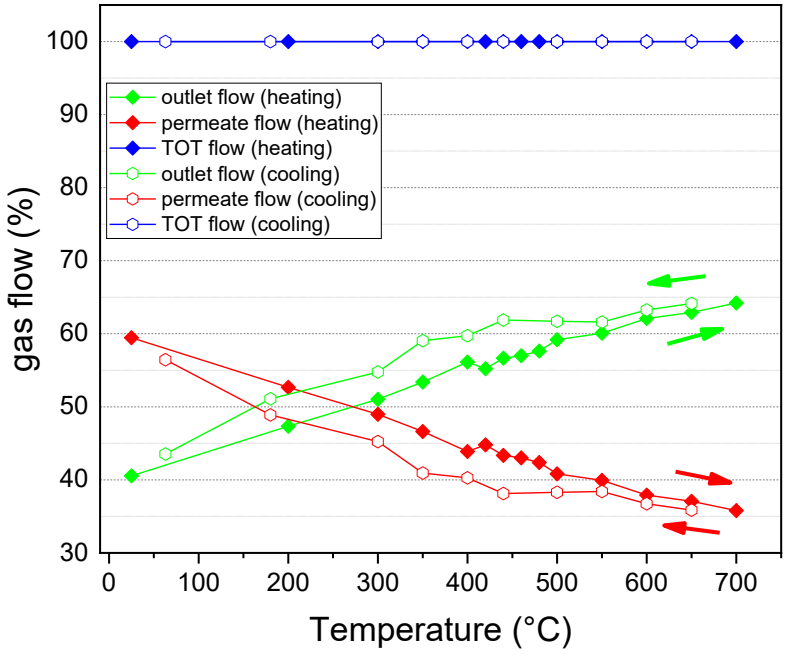

Figure 6.2.4: Permeate gas flow and outlet gas flow dependence over temperature, the flow was measured first during the heating (full dots) and after during cooling (hollow dots)

The carbonate mixture impregnation partially keeps the membrane during permeation test but the O_2 permeation rates observed are still a result of two different contribution: the O_2 permeation through the membrane and the reaction of O_2 with the support that causes a decrease in the O_2 concentration determined by GC analysis.

The stainless-steel selected for supports used in the experimental tests (SS 316) should not react with O_2 in the range of temperatures tested [134]. However, this is not true for all stainless-steel compositions available on the market. Experimental findings,

hence, suggest that supports with a different stainless-steel composition might have been acquired affecting the integrity and the efficiency of the prepared membranes.

6.3 Conclusions

Even if the experimental results were negatively affected by the support stainless steel behaviour, it was proved the potentialities metal carbonates reutilization as integral part of membranes for gas mixture separation in industrial environment.

The tests highlighted that alkaline carbonate stainless steel supported dual phase membranes, are able to separate CO_2 and O_2 from a simulated flue gas, but the carbonate mixtures tested were not able to achieve a desirable permeation rate below 500 °C.

As alkaline-earth carbonates addition can lower the melting temperature of an alkaline carbonate mixtures, $CaCO_3$ and $MgCO_3$ (produced by CO_2 fixation on silicate materials via photochemical activation during my thesis) could induce better permeation rates at low temperatures if implemented in the dual phase membranes [135]. However, the cited issues emerged with the stainless-steel supports, limited the investigation and the experimental tests over those materials.

7 CONCLUSIONS

The investigation of innovative materials, processes, and technologies for the CO_2 emission control, to be reached through its storage and conversion, represents, nowadays, a relevant challenge, which is attracting the efforts of a large scientific community. Despite the large number of experimental activities, as well as of theoretical and modelling studies, most of the work developed so far refers to approaches not sustainable in view of a wide scale implementation, including, for example, catalytic processes occurring at high temperatures, or the use of solid substrates made by precious metals or relative compounds.

Conversely, the attempt to set up new routes to face the CO_2 related issues, based on harvesting the energy produced by renewable sources, and on the activation of CO_2 conversion over low value and raw materials, as well as over industrial wastes, is quite recent. The experimental activities carried out during the Doctoral period, and presented in this thesis, were addressed along this line, and the general objective was to study solar-driven photochemical CO_2 conversion strategies on low-cost and high abundant silicate-based materials, like olivine and electric arc furnace steel slags.

Such materials are not intrinsic semiconductors, able to harvest radiative energy in the UV-Visible range through the creation of electron-hole pairs, but their multiphase structural composition, and the possibility to influence the electronic properties through doping effects, makes them of potential interest for the cited processes.

The experimental findings indicated that, while pristine olivine is not suitable for solar-driven photochemical activated CO_2 conversion strategies, due to its low efficiency in harvesting the solar irradiance, TiO_2 modified olivine has proven to be effective, in presence of H_2O and CO_2, to convert the CO_2 into light hydrocarbons and metal carbonates such as $MgCO_3 \cdot 3H_2O$. TiO_2 doping was performed via mechanical treatment and via impregnation methods, and the effect of the doping method was investigated in a suitably set-up reactor, under batch-type conditions. The impregnated samples

have proven to be more effective in converting the CO_2, with respect to the pristine olivine, and the observed conversion rate values are comparable with those reported in the literature, reaching high values observed even for thermally activated processes. The two main products of CO_2 conversion seem to be formed by different competitive reaction routes. A linear trend of the CO_2 conversion, versus the irradiation time, characterised such TiO_2-modified olivine sample prepared by impregnation.

The other class of investigated materials, electric arc furnace steel slags, have proven to be very efficient toward CO_2 conversion via solar-driven photochemical activation. The CO_2 was converted into calcium carbonates, while no other gaseous products, arising from CO_2 reduction, were formed. The high value of pH induced by steel slags to H_2O solution favours the interaction of the gaseous CO_2 with H_2O, and subsequent HCO_3^- formation. The experimental results relevant to the CO_2 conversion tests carried out in a flow type reactor, suggest that both photochemical activation and thermal activation, triggered by the solar irradiation, contributed to the reaction. The CO_2 conversion on the steel slags seems to start after an initial induction period, and the kinetics proceeds according to a sigmoidal trend, which includes different steps as gas adsorption, diffusion phenomena, CO_2 chemical conversion, new solid phases precipitation, etc. The comprehension of the mechanistic details requires further deepening, and it will be one the objectives of the study prosecution. TiO_2 doping on the steel slags proved to be effective in decreasing the energy band gap of the material, but it did not induce a beneficial effect in terms of CO_2 conversion, and, rather, led to a decrease in the conversion values.

A further CO_2 related issue was considered within the Doctoral activities: in a circular vision of CO_2 life, the research on potential applications and the development of new technologies for the reutilization of the converted CO_2 are nowadays of high interest. Carbonate-based dual-phase membranes can lead to the reutilization of the metal carbonate materials produced by CO_2 conversion processes. These membranes can be implemented to separate CO_2 and O_2 from flue gas mixtures. The investigation on

membranes prepared with several alkaline carbonate mixtures highlighted differences in the behaviour and in the efficiency of the several studied materials, indicating, however, efficient gas permeation rates at high temperatures, i.e. above 500 °C. It also emerged the critical role played by the stainless-steel supports of the membranes, which influenced the permeation process. The optimization of the inert materials for carbonate supports, and the selection of further mixtures of alkaline- and alkaline-earth-carbonates will be the focus of the study prosecution which will, hopefully, lead to set up efficient permeation rates at lower temperatures.

BIBLIOGRAPHY

[1] Trends in CO2, Global Monitoring Laboratory. (2023). https://gml.noaa.gov/ccgg/trends/.

[2] G.D. Amato, H.J. Chong-Neto, O.P. Monge Ortega, C. Vitale, I. Ansotegui, N. Rosario, T. Haahtela, C. Galan, R. Pawankar, M. Murrieta-Aguttes, L. Cecchi, C. Bergmann, E. Ridolo, G. Ramon, S. Gonzalez Diaz, M. D'Amato, I. Annesi-Maesano, The effects of climate change on respiratory allergy and asthma induced by pollen and mold allergens, Allergy. 75 (2020) 2219–2228. doi:10.1111/all.14476.

[3] M. Scheffer, V. Brovkin, P.M. Cox, Positive feedback between global warming and atmospheric CO 2 concentration inferred from past climate change, Geophysical Research Letters. 33 (2006) 2–5. doi:10.1029/2005GL025044.

[4] T.M. Gür, Carbon Dioxide Emissions , Capture , Storage and Utilization : Review of Materials , Processes and Technologies, Progress in Energy and Combustion Science. 89 (2022) 100965. doi:10.1016/j.pecs.2021.100965.

[5] J.K. Stolarczyk, S. Bhattacharyya, L. Polavarapu, J. Feldmann, Challenges and Prospects in Solar Water Splitting and CO2 Reduction with Inorganic and Hybrid Nanostructures, ACS Catalysis. 8 (2018) 3602–3635. doi:10.1021/acscatal.8b00791.

[6] M. Wiatros-Motyka, D. Jones, Global Electricity Mid-Year Insights, 2022.

[7] H. Bahar, Renewable Energy Market Update, 2023.

[8] J. Ma, L. Li, H. Wang, Y. Du, J. Ma, X. Zhang, Carbon Capture and Storage : History and the Road Ahead, 14 (2022) 33–43. doi:10.1016/j.eng.2021.11.024.

[9] F.D. Meylan, V. Moreau, S. Erkman, CO 2 utilization in the perspective of industrial ecology , an overview, Journal of CO2 Utilization. 12 (2015) 101–108. doi:10.1016/j.jcou.2015.05.003.

[10] S. Vaz, A.P. Rodrigues de Souza, B.E. Lobo Baeta, Technologies for carbon dioxide capture : A review applied to energy sectors, Cleaner Engineering and Technology. 8 (2022) 100456. doi:10.1016/j.clet.2022.100456.

[11] Trends in Atmospheric Carbon Dioxide - Monthly average Mauna Loa CO2, Global Monitoring Laboratory. (2023). https://gml.noaa.gov/ccgg/trends/.

[12] R. Rennie, J. Law, A Dictionary of Chemistry, 7th ed., Oxford University Press, 2016.

[13] K.K. Rohatgi-Mukherjee, Fundamentals of Photochemistry, New Age International limited, publishers, 1978.

[14] K. Li, B. Peng, T. Peng, Recent Advances in Heterogeneous Photocatalytic CO2 Conversion to Solar Fuels, ACS Catalysis. 6 (2016) 7485–7527. doi:10.1021/acscatal.6b02089.

[15] John A. Dutton Istitute for Teaching and Learning Excellence, The Solar Spectrum, PennState. (n.d.). https://www.e-education.psu.edu/meteo300/node/683.

[16] N.G. Holm, C. OZe, O. Mousis, J.H. Waite, A. Guilbert-Lepoutre, Serpentinization and the Formation of H2 and CH4 on Celestial Bodies (Planets, Moons, Comets), Astrobiology. 15 (2015) 587–600. doi:10.1089/ast.2014.1188.

[17] V. Farina, N.S. Gamba, F. Gennari, S. Garroni, F. Torre, A. Taras, S. Enzo, G. Mulas, CO 2 Hydrogenation Induced by Mechanochemical Activation of Olivine With Water Under CO 2 Atmosphere, Frontiers in Energy Research. 7 (2019) 1–10. doi:10.3389/fenrg.2019.00107.

[18] F. Torre, V. Farina, A. Taras, C. Pistidda, A. Santoru, J. Bednarcik, G. Mulas, S. Enzo, S. Garroni, Room temperature hydrocarbon generation in olivine powders: Effect of mechanical processing under CO2 atmosphere, Powder Technology. 364 (2020) 915–923. doi:10.1016/j.powtec.2019.10.080.

[19] F. Wang, D. Dreisinger, M. Jarvis, T. Hitchins, D. Dyson, Quantifying kinetics of mineralization of carbon dioxide by olivine under moderate conditions, Chemical Engineering Journal. 360 (2019) 452–463. doi:10.1016/j.cej.2018.11.200.

[20] A. Modak, P. Bhanja, S. Dutta, B. Chowdhury, A. Bhaumik, Catalytic reduction of CO2 into fuels and fine chemicals, Green Chemistry. 22 (2020) 4002–4033. doi:10.1039/d0gc01092h.

[21] S. Bajpai, N. Shreyash, S. Singh, A.R. Memon, M. Sonker, S.K. Tiwary, S. Biswas, Opportunities , challenges and the way ahead for carbon capture , utilization and sequestration (CCUS) by the hydrocarbon industry : Towards a sustainable future, Energy Reports. 8 (2022) 15595–15616. doi:10.1016/j.egyr.2022.11.023.

[22] Q. Lin, X. Zhang, T. Wang, C. Zheng, X. Gao, Technical Perspective of Carbon Capture , Utilization , and Storage, Engineering. 14 (2022) 27–32. doi:10.1016/j.eng.2021.12.013.

[23] E. Liu, X. Lu, D. Wang, A Systematic Review of Carbon Capture, Utilization and Storage : Status , Progress and Challenges, Energies. 16 (2023) 2865. doi:doi.org/10.3390/en16062865.

[24] A. Sanna, M. Uibu, G. Caramanna, R. Kuusik, M.M. Maroto-Valer, A Review of mineral carbonation technologies to sequester CO2, Chem Soc Rev. 43 (2014) 8049–8080. doi:10.1039/c4cs00035h.

[25] O.S. Pokrovsky, J. Schott, F. Thomas, Dolomite surface speciation and reactivity in aquatic systems, Geochimica et Cosmochimica Acta. 63 (1999) 3133–3143.

[26] A.A. Olajire, A review of mineral carbonation technology in sequestration of CO 2, Journal of Petroleum Science and Engineering. 109 (2013) 364–392. doi:10.1016/j.petrol.2013.03.013.

[27] S. Yadav, A. Mehra, A review on ex situ mineral carbonation, Environmental Science and Pollution Research. (2021) 12202–12231. doi:doi.org/10.1007/s11356-020-12049-4.

[28] H. Guzman, F. Salomone, S. Bensaid, M. Castellino, N. Russo, S. Hernandez, CO 2 Conversion to Alcohols over Cu / ZnO Catalysts : Prospective Synergies between Electrocatalytic and Thermocatalytic Routes, ACS Applied Materials & Interfaces. 14 (2022) 517–530. doi:10.1021/acsami.1c15871.

[29] J.-I. Makiura, S. Kakihara, T. Higo, N. Ito, Y. Hirano, Y. Sekine, Efficient CO2 conversion to CO using chemical looping over Co-In oxide, Chemical Communications. 58 (2022) 4837. doi:10.1039/d2cc00208f.

[30] Z. Wang, J. Chen, X. Qiu, J.-G. Ma, P. Cheng, Conversion of CO 2 to Heterocyclohexenol Carboxylic Acids through a Metal − Organic Framework Sponge, ACS Applied Materials & Interfaces. 13 (2021) 7389–7395. doi:10.1021/acsami.1c00844.

[31] J. Wei, Q. Ge, R. Yao, Z. Wen, C. Fang, L. Guo, H. Xu, J. Sun, Directly converting CO 2 into a gasoline fuel, Nature Communications. 8 (2017) 15174. doi:10.1038/ncomms15174.

[32] H.M. Jhong, S. Ma, P.J.A. Kenis, Electrochemical conversion of CO 2 to useful chemicals : current status , remaining challenges , and future opportunities, Current Opinion in Chemical Engineering. 2 (2013) 191–199. doi:10.1016/j.coche.2013.03.005.

[33] A. Saravanan, P. Senthil kumar, D.N. Vo, S. Jeevanantham, V. Bhuvaneswari, V. Anantha Narayanan, P.R. Yaashikaa, S. Swetha, B. Reshma, A comprehensive review on different approaches for CO2 utilization and conversion pathways, Chemical Engineering Science. 236 (2021) 116515. doi:10.1016/j.ces.2021.116515.

[34] B. Zha, C. Li, J. Li, Efficient electrochemical reduction of CO2 into formate and acetate in polyoxometalate catholyte with indium catalyst, Journal of Catalysis. 382 (2020) 69–76. doi:10.1016/j.jcat.2019.12.010.

[35] D. Gao, W. Li, H. Wang, G. Wang, R. Cai, Heterogeneous Catalysis for - CO 2

Conversion into Chemicals and Fuels, Transactions of Tianjin University. 28 (2022) 245–264. doi:10.1007/s12209-022-00326-x.

[36] Z. Zhao, M. Wang, P. Ma, Y. Zheng, J. Chen, H. Li, X. Zhang, K. Zheng, Q. Kuang, Z. Xie, Atomically dispersed Pt / CeO 2 catalyst with superior CO selectivity in reverse water gas shift reaction, Applied Catalysis B: Environmental. 291 (2021) 120101. doi:10.1016/j.apcatb.2021.120101.

[37] J. Ma, N. Sun, X. Zhang, N. Zhao, F. Xiao, W. Wei, Y. Sun, A short review of catalysis for CO2 conversion, Catalysis Today. 148 (2009) 221–231. doi:10.1016/j.cattod.2009.08.015.

[38] Z. Hou, P. Chen, H. Fang, X. Zheng, T. Yashima, Production of synthesis gas via methane reforming with CO2 on noble metals and small amount of noble- (Rh-) promoted Ni catalysts, International Journal of Hydrogen Energy. 31 (2006) 555–561. doi:10.1016/j.ijhydene.2005.06.010.

[39] M. Rezaei, S.M. Alavi, S. Sahebdelfar, Z. Yan, Syngas Production by Methane Reforming with Carbon Dioxide on Noble Metal Catalysts, Journal of Natural Gas Chemistry. 15 (2006) 327–334. doi:doi.org/10.1016/S1003-9953(07)60014-0.

[40] M. Hofmann, H. Hofmann, C. Hagelüken, A. Hool, Critical raw materials : A perspective from the materials science community, Sustainable Materials and Technologies. 17 (2018) e00074. doi:10.1016/j.susmat.2018.e00074.

[41] A. Galadima, O. Muraza, Catalytic thermal conversion of CO 2 into fuels : Perspective and challenges, Renewable and Sustainable Energy Reviews. 115 (2019) 109333. doi:10.1016/j.rser.2019.109333.

[42] X. Li, L. Wang, W. Su, Y. Xing, A Review of the research status of CO2 photocatalytic conversion technology based on bibliometrics, New Journal of Chemistry. 45 (2021) 2315–2325. doi:10.1039/d0nj04597g.

[43] P.R. Yaashikaa, P. Senthil Kumar, S.J. Varjani, A. Saravanan, A review on photochemical , biochemical and electrochemical transformation of CO2 into

value-added products, Journal of CO2 Utilization. 33 (2019) 131–147. doi:10.1016/j.jcou.2019.05.017.

[44] V. Kumaravel, J. Bartlett, S.C. Pillai, Photoelectrochemical Conversion of Carbon Dioxide (CO2) into Fuels and Value-Added Products, ACS Energy Letters. 5 (2020) 486–519. doi:10.1021/acsenergylett.9b02585.

[45] T. Inoue, A. Fujishima, S. Konishi, K. Honda, Photoelectrocatalytic reduction of carbon dioxide in aqueous suspensions of semiconductor powders, Nature. 277 (1979) 637–638. doi:doi.org/10.1038/277637a0.

[46] G. Yin, M. Nishikawa, Y. Nosaka, N. Srinivasan, D. Atarashi, E. Sakai, M. Miyauchi, Photocatalytic Carbon Dioxide Reduction by Copper Oxide Nanocluster-Grafted Niobate Nanosheets, ACS Nano. 9 (2015) 2111–2119. doi:10.1021/nn507429e.

[47] L. Ye, J. Mao, T. Peng, L. Zan, Y. Zhang, Opposite photocatalytic activity orders of low-index facets of anatase TiO2 for liquid phase dye degradation and gaseous phase CO2 photoreduction, Physical Chemistry Chemical Physics. 16 (2014) 15675–15680. doi:10.1039/c4cp01488j.

[48] H. Zhao, L. Liu, A.J. M;, Y. Li, Bicrystalline TiO2 with controllable anatase–brookite phase content for enhanced CO2 photoreduction to fuels, Journal of Materials Chemistry A. 1 (2013) 8209–8216. doi:10.1039/c3ta11226h.

[49] F. Gonell, A. V Puga, B. Julián-lópez, H. García, A. Corma, Copper-doped titania photocatalysts for simultaneous reduction of CO2 and production of H2 from aqueous sulfide, Applied Catalysis B: Environmental. 180 (2016) 263–270. doi:10.1016/j.apcatb.2015.06.019.

[50] Z. Zhang, Z. Huang, X. Cheng, Q. Wang, Y. Chen, P. Dong, X. Zhang, Product selectivity of visible-light photocatalytic reduction of carbon dioxide using titanium dioxide doped by different nitrogen-sources, Applied Surface Science. 355 (2015) 45–51. doi:10.1016/j.apsusc.2015.07.097.

[51] M. Mei Gui, W. Ming Ping Wong, S. Chai, A.M. Rahman, One-pot synthesis of Ag-

MWCNT @ TiO 2 core – shell nanocomposites for photocatalytic reduction of CO 2 with water under visible light irradiation, Chemical Engineering Journal. 278 (2015) 272–278. doi:10.1016/j.cej.2014.09.022.

[52] Z. Fang, S. Li, Y. Gong, W. Liao, S. Tian, C. Shan, C. He, Comparison of catalytic activity of carbon-based AgBr nanocomposites for conversion of CO 2 under visible light, Journal of Saudi Chemical Society. 18 (2014) 299–307. doi:10.1016/j.jscs.2013.08.003.

[53] B. Garcia, V. Beaumont, E. Perfetti, V. Rouchon, D. Blanchet, P. Oger, G. Dromart, A. Huc, F. Haeseler, Experiments and geochemical modelling of CO2 sequestration by olivine : Potential , quantification, Applied Geochemistry. 25 (2010) 1383–1396. doi:10.1016/j.apgeochem.2010.06.009.

[54] B.P. Mcgrail, H.T. Schaef, A.M. Ho, Y. Chien, J.J. Dooley, C.L. Davidson, Potential for carbon dioxide sequestration in flood basalts, Journal of Geophysical Research. 111 (2006) 1–13. doi:10.1029/2005JB004169.

[55] R.D. Schuiling, Olivine : a supergreen fuel, Energy, Sustainability and Society. 18 (2013) 2–5. doi:doi.org/10.1186/2192-0567-3-18.

[56] E.H. Oelkers, S.R. Gislason, J. Matter, Mineral Carbonation of CO2, Elements. 4 (2008) 333–338. doi:10.2113/gselements.4.5.333.

[57] P. Kelemen, S.M. Benson, H. Pilorgé, P. Psarras, J. Wilcox, An Overview of the Status and Challenges of CO2 Storage in Minerals and Geological Formations, Frontiers in Climate. 1 (2019) 1–20. doi:10.3389/fclim.2019.00009.

[58] U.S.P.R. Arachchige, P.W. Sakuna Sandupama, What To Do With CO2 ? Storage Vs . EOR Vs . CO2 As A Chemical Feedstock, International Journal of Advanced Research and Publications. 3 (2019) 104–109.

[59] S. Peuble, M. Godard, L. Luquot, M. Andreani, I. Martinez, P. Gouze, CO2 geological storage in olivine rich basaltic aquifers : New insights from reactive-percolation experiments, Applied Geochemistry. 52 (2015) 174–190.

doi:10.1016/j.apgeochem.2014.11.024.

[60] S.J. Gerdemann, D.C. Dahlin, W.K. O'Connor, L.R. Penner, G.E. Rush, Ex-Situ and In-Situ Mineral Carbonation as a Means to Sequester Carbon Dioxide, (2004) 17.

[61] N.C. Johnson, B. Thomas, K. Maher, R.J. Rosenbauer, D. Bird, G.E. Brown, Olivine dissolution and carbonation under conditions relevant for in situ carbon storage, Chemical Geology. 373 (2014) 93–105. doi:10.1016/j.chemgeo.2014.02.026.

[62] C.E. Wood, O. Qafoku, J.S. Loring, A.M. Chaka, Role of Fe (II) Content in Olivine Carbonation in Wet Supercritical, (2019). doi:10.1021/acs.estlett.9b00496.

[63] C. Courson, L. Udron, C. Petit, A. Kiennemann, L. Liu, Grafted NiO on natural olivine for dry reforming of methane, Science and Technology of Advanced Materials. 3 (2002) 271–282. doi:10.1016/S1468-6996(02)00026-8.

[64] J.N. Kuhn, Z. Zhao, A. Senefeld-naber, L.G. Felix, R.B. Slimane, C.W. Choi, U.S. Ozkan, Ni-olivine catalysts prepared by thermal impregnation : Structure , steam reforming activity , and stability, Applied Catalysis A: General. 341 (2008) 43–49. doi:10.1016/j.apcata.2007.12.037.

[65] T.M. Mccollom, Abiotic methane formation during experimental serpentinization of olivine, Proceedings of the National Academy of Sciences. 113 (2016) 13965–13970. doi:10.1073/pnas.1611843113.

[66] E. Escamilla-roa, M. Zorzano, J. Martin-torres, A. Hernàndez-Laguna, C.I. Sainz-díaz, DFT study of electronic and redox properties of TiO2 supported on olivine for modelling regolith on Moon and Mars conditions, Planetary and Space Science. 180 (2020) 104760. doi:10.1016/j.pss.2019.104760.

[67] I.A. Shkrob, S.D. Chemerisov, T.W. Marin, Photocatalytic Decomposition of Carboxylated Molecules on Light-Exposed Martian Regolith and Its Relation to Methane Production on Mars, Astrobiology. 10 (2010) 425–436. doi:10.1089/ast.2009.0433.

[68] S. Pan, R. Adhikari, Y. Chen, P. Li, P. Chiang, Integrated and innovative steel slag utilization for iron reclamation , green material production and CO2 fixation via accelerated carbonation, Journal of Cleaner Production. 137 (2016) 617–631. doi:10.1016/j.jclepro.2016.07.112.

[69] W.M. Mayes, A.L. Riley, H.I. Gomes, P. Brabham, J. Hamlyn, H. Pullin, P. Renforth, Atmospheric CO2 sequestration in iron and steel slag : Consett , Co . Durham , UK, Environmental Science & Technology. 52 (2018) 7892–7900. doi:doi.org/10.1021/acs.est.8b01883.

[70] P. Ahmedzade, B. Sengoz, Evaluation of steel slag coarse aggregate in hot mix asphalt concrete, Journal of Hazardous Materials. 165 (2009) 300–305. doi:10.1016/j.jhazmat.2008.09.105.

[71] S. Eloneva, S. Teir, J. Salminen, C. Fogelholm, R. Zevenhoven, Fixation of CO2 by carbonating calcium derived from blast furnace slag, Energy. 33 (2008) 1461–1467. doi:10.1016/j.energy.2008.05.003.

[72] E. Belhadj, C. Diliberto, A. Lecomte, Characterization and activation of Basic Oxygen Furnace slag, Cement and Concrete Composites. 34 (2012) 34–40. doi:10.1016/j.cemconcomp.2011.08.012.

[73] R. Ragipani, S. Bhattacharya, A.K. Suresh, A Review on steel slag valorisation via mineral carbonation, Reaction Chemistry & Engineering. 6 (2021) 1152–1178. doi:10.1039/d1re00035g.

[74] W.S. Association, 2021 World Steel in Figures, 2021.

[75] G. Liu, K. Schollbach, S. Van Der Laan, P. Tang, M.V.A. Florea, H.J.H. Brouwers, Recycling and utilization of high volume converter steel slag into CO2 activated mortars – The role of slag particle size, Resources, Conservation & Recycling. 160 (2020) 104883. doi:10.1016/j.resconrec.2020.104883.

[76] Electric arc furnace carbon steel slag (EAF), Mineral Products Association. (n.d.). https://mineralproducts.org/Mineral-Products/Slag/Electric-arc-furnace-

carbon-steel-slag.aspx.

[77] W.M. Mayes, P.L. Younger, J. Aumônier, Hydrogeochemistry of Alkaline Steel Slag Leachates in the UK, Water Air Soil Pollut. 195 (2008) 35–50. doi:10.1007/s11270-008-9725-9.

[78] C. Barca, C. Gérente, D. Meyer, F. Chazarenc, Y. Andrès, Phosphate removal from synthetic and real wastewater using steel slags produced in Europe, Water Research. 46 (2012) 2376–2384. doi:10.1016/j.watres.2012.02.012.

[79] A.L. Riley, W.M. Mayes, Long-term evolution of highly alkaline steel slag drainage waters, Environmental Monitoring and Assessment. 187 (2015) 463. doi:10.1007/s10661-015-4693-1.

[80] R.M. Santos, D. Ling, A. Sarvaramini, M. Guo, J. Elsen, F. Larachi, G. Beaudoin, B. Blanpain, T. Van Gerven, Stabilization of basic oxygen furnace slag by hot-stage carbonation treatment, Chemical Engineering Journal. 203 (2012) 239–250. doi:10.1016/j.cej.2012.06.155.

[81] K.S. Lackner, C.H. Wendt, D.P. Butt, E.L.J. Joyce, D.H. Sharp, Carbon dioxide disposal in carbonate minerals, Energy. 20 (1995) 1153–1170.

[82] M. Kakizawa, A. Yamasaki, Y. Yanagisawa, A new CO 2 disposal process via artificial weathering of calcium silicate accelerated by acetic acid, Energy. 26 (2001) 341–354.

[83] S. Teir, S. Eloneva, C. Fogelholm, R. Zevenhoven, Dissolution of steelmaking slags in acetic acid for precipitated calcium carbonate production, Energy. 32 (2007) 528–539. doi:10.1016/j.energy.2006.06.023.

[84] H. Zhao, Y. Park, D.H. Lee, A.A. Park, Tuning the dissolution kinetics of wollastonite via chelating agents for CO 2 sequestration with integrated synthesis of precipitated calcium carbonates, Physical Chemistry Chemical Physics. 15 (2013) 15185–15192. doi:10.1039/c3cp52459k.

[85] C. Fusco, M. Casiello, P. Pisani, A. Monopoli, F. Fanelli, W. Oberhauser, R. Attrotto, A. Nacci, L. D'Accolti, Steel slag as low - cost catalyst for artificial photosynthesis to convert - CO2 and water into hydrogen and methanol, Scientific Reports. 12 (2022) 11378. doi:10.1038/s41598-022-15554-3.

[86] S.J. Chung, J.H. Park, D. Li, J. Ida, I. Kumakiri, J.Y.S. Lin, Dual-Phase Metal - Carbonate Membrane for High-Temperature Carbon Dioxide Separation, Industrial & Engineering Chemistry Research. 44 (2005) 7999–8006. doi:10.1021/ie0503141.

[87] L. Yang, S. Ricote, S.B. Lundin, J.D. Way, Ceramic/Metal-Supported, Tubular, Molten Carbonate Membranes for High-Temperature CO2 Separations, Industrial & Engineering Chemistry Research. 59 (2020) 13706–13715. doi:10.1021/acs.iecr.0c01668.

[88] I.I. Betsi-Argyropoulou, A.M. Moschovi, E. Polyzou, I. Yakoumis, Towards Ammonia Free Retrofitting of Heavy- Duty Vehicles to meet Euro VI Standards, in: Vehicle and Automotive Engineering, 2021: p. 17. doi:10.1007/978-981-15-9529-5_18.

[89] S. Frangini, S. Scaccia, The Dissolution of Oxygen in La 2 O 3 -Added 52 / 48 mol % Li / Na Molten Carbonate Determined by Gas Solubility Measurements, Journal of The Electrochemical Society. 152 (2005) A2155–A2158. doi:10.1149/1.2042909.

[90] L. Zhang, J. Tong, Y. Gong, M. Han, S. Wang, K. Huang, Fast electrochemical CO2 transport through a dense metal-carbonate membrane : A new mechanistic insight, Journal of Membrane Science. 468 (2014) 373–379. doi:10.1016/j.memsci.2014.06.028.

[91] G.A. Mutch, L. Qu, G. Triantafyllou, W. Xing, M. Fontaine, I.S. Metcalfe, Supported molten-salt membranes for carbon dioxide permeation, Journal of Materials Chemistry A. 7 (2019) 12951–12973. doi:10.1039/c9ta01979k.

[92] S. Afzal, A. Khan, Recent Advances in Molten-Carbonate Membranes for Carbon Dioxide Separation : Focus on Material Selection , Geometry , and Surface Modification, The Scientific World Journal. 2021 (2021). doi:doi.org/10.1155/2021/1876875.

[93] J. Malzbender, Mechanical aspects of ceramic membrane materials, Ceramics International. 42 (2016) 7899–7911. doi:10.1016/j.ceramint.2016.02.136.

[94] D.M. Moore, R.C. Reynolds, X-Ray Diffraction And the Identification and Analysis of Clay Minerals, second edi, Oxford University Press, 1997.

[95] M. Uo, T. Wada, T. Sugiyama, Applications of X-ray fluorescence analysis (XRF) to dental and medical specimens, Japanese Dental Science Review. 51 (2014) 2–9. doi:10.1016/j.jdsr.2014.07.001.

[96] P.P. Ewald, A Review of my Papers on Crystal Optics 1912 to 1968, Acta Crystallographica. 35 (1979) 1–9.

[97] H.M. Rietveld, A profile refinement method for nuclear and magnetic structures, Journal of Applyied Crystallography. 2 (1969) 65–71. doi:10.1107/S0021889869006558.

[98] A.F. Gualtieri, V. Riva, A. Bresciani, S. Maretti, M. Tamburini, A. Viani, Accuracy in quantitative phase analysis of mixtures with large amorphous contents. the case of stoneware ceramics and bricks, Journal of Applied Crystallography. 47 (2014) 835–846. doi:10.1107/S160057671400627X.

[99] L. Lutterotti, P. Scardi, Simultaneous structure and size-strain refinement by the Rietveld method, Journal of Applied Crystallography. 23 (1990) 246–252. doi:10.1107/S0021889890002382.

[100] B. Lafuente, R.T. Downs, H. Yang, N. Stone, The powder of databases: The RRUFF project, in: Highlights in Mineralogical Crystallography, 2016: p. 201.

[101] M. Kannan, Scanning Electron Microscopy: Principle, Components and

Applications, in: Fundamentals and Applications of Nanotechnology, 2018: p. 224.

[102] W. Zhou, R.P. Apkarian, Z.L. Wang, D. Joy, Fundamentals of Scanning Electron Microscopy (SEM), in: Scanning Microscopy for Nanotechnology, 2007: p. 522.

[103] D.B. Williams, C.B. Carter, Transmission Electron Microscopy, New York and London, 1996.

[104] V. Cosslett, Introducing the electron microscopy, Nature. 198 (1963) 820–821. doi:https://doi.org/10.1038/198820a0.

[105] FEI Tecnai F-20 Operations manual, (n.d.). www.slideshare.net.

[106] J. Bernardi, Energy Dispersive X-Ray Spectroscopy, in: Imaging Modalities for Biological and Preclinical Research: A Compendium, Volume 1, IOP Publishing Ltd, 2021.

[107] K. Robards, P.R. Haddad, P.E. Jackson, Principles and Practice of Modern Chromatographic Methods, Elsevier Academic Press, 2004. doi:10.1016/B978-0-08-057178-2.50004-2.

[108] A.D. McNaught, A. Wilkinson, IUPAC Compendium of Chemical Terminology, 2nd ed., Blackbell Scientific Publications, Oxford, 1997.

[109] R.A. Sheille, Gas Chromatography, in: Encyclopedia of Forensic Sciences, 2013: pp. 579–585.

[110] Solar Simulator Manufacturer, (n.d.) 40.

[111] C. Frohlich, J. London, Revised Instruction Manual On Radiation Instruments and Measurements, 1986.

[112] R. Cozzi, P. Protti, T. Ruaro, Analisi Chimica strumentale, 1997.

[113] C.A. De Caro, H. Claudia, UV / VIS Spectrophotometry - Fundamentals and Applications, (2017) 53.

[114] Shimadzu Corporation, Reflectance Measurements, (n.d.). https://www.shimadzu.com/an/service-support/technical-support/analysis-basics/fundamentals-uv/reflectance_measurements.html.

[115] B. Stuart, Infrared Spectroscopy: fundamentals and applications, Wiley, 2004. doi:10.1002/0470011149.

[116] S. Brunauer, P.H. Emmet, E. Teller, Adsorption of Gases in Multimolecular Layers, Journal of American Chemical Society. 60 (1938) 309–319. doi:10.1021/ja01269a023.

[117] P.A. Webb, Introduction to Chemical Adsorption Analytical Techniques and their Applications to Catalysis, 2003.

[118] L. Yin, Dynamic Light Scattering, 2012. doi:10.1002/9781118229347.ch8.

[119] R. Sandhu, N. Singh, J. Dhankhar, G. Kama, R. Sharma, Dynamic light scattering (DLS) technique, principle, theoretical considerations and applications, Nanotechnological and Biochemical Techniques for Assessing the Quality and Safety of Milk and Milk Products. (2018) 135–137. https://www.researchgate.net/publication/331022012_Dynamic_light_scattering_DLS_technique_principle_theoretical_considerations_and_applications.

[120] J.W.B.R. Strutt, On the Scattering of Light by Small Particles, The London, Edinburgh, and Dublin Philosophical Magazine and Journal of Science. 41 (1871) 447–454. doi:doi.org/10.1080/14786447108640507.

[121] E. Turianicová, P. Balá, Ľ. Tucek, A. Zorkovská, V. Zelenak, Z. Németh, A. Satka, J. Kovac, A possible way to storage carbon dioxide on mechanically activated olivine (Mg , Fe) 2SiO4 International Journal of Mineral Processing A comparison of the reactivity of activated and non-activated olivine, International Journal of Mineral Processing. 123 (2013) 73–77. doi:10.1016/j.minpro.2013.05.006.

[122] I. Rigopoulos, M.A. Vasiliades, K.C. Petallidou, I. Ioannou, A.M. Efstathiou, T.

Kyratsi, A method to enhance the CO 2 storage capacity of pyroxenitic rocks, Greenhouse Gases Science and Technology. 5 (2015) 577–591. doi:10.1002/ghg.

[123] S.S. Abdullahi, S. Güner, Y. Koseoglu, I.M. Musa, B.I. Adamu, M.I. Abdulhamid, Simple method for the determination of band gap of a nanopowdered sample using Kubelka Munk theory, Journal of the Nigerian Association of Mathematical Physics. 35 (2016) 241–246.

[124] G.J. Ross, Experimental alteration of chlorites into vermiculites by chemical oxidation, Nature. 255 (1975) 133–134. doi:doi:10.1038/255133a0.

[125] M.D. Ruiz Cruz, J.M. Nieto, Chhemical and structural evolution of “metamorphic vermiculite” in metaclastic rocks of the betic cordillera, Malaga, Spain: A synthesis, The Canadian Mineralogist. 44 (2006) 249–265. doi:10.2113/gscanmin.44.1.249.

[126] S.A. Hassanzadeh-Tabrizi, A. Bigham, M. Rafienia, Surfactant-assisted sol–gel synthesis of forsterite nanoparticles as a novel drug delivery system, Materials Science & Engineering C. 58 (2016) 737–741. doi:10.1016/j.msec.2015.09.020.

[127] A. Entezari Zarandi, F. Larachi, G. Beaudoin, P. Benoit, M. Sciortino, Nesquehonite as a Carbon Sink in Ambient Mineral Carbonation of Ultramafic Mining Wastes, Chemical Engineering Journal. 314 (2017) 160–168. doi:10.1016/j.cej.2017.01.003.

[128] K. Royce, C. Baars, Caring for geological collections : unresolved questions, Journal of Natural Science Collections. 8 (2021) 28–38.

[129] M. Stillings, Z.K. Shipton, R.J. Lunn, Mechanochemical processing of silicate rocks to trap CO2, Nature Sustainability. (2023). doi:https://doi.org/10.1038/s41893-023-01083-y.

[130] G. Wang, S. Xu, L. Jiang, C. Wang, Nickel supported on iron-bearing olivine for CO2 methanation, Hydrogen Energy. 41 (2016) 12910–12919. doi:10.1016/j.ijhydene.2016.06.066.

[131] C. Karthikeyan, P. Arunachalam, K. Ramachandran, A.M. Al-mayouf, S. Karuppuchamy, Recent advances in semiconductor metal oxides with enhanced methods for solar photocatalytic applications, Journal of Alloys and Compounds. 828 (2020) 154281. doi:10.1016/j.jallcom.2020.154281.

[132] D. Kralj, J. Kontrec, L. Brecevic, G. Fallini, V. Noethig-laslo, Effect of Inorganic Anions on the Morphology and Structure of Magnesium Calcite, Chemistry - A European Journal. 10 (2004) 1647–1656. doi:10.1002/chem.200305313.

[133] M.R. Cerón, L.S. Lai, A. Amiri, M. Monte, S. Katta, J. Kelly, M.A. Worsley, M.D. Merrill, S. Kim, P.G. Campbell, Surpassing the Conventional Limitations of CO 2 Separation Membranes with Hydroxide/Ceramic Dual-Phase Membranes, Journal of Membrane Science. 567 (2018) 191–198. doi:doi.org/10.1016/j.memsci.2018.09.028.

[134] J.R. Davis, Metals Handbook Desk Edition, 2nd ed., ASM International, 1998.

[135] S. Kandhasamy, A. Solheim, S. Kjelstrup, G.M. Haarberg, Electrolyte Melt Compositions for Low Temperature Molten Carbonate Thermocells, ACS Applied Energy Materials. 10 (2018) 5386–5393. doi:10.1021/acsaem.8b00984.

ACKNOWLEDGMENTS

I would like to thank my supervisor Prof. Gabriele Mulas for his guide, mentoring and help throughout this project. Special thanks to Prof. Stefano Enzo, Prof. Sebastiano Garroni, Dr. Fabrizio Murgia and the whole INMATE^2 LAB research group for their advice and support.

Maria Domenica Simula and Gabriele Masia are gratefully acknowledged for their contribution to the PhD project.

I would like to thank Dr. Mauro Mureddu and the whole research team of Sotacarbo Scpa for welcoming me in their research facilities in Carbonia (Italy), and for the support and advice that have broadened my knowledge.

I would like to thank Dr. Iakovos Yakoumis for hosting me in the laboratories of Monolithos Catalysts and Recycling Ltd., Athens (Greece). Many thanks to Dr. Eirini Zagoraiou for her guide in the world of dual-phase membranes.

I would like to thank Prof. Francisco Gracia for welcoming me in his research group at the Universidad de Chile, Santiago (Chile). Many thanks to him and his whole team for their help and the opportunities given me to achieve a better professional knowledge.